

SYNTHESIS AND MAGNETOTRANSPORT STUDY OF KAGOME LATTICE
MAGNETS

by

David Connor Jones
A Thesis
Submitted to the
Graduate Faculty
of
George Mason University
in Partial Fulfillment of
The Requirements for the Degree
of
Master of Science
Applied and Engineering Physics

Committee:

_____ Dr. Nirmal J. Ghimire, Thesis Chair
_____ Dr. Fereshte Ghahari Kermani,
Committee Member
_____ Dr. Patrick Vora, Committee Member
_____ Dr. Paul So, Department Chairperson
_____ Dr. Donna M. Fox, Associate Dean,
Office of Student Affairs & Special
Programs, College of Science
_____ Dr. Fernando R. Miralles-Wilhelm,
Dean, College of Science

Date: _____ Summer Semester 2021
George Mason University
Fairfax, VA

Synthesis And Magnetotransport Study of Kagome Lattice Magnets

A Thesis submitted in partial fulfillment of the requirements for the degree of Master of Science at George Mason University

by

David Connor Jones
Bachelor of Science
Virginia Tech, 2018

Director: Nirmal J. Ghimire, Assistant Professor
Department of Physics and Astronomy

Summer Semester 2021
George Mason University
Fairfax, VA

Copyright 2021 David Connor Jones
All Rights Reserved

Acknowledgements

First and foremost, I would like to thank my primary research and thesis advisor Dr. Nirmal J. Ghimire. Not only has he provided me a new understanding of physics, he has mentored me as experimental scientist, collaborator, and speaker, which I can carry with me into my future academic and research career. I also would like to particularly thank Dr. Igor I. Mazin for providing an extraordinary wealth of theoretical understanding. Other people I would like to thank include, Dr. Peter Siegfried, Hari Bhandari, and Dina Michel for all the guidance in the lab, Dr. Madhav Prasad Ghimire and Dr. Suvadip Das for providing theoretical analysis, and my thesis committee members Dr. Patrick Vora and Dr. Fereshte Ghahari Kermani for providing feedback on my project.

Table of Contents

	Page
List of Tables	vi
List of Figures	vii
Abstract	xx
1 Introduction.....	1
1.1 Kagome Quantum Materials.....	2
1.2 Magnetotransport Study on Fe_3Sn_2	8
1.3 RMn_6Sn_6 Compounds.....	12
1.3.1.1 YMn_6Sn_6	18
1.3.1.2 TbMn_6Sn_6	19
2 Crystal Growth and Characterization of YMn_6Sn_6 and TbMn_6Sn_6	23
2.1 Crystal Growth	23
2.2 DC Magnetic Susceptibility Measurements	26
2.3 Electrical Transport Measurements	30
3 Magnetic Properties of YMn_6Sn_6 and TbMn_6Sn_6	35
3.1 Magnetization Measurements.....	35
3.2 Magnetic Phase Diagrams	36
3.3 Magnetic Anisotropy: First-Principle Calculations.....	40
4 Magnetotransport Properties of YMn_6Sn_6 and TbMn_6Sn_6	49
4.1 Magnetoresistance Measurements.....	50
4.2 Hall Measurements.....	52
5 Summary and Outlook.....	58
A Kagome Lattice Electronic Properties	61
A.1 Tight-Binding Model.....	61
A.2 Monolayer Kagome Lattice	62
A.3 Bilayer Kagome Lattice.....	65
A.4 Topological Chern Gap State	67

A.5 Intrinsic Anomalous Hall Effects	71
Bibliography	79

List of Tables

Table	Page
1.1: Properties of the RMn_6Sn_6 (R = rare-earth) compounds where R^{3+} is rare-earth ion, a, b, c are the lattice parameters for a hexagonal crystal system, V is the volume of the hexagonal unit cell, and T_N is the Neel temperature [13, 14, 15, 17]. The compounds with non-magnetic and magnetic R^{3+} shown are highlighted in black and blue, respectively.	14

List of Figures

Figure	Page
<p>1.1: <i>Kagome lattice in the real world.</i> (a) Traditional Japanese kagome basket [5]. Kagome patterns on the (b) Dome of the Rock in Jerusalem [6] and (c) in the Parisian Courtyard in Budapest [7].....</p>	3
<p>1.2: <i>Magnetic and electronic properties of the kagome lattice.</i> (a) Illustration of an in-plane antiferromagnetic (AFM) non-collinear arrangement and the (b) calculated electronic band structure calculations using a simple tight-binding model with nearest-neighbor (NN) hopping for the kagome lattice. The electronic band structure (left) contains two Dirac bands (top and bottom) touching at the Dirac points (DP) at $E_D = 0$, with an additional third band which is non-dispersive, commonly referred to as the Flat band (FB). The two types of DPs, DP1 and DP2, are shown by the red and yellow circles, which exist at the K and K' points, respectively. The energy density plot (right) for the top Dirac band illustrates the hexagon shape of the first Brillouin zone with the black dots denoting the K and K' points. Materials with kagome lattices comprised of magnetic and metallic atoms can thus provide a platform to study the interplay of magnetism and electronic topology.</p>	5
<p>1.3: <i>Topologically protected Dirac bands of the kagome lattice.</i> Electronic band structure near the Dirac point (DP) (at $E_D = 0$) for a (a) massless and (b) massive Dirac fermion arising from sizeable spin-orbit effects (Kane-Mele model) in the presence of an out-of-plane magnetic field (broken time-reversal symmetry) [see <i>Appendix A.4</i>:</p>	

Topological Chern Gap State]. This gap is topological protected as each Dirac band is associated with a topological invariant (Chern number) which changes when this gap is opened. 7

1.4: *Crystal structure of the Fe_3Sn_2* . (a) Unit cell of the space group $Rm3$ structure of Fe_3Sn_2 with the Fe and Sn atoms shown by the green and gray spheres, respectively. (b) Illustration of the various atomic layers with the order $[Fe_3Sn][Sn][Fe_3Sn]$ along the c -axis but successively translated along the ab -plane. Note: the number of atoms shown within each layer do not coincide with its formula to provide improved visualization of the layers. 9

1.5: *Magnetotransport measurements on Fe_3Sn_2 by Ye et. al. [8]*. (a) External field dependence of magnetization with $H \parallel c$. The inset shows the temperature dependence of saturation magnetization. (b) External field dependence of the Hall resistivity with $H \parallel c$ and $I \perp c$. The inset shows the temperature dependence of the normal Hall coefficient R_0 and the anomalous Hall coefficient R_S . (c) External field dependence of total anomalous Hall conductivity. The dashed line represents the linear line fit to the high-field data used to calculate the anomalous Hall conductivity.(d) The calculated anomalous Hall (left axis) and longitudinal (right axis) conductivities dependence on temperature where the intrinsic anomalous Hall conductivity with $H \parallel c$ is shown in green, the total anomalous Hall conductivity with $H \parallel c$ is shown in red, the anomalous Hall conductivity with $H \perp c$ is shown in black, and the longitudinal conductivity is shown in blue. The inset is the calculated anomalous Hall conductivity dependence on the squared of the longitudinal conductivity..... 11

1.6: *Crystal structure of the RMn_6Sn_6 ($R = \text{rare-earth}$) compounds.* (a) Unit cell of the $HfFe_6Ge_6$ hexagonal-type structure (space group $P6/mmm$) of RMn_6Sn_6 with the R, Mn, and Sn atoms shown by the blue, red, and gray spheres, respectively. (b) Illustration of the various atomic layers with the order $[Sn_2R][Mn_3Sn][Sn_3][Mn_3Sn]$ along the c-axis. Note: the number of atoms shown within each layer do not coincide with its formula to provide improved visualization of the layers..... 13

Figure 1.7: *Structural and Magnetic Properties of the RMn_6Sn_6 ($R = \text{rare-earth}$) compounds* [13, 14, 15, 17]. (a) Rare-earth ion radius R^{3+} dependence on the atomic number for the lanthanides ($R = Lu, Gd-Tm$) with the non-magnetic and magnetic R^{3+} shown in black and blue, respectively. (b) Hexagonal lattice parameter c dependence on the rare-earth ion radius R^{3+} for the lanthanides ($R = Lu, Gd-Tm$). (c) Neel temperature T_N dependence on the number of unpaired electrons per R^{3+} . (d) T_N dependence on the hexagonal lattice parameter c 15

Figure 1.8: *Magnetic structures of the RMn_6Sn_6 compounds.* (a) The three exchange constants necessary to describe the magnetic behavior of the RMn_6Sn_6 compound for two cases: (left) rare-earth ion R^{3+} is non-magnetic (diamagnetic) and (right) magnetic (4f-moment). The R, Mn, and Sn atoms are shown by the blue, red, and gray spheres, respectively. J_1 (J_2) is the exchange constant between the Mn kagome sublattices separated by a Sn_3 (Sn_2R) layer, J_3 is the exchange constant between the second-nearest neighboring Mn kagome sublattices, and J_{Mn-R} is the exchange constant between the adjacent Mn (red) kagome and R (blue) triangular sublattices. (b) Illustration of the magnetic ground states on the Mn and R layers where the arrows represent existence

and orientation of the magnetic moments on Mn and R. Note: the angles between moments are idealized to zero degrees along the c-axis to provide improved visualization of the ground state. R^{3+} is non-magnetic for $R = Y, Lu,$ and Sc yielding an antiferromagnetic (AFM) arrangement. R^{3+} is magnetic for $R = Tm, Er, Gd, Dy, Ho,$ and Tb yielding an ferrimagnetic (FiM) arrangement. The asterisk (*) denotes that these magnetic moments on these R atoms emerge only in the presence of an external magnetic field in ground state..... 17

1.9: Illustration of the ground state incommensurate magnetic structure for YMn_6Sn_6 in zero-field. The nine rotating arrows correspond to the arrangement of the magnetic moments on the Mn atoms of the kagome lattice stacked along the c-axis. The circles correspond to the plane of the kagome lattices. The Y, Mn, and Sn atoms are shown by the blue, red, and gray spheres, respectively. The spiral of the incommensurate structure repeats after four two-kagome sublattices or eight layers as shown by the numbers on the left. α between 1-2, 3-4, 5-6,7-8 represents the angle between the neighboring FM-coupled Mn moments within the two-kagome sublattice separated by a Sn_3 layer. β between 2-3, 4-5, 6-7,8-1 represents the angle between the neighboring AFM-coupled Mn moments between the two-kagome sublattice separated by a Sn_2Tb layer ($\beta + \alpha \approx 90^\circ$)..... 19

1.10: Anomalous Hall resistivity ρ_{yx}^{AH} dependence on the longitudinal resistivity squared ρ_{xx}^2 from 2 to 300 K in $TbMn_6Sn_6$ as measured by Yin et al. [1]. The anomalous Hall conductivity $\sigma_{xy,int}$ is approximated [$\rho_{yx}^{AH} \approx \sigma_{xy,int} \rho_{xx}^2$] by the slope of

the curve. The illustration shows the Fermi energy E_F assumed to be within lower of the two massive Dirac band, thereby producing a non-zero $\sigma_{xy,int}$ 21

2.1: *Crystal growth and x-ray characterization for single crystals of YMn_6Sn_6 and $TbMn_6Sn_6$.* (a) Single element metallic compounds sealed in fused silica ampoule under vacuum (right) to be placed into the aluminum oxide crucible (left) for flux-growth. (b) KSL-1200X box furnace for flux-growth capable of reaching temperatures up to 1200 °C. (c) Centrifuge to decant excess Sn-flux. (d) Grown single crystals of YMn_6Sn_6 (left) and $TbMn_6Sn_6$ (right). The top groups show the collection of aggregate crystals pulled directly out from the fused silica ampoule. The bottom groups show the individual plate-like single crystals with polished surfaces. (e) Rigaku MiniFlex benchtop powder X-ray diffractometer..... 25

2.2: *X-ray power diffraction measurements for ground crystals of (a) YMn_6Sn_6 and (b) $TbMn_6Sn_6$.* Top: Rietveld refinement powder patterns measured at room temperature. The blue asterisk (*) indicates the impurity peak from the Sn-flux. Bottom: Selected data from the Rietveld refinement. Atomic coordinates are 0, 0, 0 for Y(Tb); 12, 0, z for Mn; 0, 0, z for Sn(1); 13, 23, 12 for Sn(2); and 13, 23, 0 for Sn(3)..... 26

2.3: *Illustration of the alignment for measuring direct current (DC) magnetic susceptibility $\chi = M/H$.* (a) Alignment for $H \perp c$ where the edge of the plate-like sample is parallel to $M \parallel H$ along z, which is perpendicular to the surface of the coilset puck. The small arrows with circular orbits represent magnetic moments for illustrational purposes. (b) Alignment for $H \parallel c$ where the surface of the plate-like sample is parallel to $M \parallel H$ along z..... 28

2.4: Quantum Design Dynacool Physical Property Measurement System (PPMS) with a 9 T magnet. The DC magnetization (DCM) linear motor is shown by the small cylinder placed on top of the PPMS. Below is the chamber where the sample is located at the end of a long rod where high magnetic fields (up to 9 T) and low temperatures (down to 1.8 K) can be achieved..... 29

2.5: DC magnetic susceptibility data for single crystals of YMn_6Sn_6 and $TbMn_6Sn_6$. (a) Temperature dependence DC magnetic susceptibility $\chi = M/H$ measured by zero-field-cooling (ZFC) with $H \parallel c$ at $\mu_0H = 0.1$ T for a single crystal of YMn_6Sn_6 . The peak at $T_N \approx 333$ K corresponds to the Neel temperature for YMn_6Sn_6 and the arrow at 333 K corresponds to an emerging incommensurate phase upon cooling. (b) Temperature dependence of χ measured by both ZFC and field-cooling (FC) with $H \perp c$ and $H \parallel c$ at $\mu_0H = 0.1$ T for a single crystal of $TbMn_6Sn_6$. The two cubic graphics illustrate the crystallographic orientations of the Tb and Mn magnetic moments below (along the c-axis) and above (perpendicular to the c-axis) the vicinity of the spin-reorientation transition temperature T_{sr} from left to right, respectively..... 30

2.6: Electrical transport data for single crystals of YMn_6Sn_6 and $TbMn_6Sn_6$. (a) Temperature dependence of electrical resistivity for YMn_6Sn_6 with $I \perp c$, yielding a residual resistivity ratio $RRR = \rho_{xx}(350 \text{ K})/\rho_{xx}(2 \text{ K}) \approx 46$. The inset shows the temperature dependence of the first derivative of the electrical resistivity with respect to temperature where the sudden drop represents the temperature below which the incommensurate phase emerges. (b) Temperature dependence of electrical resistivity for YMn_6Sn_6 with $I \perp c$, yielding a residual resistivity ratio $RRR = \rho_{xx}(350 \text{ K})/\rho_{xx}(2$

K) ≈ 78 . The inset shows the temperature dependence of the first derivative of the electrical resistivity with respect to temperature where the peak represents the spin reorientation process temperature T_{sr} at zero-field. 34

3.1: *Magnetization data for single crystals of YMn_6Sn_6 and $TbMn_6Sn_6$.* (a) External field dependence of magnetization for YMn_6Sn_6 with $H \perp c$ (blue) and $H \parallel c$ (red) at 5 K and 245 K*. (b) External field dependence of magnetization $TbMn_6Sn_6$ with $H \perp c$. (c) External field dependence of magnetization for $TbMn_6Sn_6$ with $H \parallel c$ using our 9 T Quantum Design PPMS. The inset shows the temperature dependence of saturation magnetization and coercive field. 36

3.2: *Magnetic phases in YMn_6Sn_6 with $H \perp c$.* (a) Magnetic phase diagram constructed from AC susceptibility measurements. The four magnetic phases are distorted spiral (DS) ($0 < H < H_1$), transverse conical spiral (TCS) ($H_1 < H < H_2$), fan-like (FL) ($H_2 < H < H_3$), and forced-ferromagnetic (FF) ($H_3 < H$). The narrow intermediate phases I and II exist between the FL and FF phases and between the TCS and FF phases. Phase I is now known to be a mixed phase of commensurate and incommensurate magnetic structure, the nature of which is yet to be determined. Phase II is known to be a canted antiferromagnet (CAF) state [35]. (b) Illustration of the four magnetic phases in YMn_6Sn_6 as determined by neutron scattering* and first principles calculations [15]. 38

3.3: *First Order Magnetization Process (FOMP) in $TbMn_6Sn_6$.* M dependence on H with (a) $H \perp c$ and (b) $H \parallel c$ for various temperatures within the vicinity of the spin-reorientation transition temperature T_{sr} . dM/dH dependence on H with (c) $H \perp c$ and (d) $H \parallel c$ for various temperatures within the vicinity of T_{sr} 39

3.4: Constructed magnetic phase diagram from magnetization measurements [Fig. 3.3] for TbMn ₆ Sn ₆ . H_{sr} is the field at spin-reorientation transition field and T_{sr} is the spin-reorientation transition temperature.....	40
3.5: Reduced energies E/J_1 for the magnetic phases with $H \perp c$ as a function of reduced magnetic field H/J_1 calculated using density functional theory (DFT) calculations using mean field theory calculations [20]. The planar phase, shown in blue, comprises of the distorted spiral (DS) phase ($0 < H < H_1$), fan-like (FL) phase ($H_2 < H < H_3$) and polarized forced-ferromagnetic (FF) phase ($H_3 < H$). The transverse conical spiral (TCS) ($H_1 < H < H_2$) is shown in green. The longitudinal conical spiral (LCS) phase, shown in red, exists only for $H \parallel c$ and is a spin-reorientation TCS phase along the c-axis.....	42
3.6: Magnetic field dependence of incommensurate magnetic Bragg peaks $(0, 0, 2 - k_{z,n})$ ($n = 1,2$) at 100 K obtained from single crystal neutron diffraction on YMn ₆ Sn ₆ *. The solid black lines in the right panel are the corresponding Gaussian fits.....	43
3.7: <i>Magnetic Anisotropy Analysis for TbMn₆Sn₆</i> . (a) Magnetic phase diagram for the spin-reorientation transition. Positive values for $\mu_0 H_{sr}$ correspond to $H \perp c$ whereas negative values correspond to $H \parallel c$. The fitted curve with $K_{Mn} = - 8.96 \times 10^{-2} \text{ meV} / \mu_B^2$ and $K_{Tb} = 0.136 \text{ meV} / \mu_B^2$ is overlayed on top of the experimental values. The dashed vertical line represents the zero-field spin reorientation transition temperature T_{sr} . (b) Temperature dependence of the magnetic moments on Mn and Tb [$M_{Mn}(0) \approx 2.29 \mu_B$ and $M_{Tb}(0) \approx 8.57 \mu_B$] and magnetic anisotropy energies for the Mn- and Tb-sublattices [$MAE_{Mn}(0) \approx - 0.47 \text{ meV}$ per Mn and $MAE_{Tb}(0) \approx 10.0 \text{ meV}$ per Tb].	48

3.8: Fit of Brillouin curves (solid lines) to experimental data (points) for the temperature dependence on the magnetic moments on Mn and Tb obtained from a previous neutron powder diffraction study by Malaman et al. [14].	48
4.1: <i>Magnetoresistance in YMn₆Sn₆ and TbMn₆Sn₆</i> . External field dependence of magnetoresistance MR for (a) YMn ₆ Sn ₆ and (b) TbMn ₆ Sn ₆ with $H \parallel c$ and $I \perp c$. The inset for (a) shows MR at 100 K displays a “butterfly” effect in TbMn ₆ Sn ₆ up to some field H_b where MR is positive when the field is increasing towards H_b and negative above.	51
4.2: <i>Hall resistivity in TbMn₆Sn₆</i> . (a) External field H dependence of the Hall resistivity ρ_{yx} with $H \parallel c$ and $I \perp c$. (b) External field dependence of ρ_{yx} overlaid with magnetization M with $H \parallel c$ and $I \perp c$ between for 2 and 100 K.....	56
4.3: <i>Anomalous Hall Analysis in TbMn₆Sn₆</i> . Square of longitudinal resistivity dependence of the anomalous Hall resistivity with $H \parallel c$ and $I \perp c$ for in (a) logarithm scale and (b) non-logarithm scale for low (< 100 K) and high (≥ 100 K) temperature regimes shown in blue and red, respectively. The dashed line in (b) shows a linear fit through zero intercept for the high temperature regime with a slope of $\approx 96.6 \Omega^{-1} \text{ cm}^{-1} = 0.06 e^2/h$ per kagome layer.....	57
A.1: Two-dimensional (2D) kagome lattice in black overlaid with the 2D honeycomb lattice in blue. The black dots denote the atomic sites of the kagome lattices.....	64
A.2: <i>Simple tight-binding model with nearest-neighbor hopping for a single layer of the honeycomb and kagome lattices with $t_1 = 1$ (arbitrary units)</i> . (a) Honeycomb lattice calculated band structure. The points at which the top and bottom bands touch at $E_D =$	

0 are the Dirac points (DP). (b) Kagome lattice calculated band structure (shifted to $E_D = 0$). The additional band at the bottom is the Flat band (FB). (c) Energy density plot for the top band in (b). The dashed line illustrates the hexagon shape of the first Brillouin zone, and the black dots denote the DPs which exist at the K and K' points. 65

A.3: 3D illustration of the bilayer kagome lattice where two 2D kagome lattices are stacked along the c-axis. The vertical dashed arrow shows hopping path between a vertically displaced site with orbital hopping strength t_2 66

A.4: *Simple tight-binding model with nearest-neighbor hopping (arbitrary units) for a bilayer kagome lattice with $t_2 = 1$ and $t_1 = 0.15$.* (a) Calculated band structure where orange and blue represent the lower and upper bands, respectively. (b) Energy filled up to the lower Dirac point at $E - E_{DC} = E_{D,1} = -t_2$. (c) Energy filled up to the midpoint between the lower and upper Dirac points at $E - E_{DC} = 0$ within the Dirac circle. (d) Energy filled up to the upper Dirac point at $E - E_{DC} = E_{D,1} = +t_2$ 67

A.5: *Conceptualization of the Kane-Mele spin-orbit coupling (SOC) model.* (a) In a classical picture, as an electron hops from site i to a next-nearest-neighbor (NNN) site j , it feels an effective electric field E_{ij} induced by the positive charge via columbic potential on the nearest-neighbor (NN) site. This produces an effective magnetic field B_z in the rest frame of the electron which couples with the spin vector of the electron S_z via SOC. (b) The SOC interaction can also be written in terms of the hopping unit vectors d_i and d_j 68

A.6: *Band structure for a Dirac fermion acquiring mass for monolayer and bilayer kagome lattices with $t_1 = 1$ (arbitrary units).* (a) Calculated band structure near the Dirac

point energy $E_D = 0$ for a massless Dirac fermion ($m^* = 0$) in a single layer kagome lattice. (b) Calculated band structure near $E_D = 0$ for a Dirac fermion with an acquired mass ($m^* \neq 0$) in a single layer kagome lattice. (c) Calculated band structure near the Dirac point energies $E_{D,1} = -t_2$ and $E_{D,2} = +t_2$ for a massless Dirac fermion ($m^* = 0$) in a bilayer kagome lattice where $t_2 = 0.15$ and orange and blue represent the lower and upper bands, respectively. (d) Calculated band structure near $E_{D,1} = -t_2$ and $E_{D,2} = +t_2$ for a Dirac fermion with an acquired mass ($m^* \neq 0$) in a bilayer kagome lattice..... 70

A.7: *Berry curvature conceptualization.* (a) A magnetic field in the z -direction B_z is generated within the loop enclosed by the charge of the electron traveling in the x - y plane. (b) A Berry curvature in the k_z -direction Ω_{kz} is generated within the loop enclosed by the electron traveling in the k_x - k_y plane with a non-zero Berry phase (adiabatic phase).

..... 73

A.8: *Non-zero Berry curvature conceptualization example.* (a) Because of the preserved inversion and time-reversal symmetries within the k_x - k_y plane for the spin-up (red) and spin-down (blue) electrons bands, the total summation of the Berry curvature Ω_{kz} from each band n is zero. (b) When an applied electric field is induced in the k_y -direction E_{ky} , inversion symmetry is broken within the k_x - k_y plane, generating greater values for $\Omega_{kz}(+k_y)$ than for $\Omega_{kz}(-k_y)$. The total summation of Ω_{kz} is still however zero as time-reversal symmetry is still preserved. (c) When both E_{ky} and a magnetic field in the k_z -direction B_{kz} are applied, the inversion and time-reversal symmetries within the k_x - k_y plane for the spin-up and spin-down electrons bands are broken. The total summation

of Ω_{kz} is now non-zero, effectively yielding a non-zero intrinsic anomalous Hall conductivity..... 74

A.9: Conceptual formulation of the intrinsic anomalous Hall conductivity for a single Dirac fermion in a single layer kagome lattice using a Bloch sphere representation with $t_l = 1$ (arbitrary units). (a) Left: Filled states up to the Fermi energy $E_F = 0.15$ for a massless Dirac fermion. Right: Corresponding Bloch-sphere representation illustrating that the wavefunction of the massless Dirac fermion is confined to the Bloch sphere’s equator, yielding a zero Berry phase. (b) Left: Filled states up to E_F for a massive Dirac fermion. Right: Corresponding Bloch-sphere representation illustrating that the wavefunction of the massive Dirac fermion is confined to the Bloch sphere’s topologically distinctive lower and upper hemispheres, yielding a non-zero Berry phase. (c) Intrinsic anomalous Hall conductivity dependence on E_F for a massive Dirac fermion with Kane-Mele SOC strength $\lambda = 0.05$ and 0.10 with out-of-plane magnetization ($\theta = 0$), using Eq. A.20. 76

A.10: Conceptual formulation of the intrinsic anomalous Hall conductivity for a single Dirac fermion in a bilayer kagome lattice using a Bloch sphere representation with $t_l = 1$ (arbitrary units). (a) Left: Filled states up to the Fermi energy $E_F = 0.25$ for a massless Dirac fermion. Right: Corresponding Bloch-sphere representation illustrating that the wavefunctions of the massless Dirac fermion are confined to the Bloch sphere’s equator, yielding a zero Berry phase. (b) Left: Filled states up to E_F for a massive Dirac fermion. Right: Corresponding Bloch-sphere representation illustrating that the wavefunctions of the massive Dirac fermion are confined to the Bloch sphere’s

topologically distinctive lower and upper hemispheres, yielding a non-zero Berry phase.

The total wavefunction is a superposition of the wavefunctions from each Dirac cone.

(c) Intrinsic anomalous Hall conductivity dependence on E_F for a massive Dirac fermion with Kane-Mele SOC strength $\lambda = 0.05$, out-of-plane magnetization ($\theta = 0$), and interplanar hopping strength $t_2 = 0, 0.1, \text{ and } 0.5$, using Eq. A.21..... 78

Abstract

SYNTHESIS AND MAGNETOTRANSPORT STUDY OF KAGOME LATTICE MAGNETS

David Connor Jones, M.S.

George Mason University, 2021

Thesis Director: Dr. Nirmal J. Ghimire

The investigation and manipulation of novel magnetic textures within topological quantum materials is emerging as a new frontier for future spin-based electronic devices. Recently, transition-metal based kagome magnets have shown to provide a natural platform to study the interplay between complex magnetism and electronic topology. Of particular interest is the family of RMn_6Sn_6 ($R = \text{rare-earth}$) compounds with kagome lattices, shown to host complex magnetic textures and topological states, both strongly dependent on the choice of R atom. This master's thesis is an experimental study on role of the rare-earth elements $R = \text{Y, Tb}$ on the magnetic and magnetotransport properties within single crystals of RMn_6Sn_6 compounds using magnetometry and magnetotransport measurements combined with first-principles calculations. The framework of this study largely focuses on the magnetic rare-earth compound TbMn_6Sn_6 and compares the magnetic and electronic properties to the non-magnetic rare-earth parent compound YMn_6Sn_6 .

We first present the methods and review the crystal growth and characterization of single crystals of YMn_6Sn_6 and TbMn_6Sn_6 . The Sn self-flux method was employed for crystal growth, yielding thick plate-like shaped single crystals of YMn_6Sn_6 and TbMn_6Sn_6 . Once trimmed to adequate dimensions, magnetic susceptibility and electrical transport measurements were performed. The DC magnetic susceptibility (χ) of YMn_6Sn_6 with the applied field $H \perp c$ and TbMn_6Sn_6 with $H \perp c$ and $H \parallel c$ reveal high ordering temperatures of $T_N \approx 345$ and 423 K, respectively, as well as distinct features consistent with transformations to their magnetic structure. For TbMn_6Sn_6 , a spin-reorientation transition is observed at $T_{sr} \approx 308$ K where the collinear moments on Tb and Mn reorient along the ab-plane to the c-axis upon decreasing temperature. The electrical resistivity (ρ_{xx}) of YMn_6Sn_6 and TbMn_6Sn_6 with the electrical current perpendicular to the c-axis ($I \perp c$) reveal high metallicity for the samples.

We next perform comprehensive magnetization measurements on the YMn_6Sn_6 and TbMn_6Sn_6 samples in combination with first-principal calculations to describe the microscopic nature of the role of the rare-earth element Tb within the collinear ferrimagnetic (FiM) structure in TbMn_6Sn_6 . By considering a simplified description of the collinear configuration on magnetic anisotropy energy (MAE), by lumping the Heisenberg exchange and single-site anisotropy terms, our analysis describes how the spin-reorientation magnetic phase diagram for TbMn_6Sn_6 is quantitatively described by the temperature dependencies of magnetic moments on the Mn- and Tb-sublattices. An enhanced magnetic state on Tb at low temperatures leads to a strong out-of-plane magnetization which likely enhances the stability of the intrinsic topological Chern gap

state previously observed by Yin et. al. [1] within TbMn_6Sn_6 in the presence of a modest out-of-plane applied magnetic field of $\mu_0 H \approx 2$ T at 4.2 K. Moreover, the significance of the antiferromagnetic (AFM) coupling between the Mn- and Tb-sublattices is revealed through a comparison between the estimated ground state magnetic anisotropy energies of the Mn-sublattices for the magnetic rare-earth TbMn_6Sn_6 compound [$MAE_{Mn}(0) \approx -0.47$ meV per Mn] and the non-magnetic rare-earth compound YMn_6Sn_6 [$MAE_{Mn}(0) \approx -0.12$ meV per Mn].

We then explore to what extent the magnetic state of Tb affects the electronic properties in TbMn_6Sn_6 , especially near the Fermi surface, and therefore the transport properties, such as the anomalous Hall effect (AHE), through magnetotransport measurements on YMn_6Sn_6 and TbMn_6Sn_6 with $I \perp c$ and $H \parallel c$. By comparing the measured magnetoresistance (MR) to that of YMn_6Sn_6 the role of the magnetic rare-earth Tb on the electronic properties is clearly significant low temperatures. The MR for TbMn_6Sn_6 transitions from negative to large and positive below around 100 K and is likely attributed to the enhanced magnetic state on Tb at low temperatures. The Hall resistivity (ρ_{yx}) with H dependence and its calculated anomalous Hall resistivity (ρ_{xy}^{AH}) with ρ_{xx}^2 dependence for TbMn_6Sn_6 provides evidence of a likely dominating extrinsic contribution below around 100 K and a leading intrinsic contribution above 100 K that is likely not generated by a field-induced topological Chern gap.

At the end, we summarize the key findings of this study and outline future work to expand the scope of this study. Ultimately, the goal following this project would be to construct a comprehensive understanding of the role of the rare-earth elements among the

nine available RMn_6Sn_6 compounds to simultaneously engineer desirable magnetic and topological states potentially valuable for future spin-based electronic devices.

Chapter 1: Introduction

This master's thesis presents a systematic experimental study on role of the rare-earth elements $R = Y, Tb$ on the magnetic and magnetotransport properties within the family of RMn_6Sn_6 compounds. All figures and tables were custom-made for this thesis unless otherwise stated. It comprises of five chapters. The first chapter contains a detailed introduction to the kagome quantum materials, including an overview of the family of RMn_6Sn_6 compounds, as well as previous experimental studies on Fe_3Sn_2 , YMn_6Sn_6 , and $TbMn_6Sn_6$. The second chapter details the crystal growth and characterization of single crystals of YMn_6Sn_6 and $TbMn_6Sn_6$. The third chapter describes the microscopic nature of the role of the rare-earth element Tb within the ferrimagnetic structure of $TbMn_6Sn_6$ and compares with the helimagnet YMn_6Sn_6 . The fourth chapter presents the magnetotransport measurements on YMn_6Sn_6 and $TbMn_6Sn_6$ to describe the role of the rare-earth element Tb on the electronic properties near the Fermi level within $TbMn_6Sn_6$. The concluding chapter five summarizes the key findings from this study and discusses future work to expand its scope.

1.1 Kagome Quantum Materials

Kagome is a traditional Japanese style of bamboo weaving consisting of the edges and vertices of the trihexagonal tiling [Fig 1.1(a)], although the geometric pattern is known to exist in many cultures [Fig. 1.1(b)]. The term was introduced in physics by Itiro Syozi in 1951 [2] when he realized that a two-dimensional (2D) lattice made of this pattern, a kagome lattice, possess the same coordination number (the number of bonds each point is connected to) as the square lattice and he wondered (1) if the simple ferromagnetic (FM) Ising model can be solved analytically for this lattice and (2) if the transition temperature, T_C , for the two cases would be similar (in the mean field approximation, it would be the same however). The answer was shown true on both counts although the kagome lattice was shown to contain increased fluctuations. Syozi later realized that the antiferromagnetic (AFM) kagome lattice, as shown in Fig. 1.2(a), is the most frustrated 2D magnetic system that one can construct. In fact, it he discovered that it never orders at any temperature, and it was later realized [3] that this is not just a disordered paramagnet, but a new state of matter, termed a “spin-liquid.” [4] For a long time, it was its’ potential for hosting a quantum spin liquid that drove interest in the exotic magnetism of the kagome lattice.

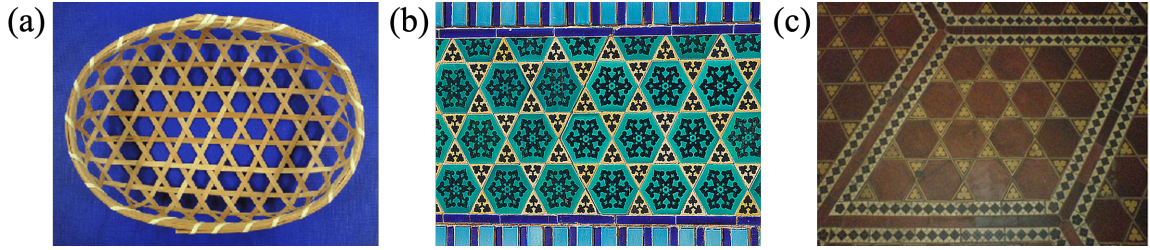


Figure A.1: *Kagome lattice in the real world.* (a) Traditional Japanese kagome basket [5]. Kagome patterns on the (b) Dome of the Rock in Jerusalem [6] and (c) in the Parisian Courtyard in Budapest [7].

It wasn't until the 21st century that it was finally observed [5] that the simple tight-binding electronic band structure of a single-orbital particle with nearest neighbor (NN) hopping contains several unusual features [see *Appendix A1: Tight-Binding Model* and *Appendix A2: Monolayer Kagome Lattice*] (the math is trivial, it is just nobody had been interested before), as shown in Fig. 1.2(b). One such feature is that the model reveals so-called Dirac bands, that is, massless quasiparticles called Dirac fermions whose energy depends strictly linearly on their momentum close to the Dirac points (DPs) [6]. The first Brillouin zone for the top Dirac band [Fig. 1.2(b)] illustrates the location of the DPs at the hexagon corners. Moreover, these Dirac bands are topologically protected, in the sense that the underlying model can be modified within some limits (e.g., longer-range, as well as interlayer-hopping effects [see *Appendix A3: Bilayer Kagome Lattice*], may be incorporated), and Dirac bands will remain such (their positions in the momentum-space are not protected, but their existence and their energies are [7]).

Another feature of the kagome band structure is the existence of the (non-dispersive) flat band (FB) [Fig. 1.2(b)]. This feature is not protected, so small modifications

of the underlying model can lead to a small, but finite dispersion of this band. However, it still retains its main property, a sharp peak in the density of electronic states at a particular energy. Consequently, electrons become localized within the hexagon of the kagome lattice with an infinite effective mass, leading to increased electronically correlated phenomenon. For example, when the FB is partially filled, fractional quantum Hall states can emerge as these localized electrons can mimic Landau levels, as in the case of twisted bilayer graphene [8].

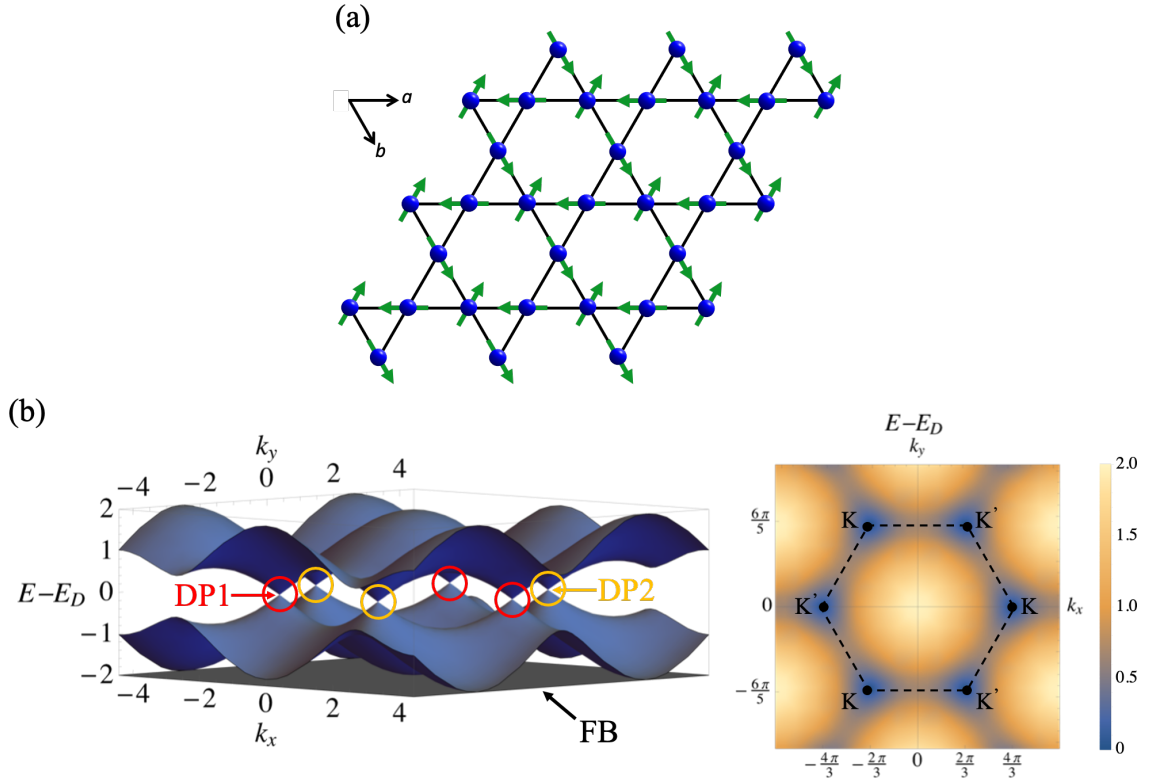


Figure A.2: *Magnetic and electronic properties of the kagome lattice.* (a) Illustration of an in-plane antiferromagnetic (AFM) non-collinear arrangement and the (b) calculated electronic band structure calculations using a simple tight-binding model with nearest-neighbor (NN) hopping for the kagome lattice. The electronic band structure (left) contains two Dirac bands (top and bottom) touching at the Dirac points (DP) at $E_D = 0$, with an additional third band which is non-dispersive, commonly referred to as the Flat band (FB). The two types of DPs, DP1 and DP2, are shown by the red and yellow circles, which exist at the K and K' points, respectively. The energy density plot (right) for the top Dirac band illustrates the hexagon shape of the first Brillouin zone with the black dots denoting the K and K' points. Materials with kagome lattices comprised of magnetic and metallic atoms can thus provide a platform to study the interplay of magnetism and electronic topology.

Dirac bands, in different contexts, have been observed in numerous 2D and 3D magnetic materials [9] [10] [11] [12]. To some extent, they enjoy considerable topological protection [see *Appendix A4: Topological Chern Gap State*] (although Dirac bands in magnetic materials are much rarer, and in many ways more interesting). Recently there has

been a considerable interest on the study of three-dimensional (3D) transition-metal kagome quantum magnets, comprising of stacked kagome lattices made of transitional-metal atoms, with Sn or Ge. This is because the transition-metal atoms provide the opportunity for the material to become both magnetic and metallic, i.e., a system to explore the interplay between magnetism and electronic topology. For example, a large anomalous Hall effect (AHE) and heavy Dirac bands were detected in the bilayer kagome ferromagnet Fe_3Sn_2 [8]. A coexistence of flat bands and Dirac cones (which are otherwise two extreme limits) were discovered in antiferromagnet FeSn [9]. Large AHE and magnetic Weyl fermions have been realized in the antiferromagnet Mn_3Sn [10], and a tunable spin-orbit coupled state was discovered in the FM Weyl semimetal $\text{Co}_3\text{Sn}_2\text{S}_2$ [11]. But the magnetism in these materials is quite simple (apart from the non-collinear AFM state in Mn_3Sn [Fig. 1.2(a)]), while compared to the highly frustrated purely 2D kagome magnetic system theoretically predicted by Syozi [2], stabilized by the interlayer coupling of the stacked kagome lattices combined with strong magnetic anisotropy [15].

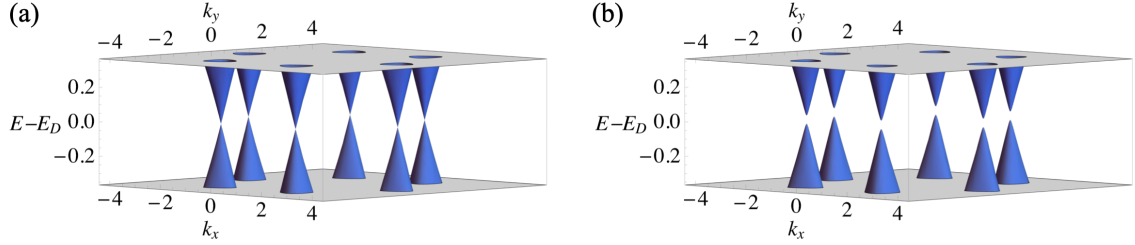


Figure A.3: *Topologically protected Dirac bands of the kagome lattice.* Electronic band structure near the Dirac point (DP) (at $E_D = 0$) for a (a) massless and (b) massive Dirac fermion arising from sizeable spin-orbit effects (Kane-Mele model) in the presence of an out-of-plane magnetic field (broken time-reversal symmetry) [see *Appendix A.4: Topological Chern Gap State*]. This gap is topological protected as each Dirac band is associated with a topological invariant (Chern number) which changes when this gap is opened.

RT₆X₆ compounds (R = rare-earth element, T = transition-metal element, and X = Sn or Ge) were extensively studied in the past for their structural, magnetic and transport properties, mostly in polycrystalline samples, but relatively untouched from topological point of view until recently. Now there are a few interesting reports of magnetic and electronic topological properties including recent work on the helimagnet YMn₆Sn₆ [15], where unconventional magnetic states and a new mechanism of "nematic spin chirality" responsible for the topological Hall effect have been realized. Another RT₆X₆ compound displaying interesting topological states is the ferrimagnet TbMn₆Sn₆, exhibiting an intrinsic topological Chern gap state with a modest out-of-plane magnetic field (~ 2 T) at 4.2 K in the quantum-limit using scanning tunneling microscopy (STM) [1]. Theoretically, this intrinsic topological Chern gap state can be attributed to a spin-polarized Kane-Mele spin-orbit effect present on the monolayer kagome lattices within TbMn₆Sn₆ [see *Appendix A.4: Topological Chern Gap State*]. What makes this material unique to the previously

mentioned transition-metal based kagome quantum magnets is that Tb can be replaced (or doped) with eight alternative rare-earth elements ($R = \text{Sc, Y, Gd-Tm, Lu}$), comprising of the family of RMn_6Sn_6 compounds, including YMn_6Sn_6 , to fine-tune the intrinsic topological state. This is significant because the various RMn_6Sn_6 compounds have been known to host complex spin textures, we will see in YMn_6Sn_6 , driven by temperature or an external magnetic field, including collinear, non-collinear, and incommensurate magnetic structures [13, 14, 15].

Alternative to STM, which directly measures the local density of states at the surface of a material, another experimental technique to probe the intrinsic electronic topological states within a material is magnetotransport. By measuring the components of a material's electrical conductivity tensor while perturbing its electronic states with an external magnetic field, magnetotransport provides information into Berry curvature effects connected to its intrinsic topological states [see *Appendix A.5: Intrinsic Anomalous Hall Effects*]. The next section details a recent magnetotransport study on the ferromagnet Fe_3Sn_2 [8], which predicts prominent Berry curvature effects arising from an intrinsic topological Chern gap state within Fe_3Sn_2 , akin to TbMn_6Sn_6 [1].

1.2 Magnetotransport Study on Fe_3Sn_2

The compound Fe_3Sn_2 forms into a hexagonal structure in the space group $R\bar{m}3$ with hexagonal lattice parameters $a = 5.338 \text{ \AA}$ and $c = 5.338 \text{ \AA}$ [8] as shown in Fig. 1.4(a). It is comprised of stacked bilayer kagome lattice made of Fe atoms, with Sn atoms filling the hexagons and stanene layers sandwiched between the bilayers [Fig. 1.4(b)]. Unlike the

monolayer kagome lattice [see *Appendix A.2: Monolayer Kagome Lattice*], the simple NN tight-binding with interlayer hopping electronic band structure for the bilayer kagome lattice contains two non-degenerate Dirac cones [see *Appendix A.3: Bilayer Kagome Lattice*], thereby naturally yielding separate contributions to $\sigma_{xy,int}^{AH}$ when incorporating spin-polarized Kane-Mele spin-orbit effects [see *Appendix A.5: Intrinsic Anomalous Hall Effects*]. Although the electronic properties of the RMn_6Sn_6 compounds can be predicted in the context of its highly monolayer kagome lattices, a recent magnetotransport study on Fe_3Sn_2 by Ye et. al. [8] serves as a complementary guide for analyzing measured magnetotransport data for TbMn_6Sn_6 , nevertheless.

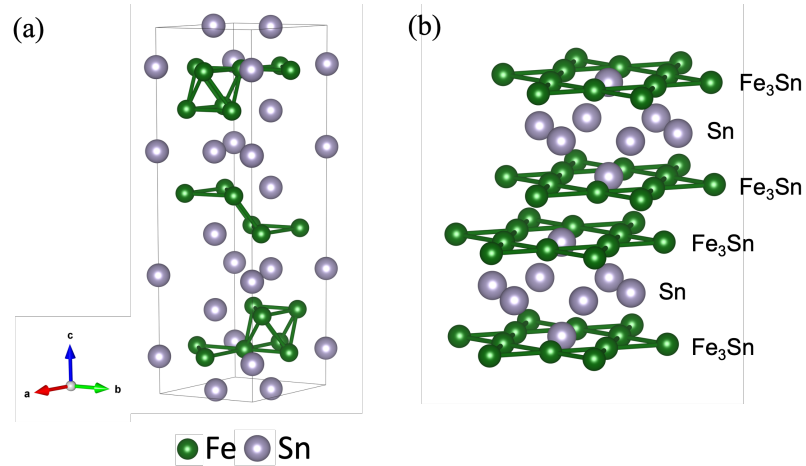


Figure A.4: *Crystal structure of the Fe_3Sn_2 .* (a) Unit cell of the space group $R\bar{3}m$ structure of Fe_3Sn_2 with the Fe and Sn atoms shown by the green and gray spheres, respectively. (b) Illustration of the various atomic layers with the order $[\text{Fe}_3\text{Sn}][\text{Sn}][\text{Fe}_3\text{Sn}]$ along the c-axis but successively translated along the ab-plane. Note: the number of atoms shown within each layer do not coincide with its formula to provide improved visualization of the layers.

Below $T_N = 670$ K, Fe_3Sn_2 naturally forms into a ferromagnet with its easy magnetization direction along the c -axis until around 300 K, where it gradually begins to cant towards the ab -plane upon cooling. This low temperature behavior leads to soft FM behavior when $H \parallel c$ as seen in the magnetization data from Ye et. al. [8] in Fig. 1.5(a). The Hall resistivity data [Fig. 1.5(b)] exhibits strong out-of-plane Hall response, as it strongly reflects the magnetization [Fig. 1.5(b)], a characteristic of the anomalous Hall effect (AHE) [see *Chapter 4.2: Hall Measurements*]. Fig. 1.5(c) shows the measured total Hall conductivity σ_{xy} as a function of H for various temperatures. By extracting the intercept at $H = 0$ using the high-field data, the temperature dependence of the anomalous Hall conductivity σ_{xy}^{AH} (in addition to the longitudinal conductivity σ_{xx}) is shown in Fig. 1.5(d). As σ_{xy}^{AH} likely contains both extrinsic and intrinsic contributions, σ_{xy}^{AH} can be parametrized with the form $\sigma_{xy}^{AH}(T) = f(\sigma_{xx,0})\sigma_{xx}^2(T) + \sigma_{xy,int}^{AH}(T)$ [20], where $\sigma_{xx,0} = \sigma_{xx}(T = 0)$, thereby approximating the temperature dependence of $\sigma_{xy,int}^{AH}$ by plotting σ_{xy}^{AH} as a function of σ_{xx}^2 [inset in Fig. 1.5(d)]. $\sigma_{xy,int}^{AH}$ remains relatively constant with temperature [Fig. 1.5(d)], varying within 10% from 400 to 2 K, at which $\sigma_{xy,int}^{AH} \approx 158 \text{ } \Omega^{-1}\text{cm}^{-1} = 0.27 \text{ } e^2/h$ per kagome bilayer. This nearly temperature independent contribution to the intrinsic AHE is indicative of massive Dirac bands in Fe_3Sn_2 with a substantial Berry-curvature contribution, since for a spin-polarized Kane-Mele spin-orbit effect, $\sigma_{xy,int}^{AH}$ theoretically depends only on the Fermi energy (which is generally nearly temperature independent) and the out-of-plane magnetization (shown nearly temperature independent in inset of Fig. 1.5(d)) [Eq. A.21]. The massive Dirac bands were

experimentally realized using angle resolved photoemission spectroscopy (ARPES) measurements [8], revealing the two non-degenerate Dirac cones as predicted in the NN tight-binding model [see *Appendix A.3: Bilayer Kagome Lattice*].

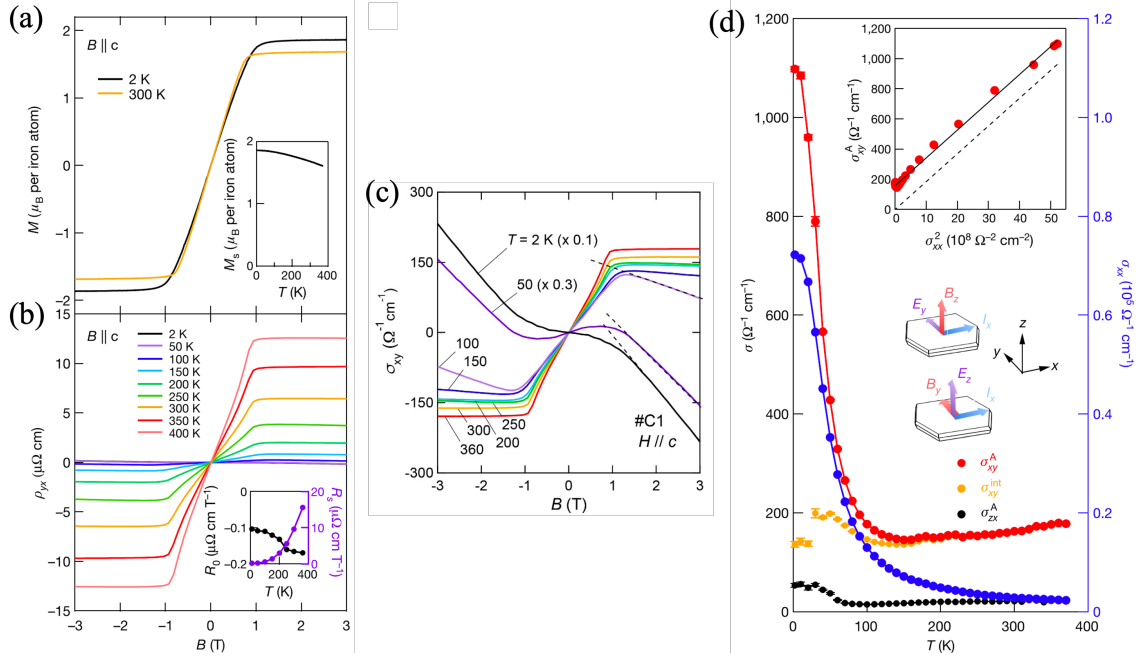


Figure A.5: Magnetotransport measurements on Fe_3Sn_2 by Ye et. al. [8]. (a) External field dependence of magnetization with $H \parallel c$. The inset shows the temperature dependence of saturation magnetization. (b) External field dependence of the Hall resistivity with $H \parallel c$ and $I \perp c$. The inset shows the temperature dependence of the normal Hall coefficient R_0 and the anomalous Hall coefficient R_S . (c) External field dependence of total anomalous Hall conductivity. The dashed line represents the linear line fit to the high-field data used to calculate the anomalous Hall conductivity. (d) The calculated anomalous Hall (left axis) and longitudinal (right axis) conductivities dependence on temperature where the intrinsic anomalous Hall conductivity with $H \parallel c$ is shown in green, the total anomalous Hall conductivity with $H \parallel c$ is shown in red, the anomalous Hall conductivity with $H \perp c$ is shown in black, and the longitudinal conductivity is shown in blue. The inset is the calculated anomalous Hall conductivity dependence on the squared of the longitudinal conductivity.

1.3 RMn₆Sn₆ Compounds

The RMn₆Sn₆ (R = rare-earth) compounds crystallize into a HfFe₆Ge₆ hexagonal-type structure (space group *P6/mmm*) [16], as shown in Fig. 1.6(a). These compounds comprise of stacked crystallographically equivalent Mn monolayer kagome lattices, each forming a net with Sn atoms (Mn₃Sn) [Fig. 1.6(b)], with the layers successively separated by either a three Sn blocks (Sn₃) or a mixed triangular R and honeycomb Sn layer (Sn₂R) - [Sn₂R][Mn₃Sn][Sn₃][Mn₃Sn]. The choice of the rare-earth element R leads to different properties of the material as presented in Table 1.1 and Fig. 1.7 [13, 14, 15, 17]. As a result of R³⁺ within ScMn₆Sn₆, LuMn₆Sn₆, and YMn₆Sn₆ containing zero unpaired electrons, the rare-earth sublattice is non-magnetic (diamagnetic) while the other RMn₆Sn₆ with R = Gd-Tm are magnetic (4f-moment). Such an environment opens an entirely new avenue to study the interplay of magnetism, and the properties inherent to kagome magnets - topology and correlations. For the lanthanides (R = Lu, Gd-Tm), the ionic radius of the R³⁺ decreases with increasing atomic number [Fig. 1.7(a)] because of Lanthanide contraction as the 4f-electrons provide poor shielding of the nuclear charge [18]. The decrease of the R³⁺ ion radius for the lanthanides leads a decrease in the hexagonal lattice parameter *c* [Fig 1.7(b)].

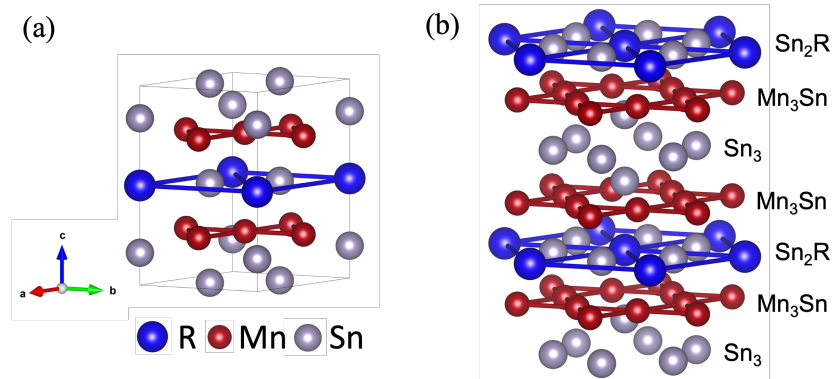


Figure A.6: *Crystal structure of the RMn_6Sn_6 ($R = \text{rare-earth}$) compounds.* (a) Unit cell of the $HfFe_6Ge_6$ hexagonal-type structure (space group $P6/mmm$) of RMn_6Sn_6 with the R, Mn, and Sn atoms shown by the blue, red, and gray spheres, respectively. (b) Illustration of the various atomic layers with the order $[Sn_2R][Mn_3Sn][Sn_3][Mn_3Sn]$ along the c-axis. Note: the number of atoms shown within each layer do not coincide with its formula to provide improved visualization of the layers.

Table A.1: Properties of the RMn_6Sn_6 (R = rare-earth) compounds where R^{3+} is rare-earth ion, a, b, c are the lattice parameters for a hexagonal crystal system, V is the volume of the hexagonal unit cell, and T_N is the Neel temperature [13, 14, 15, 17]. The compounds with non-magnetic and magnetic R^{3+} shown are highlighted in black and blue, respectively.

RMn_6Sn_6	ScMn_6Sn_6	LuMn_6Sn_6	YMn_6Sn_6	TmMn_6Sn_6	ErMn_6Sn_6	HoMn_6Sn_6	DyMn_6Sn_6	TbMn_6Sn_6	GdMn_6Sn_6
Atomic Number (# Protons)	21	71	39	69	68	67	66	65	64
R^{3+} Electron Configuration	[Ar]	[Xe] 4f ¹⁴	[Kr]	[Xe] 4f ¹²	[Xe] 4f ¹¹	[Xe] 4f ¹⁰	[Xe] 4f ⁹	[Xe] 4f ⁸	[Xe] 4f ⁷
# Unpaired Electrons on R^{3+}	0	0	0	2	3	4	5	6	7
R^{3+} Radius (\AA)	0.750	0.861	0.900	0.881	0.890	0.901	0.912	0.923	0.938
a, b (\AA)	5.469	5.508	5.541	5.514	5.516	5.520	5.522	5.531	5.536
c (\AA)	8.974	8.985	9.035	8.992	8.999	9.007	9.010	9.023	9.028
V (\AA^3)	232.5	236.1	238.8	236.8	237.1	237.7	237.9	238.9	239.6
T_N (K)	384	353	345	347	355	376	393	423	435

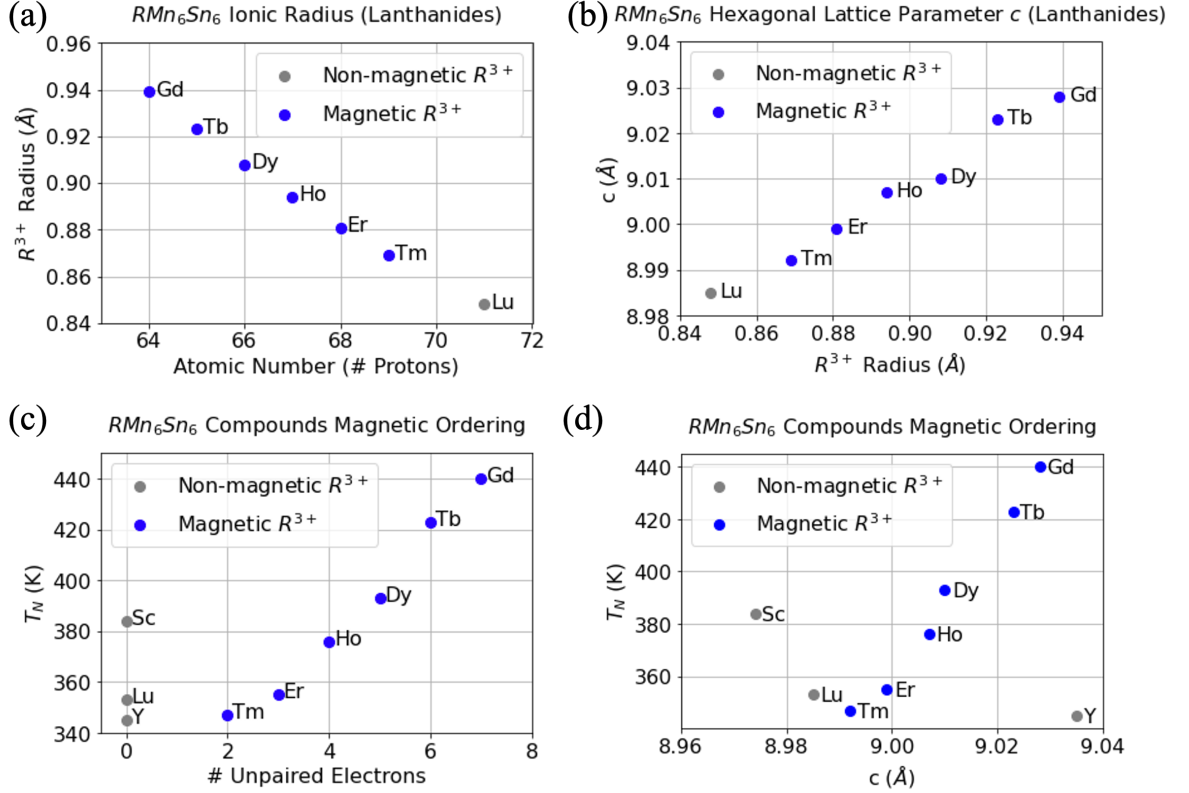


Figure A.7: *Structural and Magnetic Properties of the RMn_6Sn_6 ($R = \text{rare-earth}$) compounds [13, 14, 15, 17]. (a) Rare-earth ion radius R^{3+} dependence on the atomic number for the lanthanides ($R = \text{Lu, Gd-Tm}$) with the non-magnetic and magnetic R^{3+} shown in black and blue, respectively. (b) Hexagonal lattice parameter c dependence on the rare-earth ion radius R^{3+} for the lanthanides ($R = \text{Lu, Gd-Tm}$). (c) Neel temperature T_N dependence on the number of unpaired electrons per R^{3+} . (d) T_N dependence on the hexagonal lattice parameter c .*

By virtue of the Mermin-Wagner theorem, which states that for 2D systems at finite temperatures, continuous symmetries cannot be broken spontaneously with sufficient short-range interactions [19], the FM ordering in the Mn kagome lattice is strongly suppressed, causing the magnetic structure within the RMn_6Sn_6 to be governed by interplanar interactions between the Mn kagome and R triangular lattices. For the non-magnetic rare-earth compounds ($R = \text{Sc, Y, Lu}$), the magnetic structure can be adequately

described by the exchange interaction between the Mn kagome sublattices separated by a Sn_3 (Sn_2Tb) layer with exchange constant J_1 (J_2) and the exchange interaction between the second-nearest neighboring Mn kagome sublattices with exchange constant J_3 [20], as shown in Fig. 1.8(a), resulting in an AFM coupling between the Mn kagome sublattices as shown in Fig. 1.8(b). The Neel temperature T_N for the non-magnetic rare-earths increase with a decrease in c [Fig. 1.7(c)] [13, 14, 15, 17]. For the magnetic rare-earth compounds ($R = \text{Gd-Tm}$), the exchange interaction between the adjacent Mn kagome sublattice and R triangular sublattice with exchange constant J_{Mn-R} [Fig. 1.8(a)] are non-negligible, resulting in a ferrimagnetic (FiM) coupling between the Mn kagome sublattice and R triangular sublattice below T_N . The angle of the FiM arrangement with the c-axis in ground state depends on the rare-earth with $R = \text{Tb}$ being the only compound where the moments are aligned along the c-axis. An increase in the number of unpaired electrons on R^{3+} [Fig 1.7(c)] and c [Fig 1.7(d)] for the magnetic rare-earth compounds is correlated with an increase of T_N .

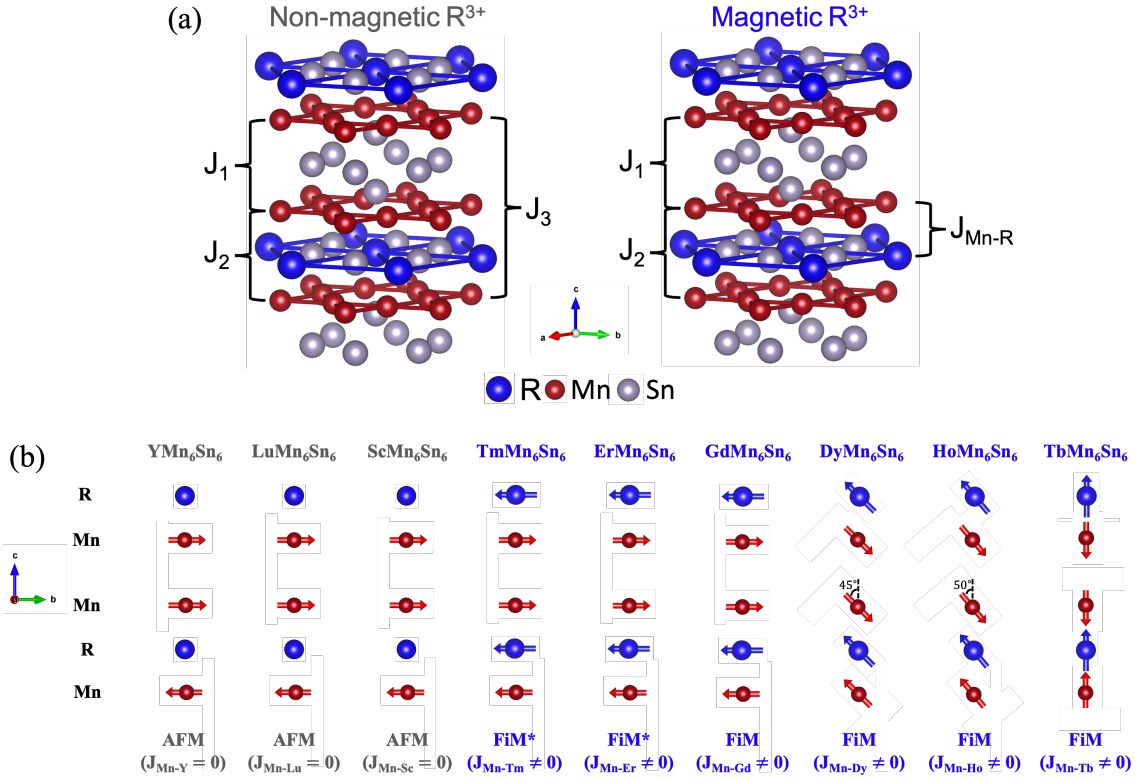


Figure A.8: *Magnetic structures of the RMn_6Sn_6 compounds.* (a) The three exchange constants necessary to describe the magnetic behavior of the RMn_6Sn_6 compound for two cases: (left) rare-earth ion R^{3+} is non-magnetic (diamagnetic) and (right) magnetic (4f-moment). The R, Mn, and Sn atoms are shown by the blue, red, and gray spheres, respectively. J_1 (J_2) is the exchange constant between the Mn kagome sublattices separated by a Sn_3 (Sn_2R) layer, J_3 is the exchange constant between the second-nearest neighboring Mn kagome sublattices, and $J_{\text{Mn-R}}$ is the exchange constant between the adjacent Mn (red) kagome and R (blue) triangular sublattices. (b) Illustration of the magnetic ground states on the Mn and R layers where the arrows represent existence and orientation of the magnetic moments on Mn and R. Note: the angles between moments are idealized to zero degrees along the c-axis to provide improved visualization of the ground state. R^{3+} is non-magnetic for $R = \text{Y}, \text{Lu},$ and Sc yielding an antiferromagnetic (AFM) arrangement. R^{3+} is magnetic for $R = \text{Tm}, \text{Er}, \text{Gd}, \text{Dy}, \text{Ho},$ and Tb yielding an ferrimagnetic (FiM) arrangement. The asterisk (*) denotes that these magnetic moments on these R atoms emerge only in the presence of an external magnetic field in ground state.

A.1.1.1 YMn_6Sn_6

YMn_6Sn_6 crystallizes with the hexagonal lattice parameters $a = 5.533 \text{ \AA}$ and $c = 9.008 \text{ \AA}$ [13]. The two exchange interactions across the Mn kagome sublattices separated by Sn_3 or Sn_2Y described by J_1 and J_2 are uniquely FM and AFM [Fig. 1.8(c)], respectively. Because Y^{3+} is effectively non-magnetic (diamagnetic) within YMn_6Sn_6 , J_{Mn-Y} is negligible, causing the nearest-neighbor exchange interactions (J_1 and J_2) to become parametrically frustrated by the exchange interaction across second-nearest neighboring Mn kagome sublattices described by J_3 [Fig. 1.8(a)]. This parametric frustration along the c-axis leads to non-trivial magnetic phases within YMn_6Sn_6 which compete with temperature and an applied magnetic field. Below $T_N \approx 345 \text{ K}$, YMn_6Sn_6 orders into a commensurate collinear AFM structure [15]. An incommensurate phase quickly emerges upon cooling at 333 K and coexists with the commensurate phase until 300 K, below which only the incommensurate phase exists down to zero temperature, as revealed by Venturini et. al. [16] via neutron diffraction. The magnetic structure of the incommensurate phase contains two nearly equal wave vectors where the sum of the angles α and β between FM-coupled spins across the Sn_3 and Sn_2Y layers [Fig. 1.6(b)], respectively, approximate to $\alpha + \beta \approx 90^\circ$, as illustrated in Fig. 1.9. At high temperatures, one of the competing magnetic phases, named the transverse conical spiral (TCS) phase, gives rise to the topological Hall effect by a new mechanism of nematic chirality [15], an example of magnetic topology. Magnetic properties have been reported in several materials in this class and have equally interesting features as in YMn_6Sn_6 , both in susceptibility and magnetization but are poorly studied.

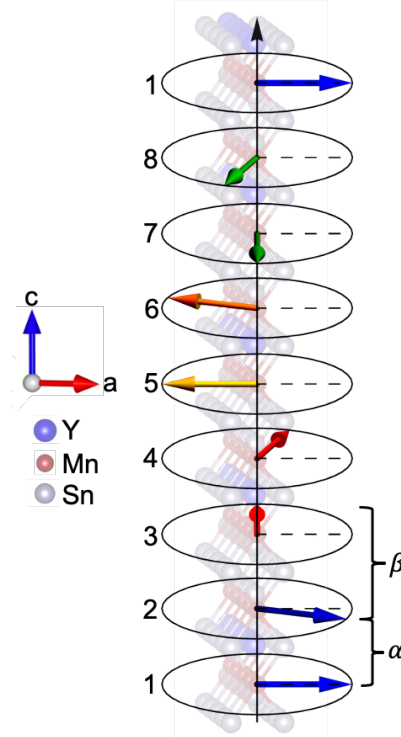


Figure A.9: Illustration of the ground state incommensurate magnetic structure for YMn_6Sn_6 in zero-field. The nine rotating arrows correspond to the arrangement of the magnetic moments on the Mn atoms of the kagome lattice stacked along the c -axis. The circles correspond to the plane of the kagome lattices. The Y, Mn, and Sn atoms are shown by the blue, red, and gray spheres, respectively. The spiral of the incommensurate structure repeats after four two-kagome sublattices or eight layers as shown by the numbers on the left. α between 1-2, 3-4, 5-6, 7-8 represents the angle between the neighboring FM-coupled Mn moments within the two-kagome sublattice separated by a Sn_3 layer. β between 2-3, 4-5, 6-7, 8-1 represents the angle between the neighboring AFM-coupled Mn moments between the two-kagome sublattice separated by a Sn_2Tb layer ($\beta + \alpha \approx 90^\circ$).

A.1.1.2 TbMn_6Sn_6

TbMn_6Sn_6 crystallizes with hexagonal lattice parameters $a = 5.530 \text{ \AA}$ and $c = 9.023 \text{ \AA}$ [21]. Unlike in the non-magnetic rare earth cousins, YMn_6Sn_6 , ScMn_6Sn_6 and LuMn_6Sn_6 , $J_{\text{Mn-Tb}}$ must be considered. Below $T_N \approx 421 \text{ K}$, the magnetic moments on Mn

and Tb form into a collinear (or at least close to) FiM arrangement down to 2 K as revealed by Idrissi et. al. [24] via neutron diffraction. At high temperatures, the magnetocrystalline anisotropy along the kagome planes dominates [22], resulting in the “easy-plane” type compound, similar to YMn_6Sn_6 in ground state [Fig. 1.9]. Below the spin-reorientation transition temperature at zero-field, $T_{sr} \approx 308$ K, the uniaxial anisotropy of the Tb-sublattice dominates and the easy magnetization direction is along the c-axis. When an external field is applied along the c-axis within TbMn_6Sn_6 at low temperatures, an emergence of a variety of pronounced states distributed in energy, a signature of Landau quantization, with a gap energy of 34 meV, was recently experimentally observed using low-energy scanning tunneling microscopy (STM) on the Mn kagome surface by Yin et al. [1] This observation, as well as the considerable gap size, is suggestive of the existence of magnetized Dirac electrons within the quantum limit in TbMn_6Sn_6 attributed to a spin-polarized Kane-Mele spin-orbit effect [see *Appendix A.4: Topological Chern Gap State*]. Moreover, the low-energy tunnelling spectrum at the step edge of the sample revealed that a prominent energy state emerges at 130 meV [1]. This effect was ascribed to the Fermi energy filled to the Chern gap, i.e., only the lower Dirac band is filled, yielding a topological protected edge state with corresponding bulk-boundary correspondence gap.

Magnetotransport measurements were also performed on a sample of TbMn_6Sn_6 by Yin et al. [1] to provide further evidence to the claim of the quantum-limit topological Chern gap state observed from STM. Fig. 1.10 shows the plotted anomalous Hall resistivity ρ_{xy}^{AH} as a function of the square of the longitudinal resistivity ρ_{xx}^2 from 2 to 300 with $I \perp c$ and $H \parallel c$ [1]. By fitting a linear line [Fig. 1.10], the intrinsic anomalous Hall conductivity

$\sigma_{xy,int}^{AH}$ was estimated using $\rho_{xy}^{AH} \approx \sigma_{xy,int}^{AH} \rho_{xx}^2$ in the limit of the small Hall angle $\theta_H = \rho_{yx}/\rho_{xx} \ll 1$ [see *Chapter 4.2: Hall Measurements*], which yields $\sigma_{xy,int}^{AH} \approx 0.14 e^2/h$ per kagome layer. This approximated value for $\sigma_{xy,int}^{AH}$ was assumed to arise from Berry curvature correspondence of the Chern gapped Dirac fermions [see *Appendix A.5: Intrinsic Anomalous Hall Effects*], as illustrated in the bottom right of Fig. 1.10.

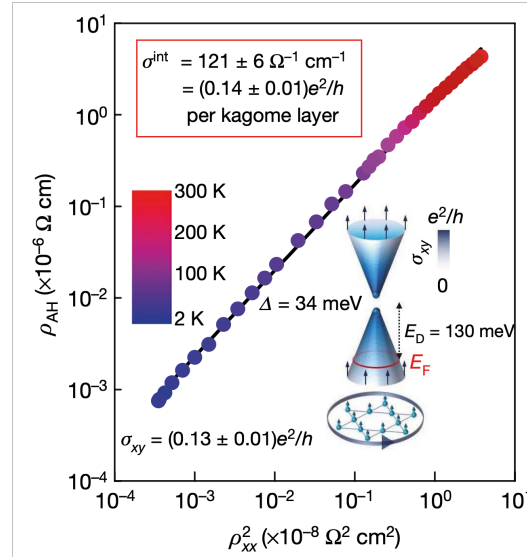


Figure A.10: Anomalous Hall resistivity ρ_{yx}^{AH} dependence on the longitudinal resistivity squared ρ_{xx}^2 from 2 to 300 K in TbMn_6Sn_6 as measured by Yin et al. [1]. The anomalous Hall conductivity $\sigma_{xy,int}$ is approximated [$\rho_{yx}^{AH} \approx \sigma_{xy,int} \rho_{xx}^2$] by the slope of the curve. The illustration shows the Fermi energy E_F assumed to be within lower of the two massive Dirac band, thereby producing a non-zero $\sigma_{xy,int}$.

As demonstrated by Yin et al. [1], the interesting physics in TbMn_6Sn_6 arises from its out-of-plane magnetic ordering. All other RMn_6Sn_6 compounds have easy-plane magnetic ordering [Fig. 1.8(b)] (excluding DyMn_6Sn_6 and HoMn_6Sn_6 , which are canted

ferromagnets). However, in magnetic field induced spin polarized states, all these RMn_6Sn_6 compounds are expected to have behavior like that of TbMn_6Sn_6 . In addition to the magnetic and magnetotransport properties within TbMn_6Sn_6 , which are poorly understood, the topological properties in other compounds are not studied at all.

Chapter 2: Crystal Growth and Characterization of YMn_6Sn_6 and TbMn_6Sn_6

1.4 Crystal Growth

Intermetallic compounds comprised of exclusively two or more different metal elements consist of atomic bonding with slightly more ionic and covalent character than compared to metallic compounds comprised of exclusively one metal element [23]. These differences in bond character among intermetallic compounds result in different behavior in materials. Therefore, to synthesize an intermetallic compound with starting materials of single element metallic compounds, one must heat the required metallic compounds to high temperatures to cause sufficient diffusion for a mixture to take place. In the flux method, another elemental metal (or a compound) is used as a solvent that can dissolve the desired reacting elements at temperatures much lower than their individual melting points. When one of the reacting metals does the job of the solvent, such a flux technique is called the “self flux” method. The flux method relies on the phase diagram to determine which path upon cooling to take to reach the desired intermetallic compound. Single crystals of YMn_6Sn_6 and TbMn_6Sn_6 are grown by the self-flux method using excess Sn as the flux. Y (Tb) pieces (Alfa Aesar, 99%), Mn pieces (Alfa Aesar, 99.95 %), and Sn shots (Alfa Aesar 99.999%) are added to a 2 mL aluminum oxide crucible in a molar ratio of 1:1:20 (1:6:20) and sealed in a fused silica ampoule under vacuum, as shown in Fig. 2.1(a). The sealed ampoule with Y (Tb) is heated in a box furnace [Fig. 2.1(b)] to 1175 °C (1150 °C) for 10

hours, homogenized at 1075 °C (1150 °C) for 12 hours, and then cooled to 600 °C (650 °C) at 4 °C / hour. Once the furnace reaches 600 °C (650 °C), the excess Sn-flux was decanted with a centrifuge [Fig. 2.1 (c)]. Single crystals of YMn₆Sn₆ and TbMn₆Sn₆ are shown in Fig. 2.1(d) and have thick plate-like shapes with distinct edges. The c-axis of YMn₆Sn₆ and TbMn₆Sn₆ naturally orients perpendicular to the plate-like surface [Fig. 2.1(d)]. The plate area of the grown YMn₆Sn₆ single crystals [left of Fig. 2.1(d)] are greater than for TbMn₆Sn₆ while the TbMn₆Sn₆ single crystals [right of Fig. 2.1(d)] are more brittle. The crystal structure was verified using powder x-ray diffraction at room temperature using a Rigaku MiniFlex benchtop diffractometer [Fig. 2.1(e)]. A small amount of the crystals from each batch were ground into powder and their collected diffraction patterns are shown in Fig. 2.2 using Rietveld refinement [32] with FullProf software [33]. Hexagonal lattice parameters $a = 5.5398(5)$ and $5.5388(1)$ Å, and $c = 9.0203(9)$ and $9.0329(2)$ Å, for YMn₆Sn₆ and TbMn₆Sn₆, respectively, are in good agreement with previous studies [Table 1.1] [13, 14, 15, 17]. The small peaks present in both YMn₆Sn₆ and TbMn₆Sn₆ patterns (as marked by the asterisks in Fig. 2.2(a) and (b), respectively) are identified to be Sn peaks attributed to excess Sn-flux on the surface of the single crystals and were omitted from the Rietveld refinement.

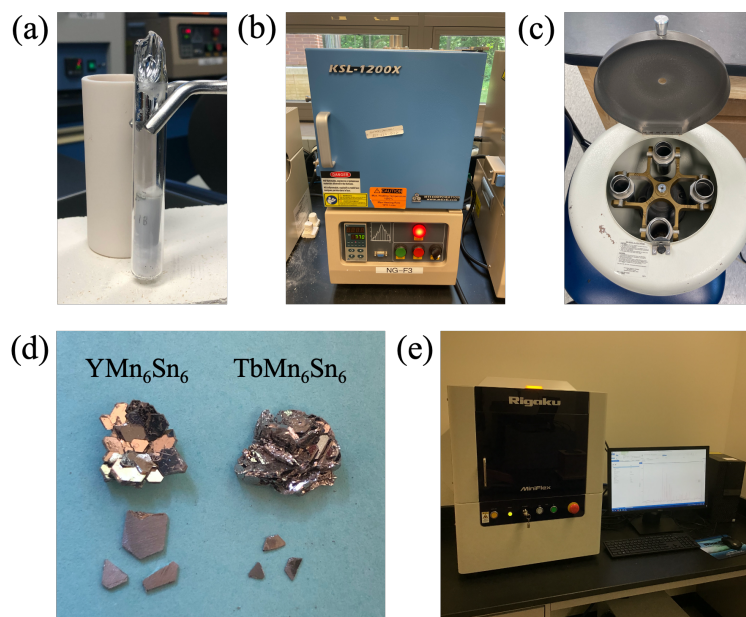


Figure B.1: *Crystal growth and x-ray characterization for single crystals of YMn_6Sn_6 and $TbMn_6Sn_6$.* (a) Single element metallic compounds sealed in fused silica ampoules under vacuum (right) to be placed into the aluminum oxide crucible (left) for flux-growth. (b) KSL-1200X box furnace for flux-growth capable of reaching temperatures up to 1200 °C. (c) Centrifuge to decant excess Sn-flux. (d) Grown single crystals of YMn_6Sn_6 (left) and $TbMn_6Sn_6$ (right). The top groups show the collection of aggregate crystals pulled directly out from the fused silica ampoule. The bottom groups show the individual plate-like single crystals with polished surfaces. (e) Rigaku MiniFlex benchtop powder X-ray diffractometer.

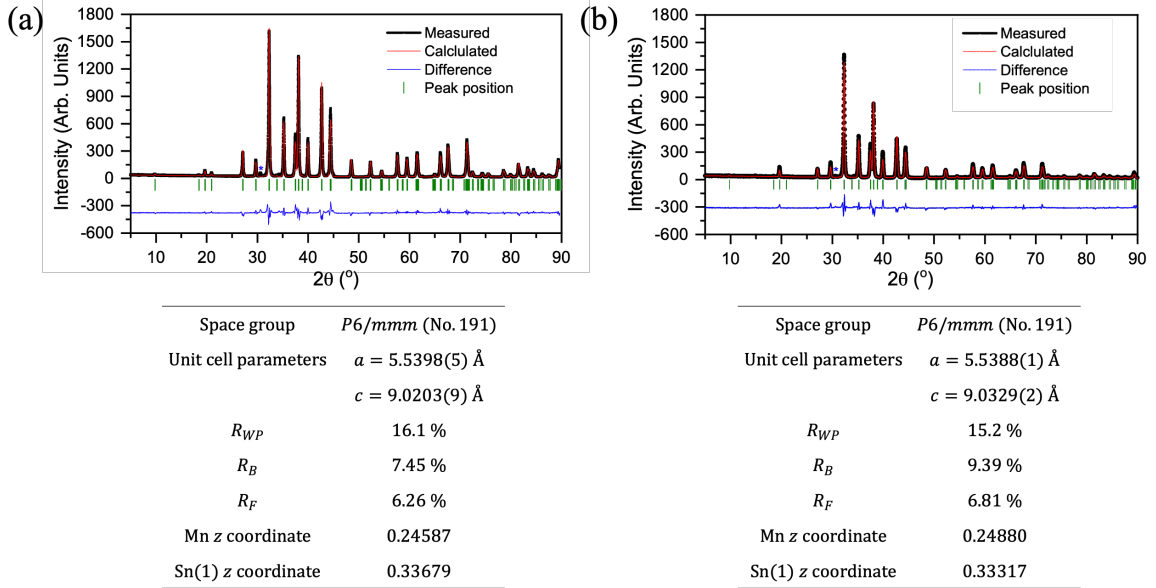


Figure B.2: *X-ray power diffraction measurements for ground crystals of (a) YMn_6Sn_6 and (b) $TbMn_6Sn_6$. Top: Rietveld refinement powder patterns measured at room temperature. The blue asterisk (*) indicates the impurity peak from the Sn-flux. Bottom: Selected data from the Rietveld refinement. Atomic coordinates are 0, 0, 0 for Y(Tb); 12, 0, z for Mn; 0, 0, z for Sn(1); 13, 23, 12 for Sn(2); and 13, 23, 0 for Sn(3).*

1.5 DC Magnetic Susceptibility Measurements

To characterize the bulk magnetic behavior of single crystals of YMn_6Sn_6 and $TbMn_6Sn_6$ with an external magnetic field H , direct current (DC) magnetic susceptibility $\chi = M/H$ measurements are performed with varying temperature, where M is the total DC magnetization of the sample. The importance of measuring χ during a continuous temperature sweep is that it provides a quantitative measure of the extent to which a material can be magnetized when placed in an applied magnetic field. The grown single crystal samples of YMn_6Sn_6 and $TbMn_6Sn_6$ are polished on all sides to remove any excess Sn-flux which may provide additional contributions to M . To orient H along the appropriate crystallographic direction within the sample, the plate-like surface of the

sample is oriented above the coilset puck differently for $H \perp c$ and $H \parallel c$, as illustrated in Fig. 2.3(a) and (b), respectively. For $H \perp c$ [Fig. 2.3(a)], the plate-like surface of the sample [Fig. 2.1(d)] is firmly positioned normal to H using a custom-made brass holder. For $H \parallel c$ [Fig. 2.3(b)], the plate-like surface is firmly positioned parallel to H by gluing to the sample holder surface with GE-varnish. The prepared sample holder and coilset puck are next slowly placed into the Quantum Design Dynacool Physical Property Measurement System (PPMS), shown in Fig. 2.4, where $M \parallel H$ is measured using the direct current magnetization (DCM) option incorporated within the alternating current measurement system (ACMS) II. The basic principle of operation of the DCM option is based on Faraday's law of induction where a change in magnetic field flux Φ from the sample induces a voltage V_{coil} on two counterwound coils situated just above and below the sample of the coilset puck given by

$$V_{coil} = \frac{d\Phi}{dt} = \frac{d\Phi}{dz} \frac{dz}{dt}, \quad (2.1)$$

where dz is change in position of the puck along the direction z normal to the surface of the coilset puck. The coilset puck is placed at the end of a rod connected to the DCM linear motor on top of the Quantum Design Dynacool PPMS [Fig. 2.4], which sinusoidally oscillates the coilset puck along z at very low frequencies f (~ 1 Hz), modifying Eq. 2.1 as

$$V_{coil} = 2\pi f A \sin(\omega t) \mu_0 (H + M), \quad (2.2)$$

where A is the amplitude of oscillation, and μ_0 is the vacuum permeability. Hence, $\chi = M/H$ is determined experimentally by solving Eq. 2.2 for M at some H and temperature

T , where H is provided by the superconducting magnet placed below the sample holder. Two techniques are commonly used when measuring χ with T , which may lead to different behaviors of the resulting curves: field-cooling (FC) and zero field-cooling (ZFC). For FC, a constant H is applied throughout the entire cooling process. Conversely, for ZFC, the sample is cooled down to some T in zero-field ($H = 0$), afterwards H is applied. This is then repeated for each T in the cooling process.

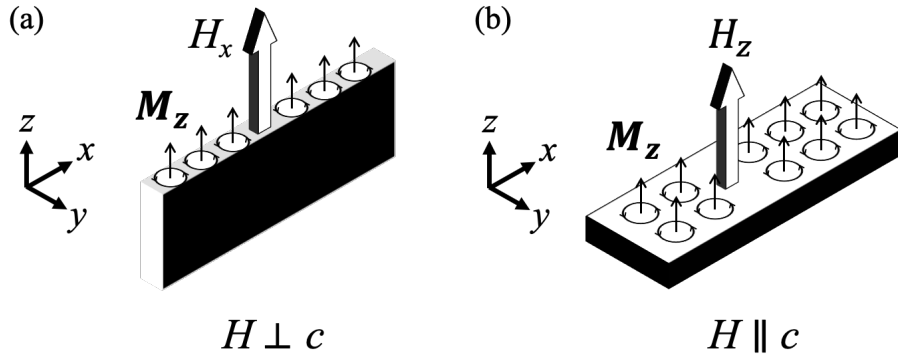


Figure B.3: *Illustration of the alignment for measuring direct current (DC) magnetic susceptibility $\chi = M / H$. (a) Alignment for $H \perp c$ where the edge of the plate-like sample is parallel to $M \parallel H$ along z , which is perpendicular to the surface of the coilset puck. The small arrows with circular orbits represent magnetic moments for illustrational purposes. (b) Alignment for $H \parallel c$ where the surface of the plate-like sample is parallel to $M \parallel H$ along z .*



Figure B.4: Quantum Design Dynacool Physical Property Measurement System (PPMS) with a 9 T magnet. The DC magnetization (DCM) linear motor is shown by the small cylinder placed on top of the PPMS. Below is the chamber where the sample is located at the end of a long rod where high magnetic fields (up to 9 T) and low temperatures (down to 1.8 K) can be achieved.

The χ dependence on T measured by FC with $H \parallel c$ at $\mu_0 H = 0.1$ T is plotted in Fig. 2.5(a) for a single crystal of YMn_6Sn_6 . At 345 K, a distinct peak is observed corresponding to T_N for the grown sample of YMn_6Sn_6 , in good agreement with previous studies [Table 1.1] [13, 14, 15, 17], below which, the commensurate collinear AFM structure forms. A small notch in χ is present at 333 K, which arises from a change in the magnetic structure via the emerging incommensurate phase upon cooling as previously revealed by Venturini et. al. [16] via neutron diffraction. The χ dependence on T by both FC and ZFC with $H \perp c$ and $H \parallel c$ at $\mu_0 H = 0.1$ T is plotted in Fig. 2.4(b) for a single crystal of TbMn_6Sn_6 . The sharp transition near $T_{sr} \approx 308$ K corresponds to the spin-reorientation transition temperature. The moments align predominantly along the c-axis above the vicinity of T_{sr} [$\chi(350 \text{ K})_{ZFC, H \perp c} / \chi(350 \text{ K})_{ZFC, H \parallel c} \approx 13$] and along the c-axis

below the vicinity of T_{sr} [$\chi(250 \text{ K})_{ZFC, H \parallel c} / \chi(250 \text{ K})_{ZFC, H \perp c} \approx 50$]. The reduction of the ZFC response of χ with $H \parallel c$ at low temperatures is likely due to the existence of FiM domains within the sample which tend to anti-align during ZFC, as noted by Guguchia et. al. [24].

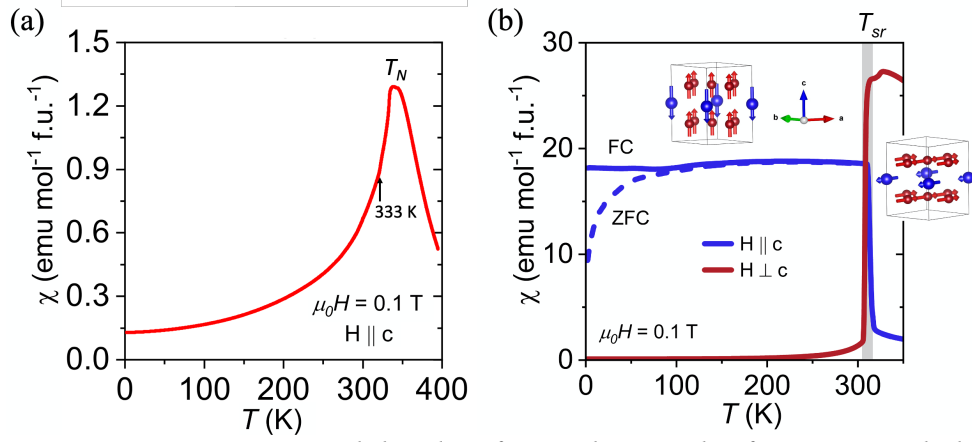


Figure B.5: DC magnetic susceptibility data for single crystals of YMn_6Sn_6 and $TbMn_6Sn_6$. (a) Temperature dependence DC magnetic susceptibility $\chi = M/H$ measured by zero-field-cooling (ZFC) with $H \parallel c$ at $\mu_0 H = 0.1 \text{ T}$ for a single crystal of YMn_6Sn_6 . The peak at $T_N \approx 333 \text{ K}$ corresponds to the Neel temperature for YMn_6Sn_6 and the arrow at 333 K corresponds to an emerging incommensurate phase upon cooling. (b) Temperature dependence of χ measured by both ZFC and field-cooling (FC) with $H \perp c$ and $H \parallel c$ at $\mu_0 H = 0.1 \text{ T}$ for a single crystal of $TbMn_6Sn_6$. The two cubic graphics illustrate the crystallographic orientations of the Tb and Mn magnetic moments below (along the c-axis) and above (perpendicular to the c-axis) the vicinity of the spin-reorientation transition temperature T_{sr} from left to right, respectively.

1.6 Electrical Transport Measurements

To characterize the zero-field electronic properties of single crystals of YMn_6Sn_6 and $TbMn_6Sn_6$ along the plane of the Mn kagome lattices [Fig. 1.6], electrical transport measurements are performed with the electrical current $I \perp c$. The single crystal samples

of YMn_6Sn_6 and TbMn_6Sn_6 are trimmed to adequate dimensions with a large surface area to thickness ratio where the surface is perpendicular to the c -axis. The trimmed samples are glued onto to a puck with GE-varnish separated by a sapphire block and five or six 25-micron platinum wire contacts are placed using Epotek H20E silver epoxy. The Hall-bar geometry, shown for a polished sample of YMn_6Sn_6 in Fig. 2.6(a) with six contacts are attached, is used for the electrical transport measurement. Longitudinal voltage (V_x) and Hall voltage (or transverse voltage) (V_y) are then measured on the same sample with a four-probe method, as shown in Fig. 2.6(b). For both measurements, the two contacts at the long edges of the sample pass a current I through the sample. While a separate set of leads placed longitudinally (transversely) in between measure the voltage drop V_x (V_y) across a region of the sample in the x -direction (y -direction). Ideally, the voltage leads should be arranged in-line with the current leads such that the electrical field lines remain parallel. The resistances between all contacts are also tested to prevent an electrical short circuit. The puck is next slowly placed into the PPMS [Fig. 2.4] where V_x and V_y are measured using the electrical transport option.

The electrical resistance R_{xx} is calculated using Ohm's law:

$$R_{xx} = \frac{V_x}{I}. \quad (2.3)$$

The electrical resistivity ρ_{xx} is then calculated by the following geometric relation:

$$\rho_{xx} = \frac{A_x}{l} R_{xx} = \frac{A_x}{l \cdot I} V_x, \quad (2.4)$$

where A_x is the cross-sectional area normal to the x -direction through which the current I passes and l is the length between the closest edges of the silver epoxy which attaches the voltage contacts to the sample [left of Fig. 2.6(a)].

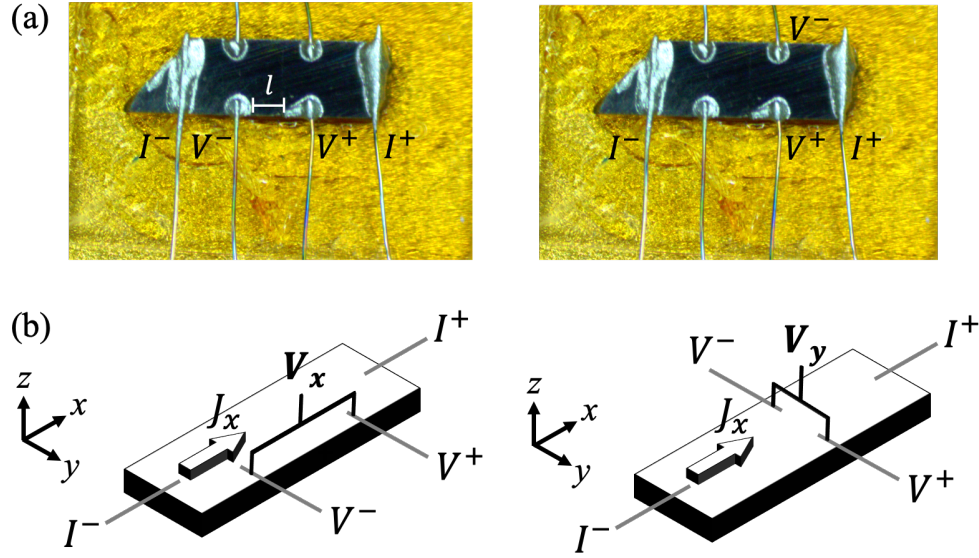


Figure 2.6: *Electrical transport measurements.* (a) A polished sample of YMn_6Sn_6 with six platinum wire contacts placed using Epotek H20E silver epoxy in a Hall-bar geometry for measuring longitudinal voltage V_x (left) and Hall voltage V_y (right) using the four-probe method shown in (b). l is the distance between the closest edges of the silver epoxy which attaches the longitudinal contacts to the sample. w is the width of the sample. (b) Illustrations of the four-probe configurations with contacts shown by the gray lines. The electrical current for electrons flows from I^- to I^+ with electrical current density J_x and V_x (left) and V_y (right) are measured across V^- and V^+ .

The ρ_{xx} dependence on temperature T with $I \perp c$ is plotted in Fig. 2.7(a) and (b), for single crystals of YMn_6Sn_6 and TbMn_6Sn_6 , respectively. Both YMn_6Sn_6 and TbMn_6Sn_6 are shown to have exhibit high metallicity with the residual resistivity ratio $RRR = \rho_{xx}(350 \text{ K})/\rho_{xx}(2 \text{ K}) \approx 46$ and 78 for YMn_6Sn_6 and TbMn_6Sn_6 , respectively. The strong

decrease of ρ_{xx} with decreasing T [Fig. 2.7(a) and (b)] is a well-defined signature of a metallic system, suggesting that relatively long-range exchange interactions likely play a significant role. Moreover, the large values of RRR suggest that the grown single crystal samples possess low impurities as the resistivity is relatively small within the low temperature regime where lattice vibrations become insignificant. The first derivative of ρ_{xx} with respect to temperature for YMn_6Sn_6 and TbMn_6Sn_6 [insets of Fig. 2.7(a) and (b), respectively] reveals the distinct magnetic transitions at 333 K and 308 K, as previously revealed in Fig. 2.5(a) and (b), respectively. For YMn_6Sn_6 , the drop in $d\rho_{xx}/dT$ at 333 K again corresponds to the temperature at which the incommensurate phase emerges upon cooling [Fig. 2.5(a)] for the grown sample. For TbMn_6Sn_6 , $d\rho_{xx}/dT$ displays a distinct peak at $T_{sr} = 308$ K again denoting the spin-reorientation transition at zero-field [Fig. 2.5(b)] for the grown sample.

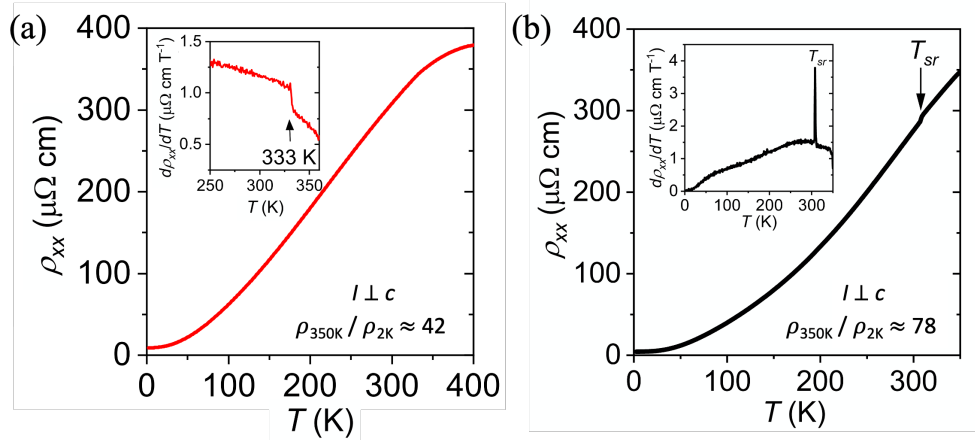


Figure B.6: *Electrical transport data for single crystals of YMn_6Sn_6 and TbMn_6Sn_6 .* (a) Temperature dependence of electrical resistivity for YMn_6Sn_6 with $I \perp c$, yielding a residual resistivity ratio $RRR = \rho_{xx}(350 \text{ K}) / \rho_{xx}(2 \text{ K}) \approx 46$. The inset shows the temperature dependence of the first derivative of the electrical resistivity with respect to temperature where the sudden drop represents the temperature below which the incommensurate phase emerges. (b) Temperature dependence of electrical resistivity for TbMn_6Sn_6 with $I \perp c$, yielding a residual resistivity ratio $RRR = \rho_{xx}(350 \text{ K}) / \rho_{xx}(2 \text{ K}) \approx 78$. The inset shows the temperature dependence of the first derivative of the electrical resistivity with respect to temperature where the peak represents the spin reorientation process temperature T_{sr} at zero-field.

Chapter 3: Magnetic Properties of YMn_6Sn_6 and TbMn_6Sn_6

1.7 Magnetization Measurements

The H dependence of M with $H \perp c$ and $H \parallel c$ for a single crystal of TbMn_6Sn_6 at several temperatures is shown in Figs. 3.1(b) and (c), respectively. For $H \perp c$ [Fig. 3.1(b)], the shape of the curves displays soft FM behavior above T_{sr} via a sharp increase at low fields followed by saturation at higher fields. For $H \parallel c$ [Fig. 3.1(c)], the curves also display soft FM behavior below T_{sr} , but then quickly change to hard FM behavior near 250 K via the emergence of hysteresis loops containing asymmetric steps, which increase in width, with a large coercive field of around $\mu_0 H_c = 2$ T at 2 K [inset of Fig. 3.1(c)]. The mechanism behind the asymmetry steps is unknown at present but may be related to the presence of FiM domains. The saturation magnetization M_{sat} reaches approximately $3.9 \mu_B/\text{f.u.}$ at 2 K and increases up until around 300 K [inset of Fig. 3.1(c)]. The magnetization curves for $T < T_{sr}$ with $H \perp c$ [Fig. 3.1(b)] and $T > T_{sr}$ with $H \parallel c$ [Fig. 3.1(c)] exhibit a dramatic jump at the field $H = H_{sr}$ at which induces the spin-reorientation transition.

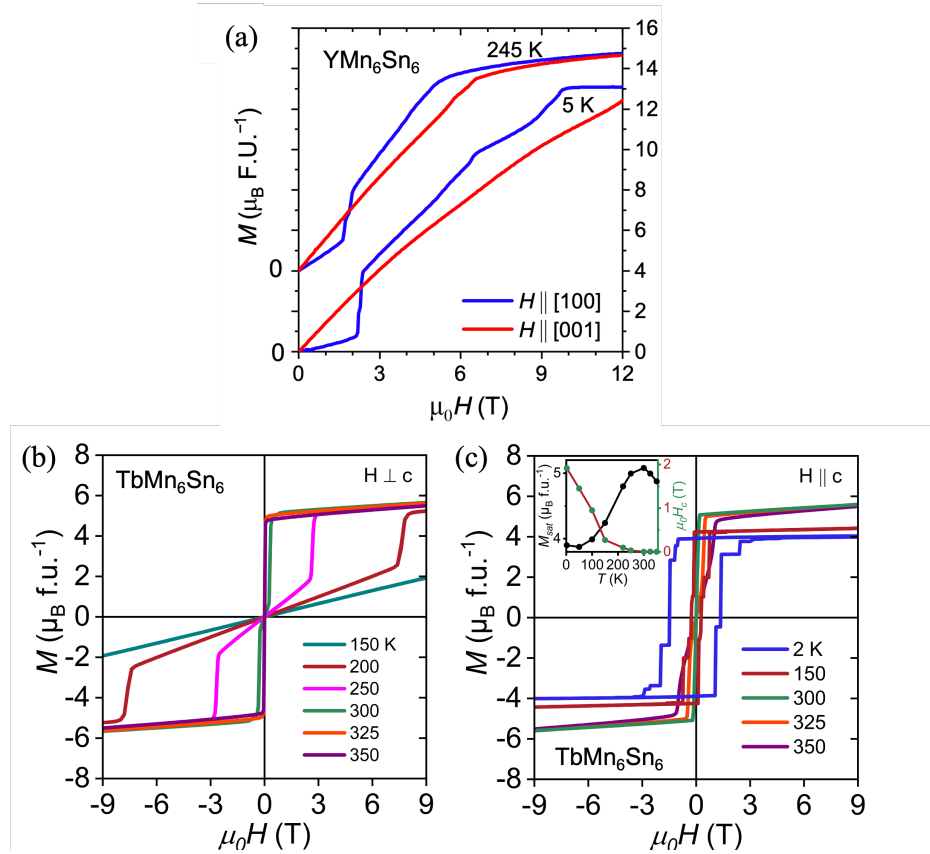


Figure C.1: Magnetization data for single crystals of YMn_6Sn_6 and $TbMn_6Sn_6$. (a) External field dependence of magnetization for YMn_6Sn_6 with $H \perp c$ (blue) and $H \parallel c$ (red) at 5 K and 245 K*. (b) External field dependence of magnetization $TbMn_6Sn_6$ with $H \perp c$. (c) External field dependence of magnetization for $TbMn_6Sn_6$ with $H \parallel c$ using our 9 T Quantum Design PPMS. The inset shows the temperature dependence of saturation magnetization and coercive field.

1.8 Magnetic Phase Diagrams

To map the distinct competing magnetic phases dependent on T and H , as evident in the magnetization data for discrete temperatures [Fig. 3.1], magnetic phase diagrams are now constructed for YMn_6Sn_6 and $TbMn_6Sn_6$. Due to the complexity of the magnetic phase

*Magnetization measurement performed by Michael A. McGuire at the Oak Ridge National Laboratory using a 14 T Quantum Design PPMS.

transitions in YMn_6Sn_6 for $H \perp c$ [Fig. 3.1(a)], alternating current (AC) susceptibility, defined as the differential response $\chi_{AC} = dM/dH$ to M , is measured in place of the DC susceptibility χ using the ACMS II in the Quantum Design PPMS [Fig. 2.4]. In addition to the applied field supplied by the PPMS superconducting magnetic, however, a small AC drive magnetic field is superimposed at high values of f (10 – 10,000 Hz) where χ_{AC} is then measured within a narrow frequency band using Eq. 2.2. The constructed AC susceptibility phase diagram for TbMn_6Sn_6 with $H \perp c$ between 4 and 380 K is shown in Fig. 3.2(a), revealing several magnetic phase boundaries marked by the peaks in χ_{AC} . Following the construction of Fig. 3.2(a), the structures of these distinct magnetic phases in YMn_6Sn_6 were determined [15] with $H \perp c$ and are the distorted spiral (DS) ($0 < H < H_1$), transverse conical spiral (TCS) ($H_1 < H < H_2$), fan-like (FL) ($H_2 < H < H_3$), and polarized forced-ferromagnetic (FF) ($H_3 < H$), as labeled in Fig. 3.2(b) and their magnetic structures along the c-axis are illustrated in Fig. 3.2(b). The narrow intermediate phases I and II exist between the FL and FF phases and between the TCS and FF phases, respectively, and are likely complex mixtures of these phases. For $H \parallel c$, the magnetic phases are more trivial: the helical spiral gradually becomes a longitudinal conical spiral (LCS) upon increasing $H \parallel c$ [15], which is a spin-reorientation TCS-type phase but parallel to the c-axis, eventually saturating into a polarized FF along the c-axis at high H [Fig. 3.2(a)].

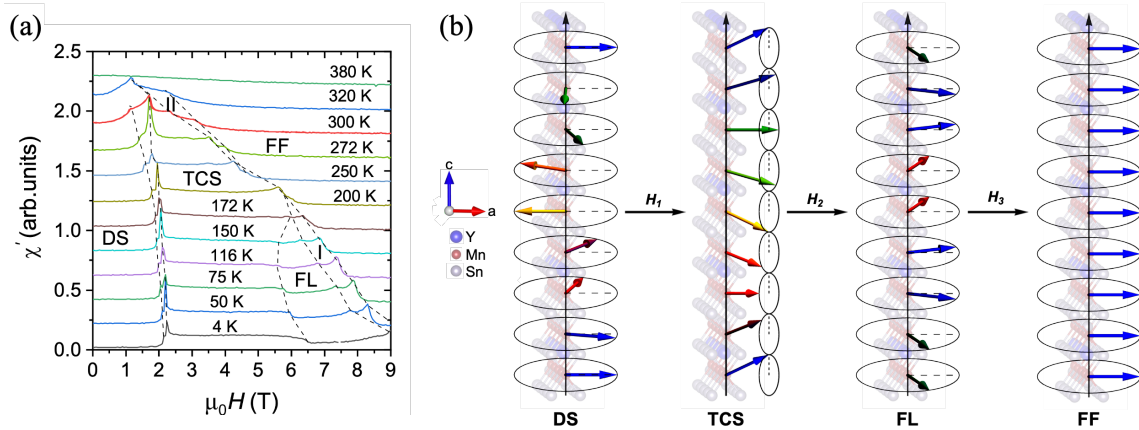


Figure C.2: *Magnetic phases in YMn_6Sn_6 with $H \perp c$.* (a) Magnetic phase diagram constructed from AC susceptibility measurements. The four magnetic phases are distorted spiral (DS) ($0 < H < H_1$), transverse conical spiral (TCS) ($H_1 < H < H_2$), fan-like (FL) ($H_2 < H < H_3$), and forced-ferromagnetic (FF) ($H_3 < H$). The narrow intermediate phases I and II exist between the FL and FF phases and between the TCS and FF phases. Phase I is now known to be a mixed phase of commensurate and incommensurate magnetic structure, the nature of which is yet to be determined. Phase II is known to be a canted antiferromagnet (CAF) state [35]. (b) Illustration of the four magnetic phases in YMn_6Sn_6 as determined by neutron scattering* and first principles calculations [15].

For $TbMn_6Sn_6$, the magnetic phase transitions with $H \perp c$ and $H \parallel c$ [Fig. 3.1(b) and (c)] below $T_N \approx 423$ K are simply the two distinct FiM phases with in-plane and out-of-plane magnetization separated by the spin-reorientation transition $T_{sr} \approx 308$ K [Fig. 2.4] and the spin-reorientation transition field H_{sr} with changing temperature. M and dM/dH dependence on H with $H \perp c$ and $H \parallel c$ for single crystals of $TbMn_6Sn_6$ are shown in Fig. 3.3 for various temperatures within the vicinity of T_{sr} . At $H = H_{sr}$, dM/dH reaches a maximum via a first order magnetization process (FOMP), allowing for the extraction of

*Neutron scattering performed by Lekh Poudel, Rebecca Dally, and Jeffrey Lynn using a triple-axis neutron spectrometer BT-7 at the National Institute of Standard and Technology (NIST) Center for Neutron Research.

H_{sr} as a function of T , which leads to the magnetic phase diagram for TbMn_6Sn_6 shown in Fig. 3.4.

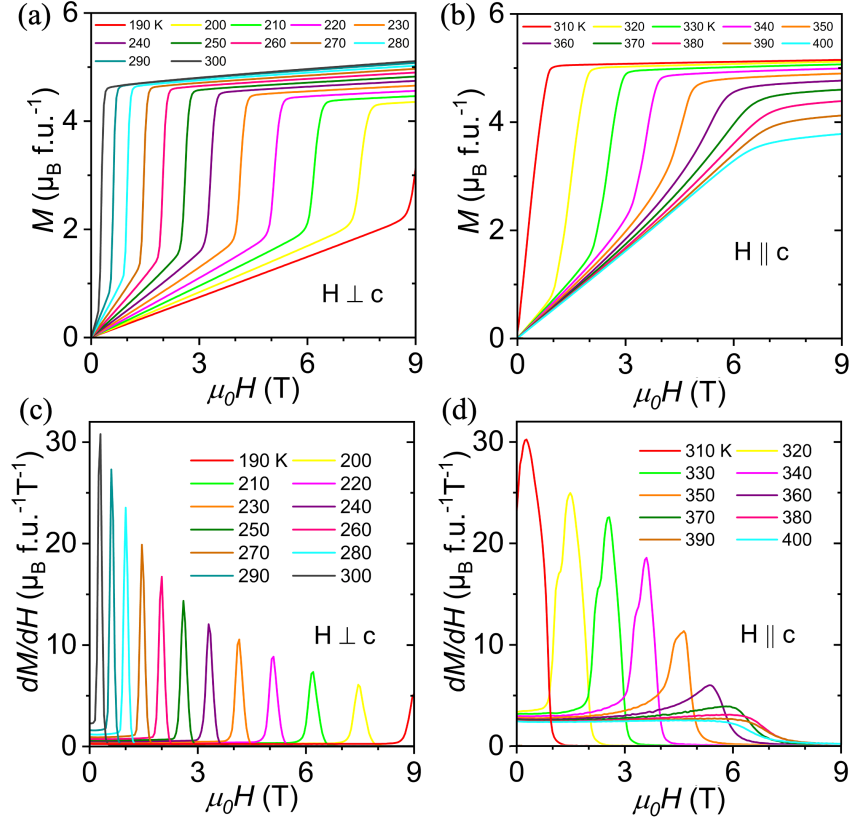


Figure C.3: *First Order Magnetization Process (FOMP) in TbMn_6Sn_6 . M dependence on H with (a) $H \perp c$ and (b) $H \parallel c$ for various temperatures within the vicinity of the spin-reorientation transition temperature T_{sr} . dM/dH dependence on H with (c) $H \perp c$ and (d) $H \parallel c$ for various temperatures within the vicinity of T_{sr} .*

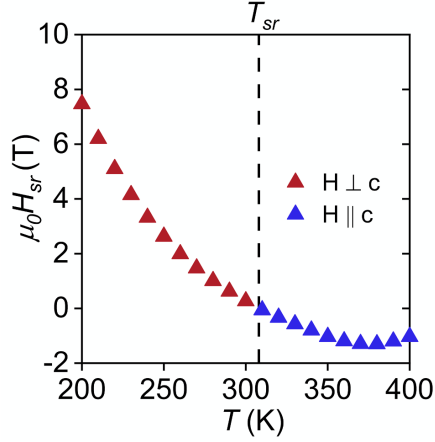


Figure C.4: Constructed magnetic phase diagram from magnetization measurements [Fig. 3.3] for TbMn₆Sn₆. H_{sr} is the field at spin-reorientation transition field and T_{sr} is the spin-reorientation transition temperature.

1.9 Magnetic Anisotropy: First-Principle Calculations

We now explore the magnetic anisotropy within YMn₆Sn₆ and TbMn₆Sn₆ using first-principles calculations. For YMn₆Sn₆, the competing magnetic phases which compete with T and $H \perp c$ [Fig. 3.2] can be quantitatively described by the interplanar exchange interactions J_1 , J_2 , and J_3 [20]. By constructing a mean field theory at $T = 0$, density functional theory (DFT) total energy calculations for YMn₆Sn₆* [15] are performed and fit to the Hamiltonian is given by

$$\mathcal{H}_{MF} = \sum_{i,j} J_n \vec{n}_{Mn,i} \cdot \vec{n}_{Mn,j} + \sum_{i,j} J_p \vec{n}_{Mn,i} \cdot \vec{n}_{Mn,j} + MAE_{Mn} + \sum_i \mu_0 \vec{H} \cdot \mu_B M_{Mn} \vec{n}_i, \quad (3.1)$$

where μ_B is the Bohr magneton. By considering Heisenberg exchange interactions, the first and second sums run over the six nearest-neighbors along the c-axis and the over the three nearest-neighbors within the ab-plane, respectively. The third term considers magnetic anisotropy energy for all nearest-neighbor neighbors by lumping the Ising-type exchange

(moments along the c-axis) and the single-ion anisotropy terms into the single term given by

$$MAE_{Mn} = \sum_i J^z n_{Mn,i}^z n_{Mn,i+1}^z + K_{Mn} M_{Mn}^2 \sum_i (n_{Mn,i}^z)^2, \quad (3.2)$$

where K_{Mn} is the easy-plane anisotropy coefficient for the Mn kagome sublattice. The last term in Eq. 3.1 is the single-site Zeeman energy. A Hubbard correlation is also considered by adding a DFT + U correction with $U - J = 0.4$ eV. The DFT results at $T = 0$ are shown in Fig. 3.5 with $J_1 = -50.9$ meV (AFM), $J_2 = +18.5$ meV (FM), and $J_3 = +8.7$ meV (FM), which quantitatively describes the magnetic phase diagram constructed for YMn_6Sn_6 for $H \perp c$ [Fig. 3.2].

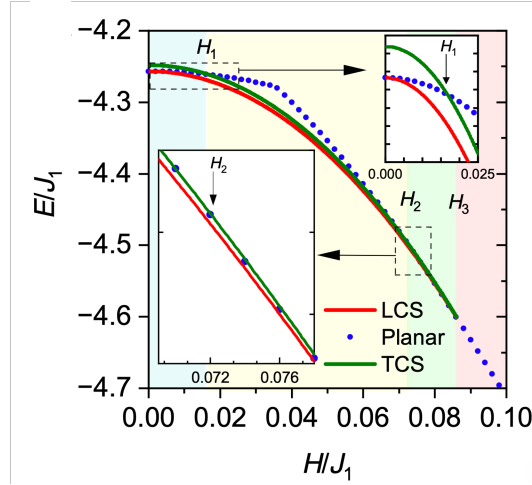


Figure C.5: Reduced energies E / J_1 for the magnetic phases with $H \perp c$ as a function of reduced magnetic field H / J_1 calculated using density functional theory (DFT) calculations using mean field theory calculations [20]. The planar phase, shown in blue, comprises of the distorted spiral (DS) phase ($0 < H < H_1$), fan-like (FL) phase ($H_2 < H < H_3$) and polarized forced-ferromagnetic (FF) phase ($H_3 < H$). The transverse conical spiral (TCS) ($H_1 < H < H_2$) is shown in green. The longitudinal conical spiral (LCS) phase, shown in red, exists only for $H \parallel c$ and is a spin-reorientation TCS phase along the c -axis.

At the transition between the DS and TCS phases ($H = H_1$), the DFT calculations using Eq. 3.1 also calculates $MAE_{Mn} \sim 20$ meV. To solve for K_{Mn} in Eq. 3.2, we now approximate J^z by analyzing data obtained from single crystal neutron diffraction on YMn_6Sn_6 shown in Fig. 3.6 at 100 K about $(0, 0, 2 - k_{z,n})$ ($n = 1, 2$) with k_z being wavevector of the magnetic spirals along the c -axis. At $H = H_1$, k_z is increased by ~ 2.5 % obtained by the Gaussian fits to the data which can be explained by an increase in $\alpha + \beta$ [Fig. 1.9] given by

$$\alpha + \beta \approx \cos^{-1} \left(\frac{J_1 J_2}{8J_3^2} - \frac{J_2}{2J_1} - \frac{J_1}{2J_2} \right). \quad (3.3)$$

*Density functional theory (DFT) total energy calculations for YMn_6Sn_6 performed by Igor I. Mazin at George Mason University.

By assuming that the dominant contribution of J^z resides in the largest J , which is J_1 (FM), we approximate $J^z \approx dJ_1$ at $H = H_1$, allowing one to solve for J^z :

$$J^z \frac{d\cos(\alpha+\beta)}{dJ_1} = \frac{d}{dJ_1} \left(\frac{J_1 J_2}{8J_3^2} - \frac{J_2}{2J_1} - \frac{J_1}{2J_2} \right) = \frac{J_2}{8J_3^2} + \frac{J_2}{2J_1^2} - \frac{1}{2J_2} \approx 2.5 \%. \quad (3.4)$$

Eq. 3.4 yields $J^z \approx + 0.34$ meV (AFM) and when finally plugged into Eq. 3.2 yields $K_{Mn} M_{Mn}^2 \approx - 0.12$ meV / Mn. The negative sign of K_{Mn} indicates that the Mn- sublattice favors the easy-magnetization direction along the plane which we will next use compare to the magnetic anisotropy for TbMn_6Sn_6 .

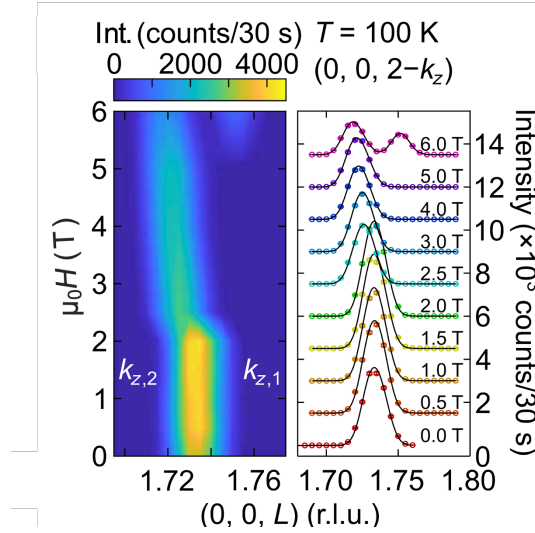


Figure C.6: Magnetic field dependence of incommensurate magnetic Bragg peaks $(0, 0, 2 - k_{z,n})$ ($n = 1,2$) at 100 K obtained from single crystal neutron diffraction on YMn_6Sn_6 *. The solid black lines in the right panel are the corresponding Gaussian fits.

*Neutron scattering performed by Lekh Poudel, Rebecca Dally, and Jeffrey Lynn using a triple-axis neutron spectrometer BT-7 at the National Institute of Standard and Technology (NIST) Center for Neutron Research.

Let us now explore the microscopic nature of the constructed magnetic phase diagram for TbMn₆Sn₆ [Fig. 3.4] by considering a simplified description of the collinear configuration on magnetic single-site anisotropy. By lumping the Heisenberg exchange and single-site anisotropy terms into a single term, the temperature dependence on magnetic anisotropy energy for the collinear arrangement of the moments on the Tb- and Mn-sublattices will be approximated by

$$\mathcal{H}_{anis}(T) = 6MAE_{Mn}(T) + MAE_{Tb}(T). \quad (3.5)$$

We now derive an expression for MAE_i ($i = \text{Mn, Tb}$) on the classical (Langevin) level [35]. The standard partition function for $H \parallel z$, assuming the anisotropy is a small correction to the Zeeman term is given by

$$Z = \int_0^{2\pi} d\varphi \int_0^\pi e^{-(-HM_z)\beta} \sin \theta d\theta \quad (3.6)$$

$$= 2\pi \int_0^\pi e^{\beta HM \cos \theta} \sin \theta d\theta \quad (3.7)$$

$$= 2\pi \frac{2 \sinh(\beta HM)}{\beta HM}, \quad (3.8)$$

where φ is the azimuthal angle, θ is the polar angle (angle made with the z -axis), and $\beta = k_B T$ with k_B being the Boltzmann constant.

The expectation value for the total magnetic moment in the z -direction $M_z = M \cos \theta$ is then

$$m = \langle M_z \rangle = \frac{1}{Z} \int_0^\pi M \cos \theta e^{\beta HM \cos \theta} \sin \theta d\theta \quad (3.9)$$

$$= M \coth(\beta HM) - \frac{1}{\beta H} \quad (3.10)$$

$$= ML(\alpha), \quad (3.11)$$

where $L(\alpha)$ is the Langevin function defined by $L(\alpha) = \coth(\alpha) - 1/\alpha$ with $\alpha = \beta HM$. In the limit $H \rightarrow \infty$ or $T \rightarrow 0$, $L(\alpha) \rightarrow 1$ and thus $m \rightarrow M$. In the other extreme, $H \rightarrow 0$ or $T \rightarrow \infty$, $L(\alpha) \rightarrow 0$ and thus $m \rightarrow 0$.

If $c \parallel z$, then the anisotropy energy with anisotropy coefficient K can be approximated (to the second order) as

$$E = KM_z^2 = KM^2 \cos^2 \theta. \quad (3.12)$$

For the easy axis parallel to H , the expectation value of the anisotropy energy is

$$E_{\parallel} = \frac{1}{Z} \int_0^{2\pi} d\varphi \int_0^{\pi} KM^2 \cos^2 \theta e^{\beta HM \cos \theta} \sin \theta d\theta \quad (3.13)$$

$$= \frac{2K}{(\beta H)^2} + KM^2 - \frac{2KM \coth(\beta HM)}{(\beta H)^2} \quad (3.14)$$

$$= KM^2 - \frac{2K}{\beta H} m \quad (3.15)$$

For the easy axis perpendicular to H , the expectation value of the anisotropy energy is

$$E_{\perp} = \frac{1}{Z} \int_0^{2\pi} \int_0^{\pi} KM^2 \sin^2 \theta \cos^2 \varphi e^{\beta HM \cos \theta} \sin \theta d\varphi d\theta \quad (3.16)$$

$$= \frac{KM \coth(\beta HM)}{\beta H} - \frac{K}{(\beta H)^2} = \frac{K}{\beta H} m. \quad (3.17)$$

The effective anisotropy energy is therefore

$$\Delta E = E_{\parallel} - E_{\perp} = KM^2 - \frac{3K}{\beta H} m. \quad (3.18)$$

To eliminate H , we solve the transcendental equation [Eq. 3.10] for H , by rewriting as

$$\mu = \coth(\alpha) - \frac{1}{\alpha} \quad (3.19)$$

where $\mu = m/M$. One finds solutions for $\mu \rightarrow 0$ and $\mu \rightarrow 1$ by interpolating between the two:

$$\alpha = \mu \left(2 - \mu + \frac{1}{1-\mu} \right) \quad (3.20)$$

$$H = \frac{m}{\beta M^2} \left(2 - \frac{m}{M} + \frac{M}{M-m} \right) \quad (3.21)$$

$$\Delta E = KM^2 - 3K \frac{M^2}{2 - \frac{m}{M} + \frac{M}{M-m}} \quad (3.22)$$

$$= Km^2 \frac{M^2}{3M^2 - 3Mm + m^2} \quad (3.23)$$

Note that $\Delta E \rightarrow Km^2$ at $T = 0$, where $m = M$, and $\Delta E \rightarrow Km^2$ at $T = T_N$.

Finally, MAE_i can now be written as

$$MAE_i(T) = K_i M_i^2(0) \frac{M_i^2(T)}{3M_i^2(T) - 3M_i(T)M_i(0) + M_i^2(0)}, \quad (3.24)$$

where M_i and K_i are the magnetic moments and the 2nd order anisotropy coefficients for the two atoms and sublattices ($i = \text{Mn, Tb}$), respectively. The temperature dependence for M_{Mn} and M_{Tb} are shown in Fig. 3.7(b), produced by fitting Brillouin curves, as shown in Fig. 3.8, with the form $a[1 - (T/T_N)^b]^c$ where $T_N = 423$ K, to experimental data from a previous neutron powder diffraction study by Malaman et al. [14].

By equating \mathcal{H}_{anis} [Eq. 3.5] using the derived expression for MAE_i [Eq. 3.24] to the single-site Zeeman energy at $H = H_{sr}$ given by

$$\mathcal{H}_{zeeman}(T, H_{sr}) = [M_{\text{Tb}}(T) - 6M_{\text{Mn}}(T)]\mu_B\mu_0 H_{sr}(T), \quad (3.25)$$

a fitted curve for $H_{sr}(T)$ separating the two distinct FiM phases in YMn_6Sn_6 is generated in Fig. 3.7(a) with $K_{\text{Mn}} = -8.96 \times 10^{-2} \text{ meV} / \mu_B^2$ and $K_{\text{Tb}} = 0.136 \text{ meV} / \mu_B^2$. The negative(positive) sign of $K_{\text{Mn}}(K_{\text{Tb}})$ indicates that the Mn-(Tb-) sublattice favors the easy-magnetization direction along the plane (c-axis) likely due to hexagonal crystal field splitting on the 3d-(4f-)orbital kagome (triangular) lattice. Moreover, because Tb^{3+} is a

heavier ion, the magnitude of K_{Tb} is significantly larger than K_{Mn} , thereby contributing greater to \mathcal{H}_{anis} for a given M_i . Therefore, the remarkable agreement of the fitted curve [Fig. 3.7(a)] with the experimental data reveals that the spin-reorientation magnetic phase diagram is quantitatively described by the temperature dependencies of M_{Mn} and M_{Tb} [Fig. 3.7(b)]. The calculated values for MAE_{Mn} and MAE_{Tb} as functions of temperature are shown in Fig. 3.7(b). Akin to M_{Mn} and M_{Tb} , respectively, MAE_{Mn} remains relatively constant from around 300 K down to zero temperature whereas MAE_{Tb} dramatically increases with decreasing temperature. At T_{sr} , $MAE_{Mn} \approx -MAE_{Tb}$, revealing that the spin reorientation transition in zero-field occurs when the two competing anisotropy energies of the two sublattice FiM system cancel out. In ground state, $MAE_{Mn}(0) \approx -0.47$ meV per Mn and $MAE_{Tb}(0) \approx 10.0$ meV per Tb. To understand the contributions of Heisenberg exchange and single-site anisotropy terms within MAE_{Mn} , we compare with the YMn_6Sn_6 compound. As previously demonstrated, the estimated magnetic anisotropy for YMn_6Sn_6 in ground state was estimated to be $MAE_{Mn}(0) \approx -0.12$ meV per Mn atom. By assuming the single-site anisotropy on Mn- and Tb-sublattices coexist independently, the larger magnitude and sign of MAE_{Mn} for $TbMn_6Sn_6$ likely arises from the necessary J_{Mn-Tb} component [Fig. 1.8(a)].

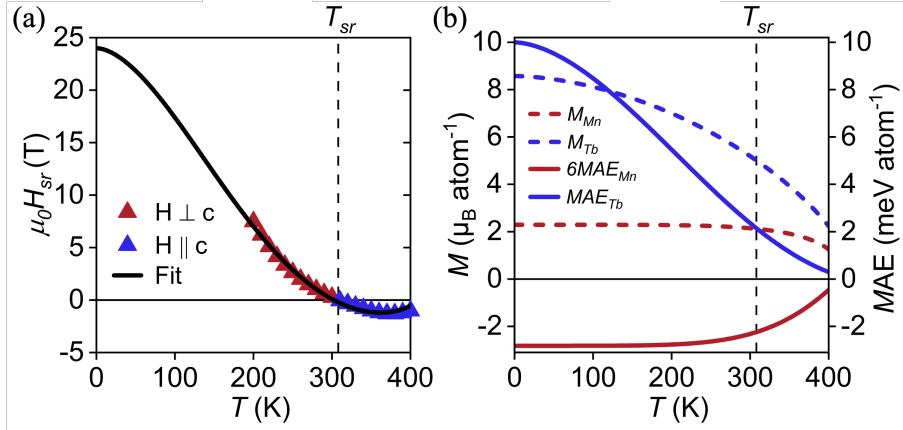


Figure C.7: *Magnetic Anisotropy Analysis for TbMn₆Sn₆*. (a) Magnetic phase diagram for the spin-reorientation transition. Positive values for $\mu_0 H_{sr}$ correspond to $H \perp c$ whereas negative values correspond to $H \parallel c$. The fitted curve with $K_{Mn} = - 8.96 \times 10^{-2} \text{ meV} / \mu_B^2$ and $K_{Tb} = 0.136 \text{ meV} / \mu_B^2$ is overlaid on top of the experimental values. The dashed vertical line represents the zero-field spin reorientation transition temperature T_{sr} . (b) Temperature dependence of the magnetic moments on Mn and Tb [$M_{Mn}(0) \approx 2.29 \mu_B$ and $M_{Tb}(0) \approx 8.57 \mu_B$] and magnetic anisotropy energies for the Mn- and Tb-sublattices [$MAE_{Mn}(0) \approx - 0.47 \text{ meV}$ per Mn and $MAE_{Tb}(0) \approx 10.0 \text{ meV}$ per Tb].

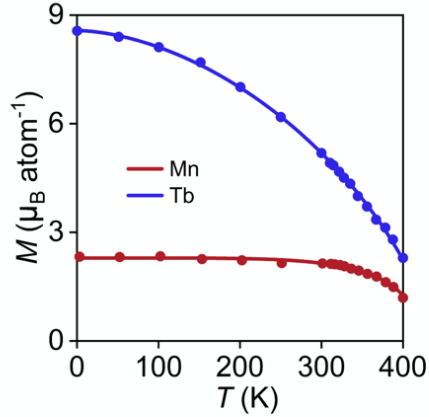


Figure C.8: Fit of Brillouin curves (solid lines) to experimental data (points) for the temperature dependence on the magnetic moments on Mn and Tb obtained from a previous neutron powder diffraction study by Malaman et al. [14].

Chapter 4: Magnetotransport Properties of YMn₆Sn₆ and TbMn₆Sn₆

The electrical resistivity ρ and conductivity σ for a given material are intrinsic properties which measure how a material resists and conducts electrical current, respectively. When ρ in a material is dependent on direction, it can be described by the tensor form of Ohm's law $\vec{E}_i = \rho_{ij}\vec{J}_i$ ($i = x, y, z$), written in matrix form as

$$\begin{bmatrix} E_x \\ E_y \\ E_z \end{bmatrix} = \begin{bmatrix} \rho_{xx} & \rho_{xy} & \rho_{xz} \\ \rho_{yx} & \rho_{yy} & \rho_{yz} \\ \rho_{zx} & \rho_{zy} & \rho_{zz} \end{bmatrix} \begin{bmatrix} J_x \\ J_y \\ J_z \end{bmatrix}, \quad (4.1)$$

where \vec{E}_i is the electrical field vector, ρ_{ij} is the resistivity tensor, and \vec{J}_i is the electrical current density vector. σ is similarly described by $\vec{J}_i = \sigma_{ij}\vec{E}_i$ ($i = x, y, z$), written in matrix form as

$$\begin{bmatrix} J_x \\ J_y \\ J_z \end{bmatrix} = \begin{bmatrix} \sigma_{xx} & \sigma_{xy} & \sigma_{xz} \\ \sigma_{yx} & \sigma_{yy} & \sigma_{yz} \\ \sigma_{zx} & \sigma_{zy} & \sigma_{zz} \end{bmatrix} \begin{bmatrix} E_x \\ E_y \\ E_z \end{bmatrix}, \quad (4.2)$$

where σ_{ij} is the conductivity tensor. Let us assume the electrical field in the z-direction $E_z = 0$, which yields from Eq. 4.1 and 4.2:

$$E_x = \rho_{xx}J_x + \rho_{xy}J_y \quad (4.3)$$

$$E_y = \rho_{yx}J_x + \rho_{yy}J_y \quad (4.4)$$

$$J_z = \sigma_{xx}E_x + \sigma_{xy}E_y \quad (4.5)$$

$$J_y = \sigma_{yx}E_x + \sigma_{yy}E_y \quad (4.6)$$

Assuming an isotropic material, $\rho_{xx} = \rho_{yy}$ and $\rho_{yx} = -\rho_{xy}$, which plugged into Eqs. 4.3-4.6 yields the expressions relating ρ_{ij} and σ_{ij} :

$$\sigma_{xx} = \frac{\rho_{xx}}{\rho_{xx}^2 + \rho_{yx}^2} \quad (4.7)$$

$$\sigma_{xy} = \frac{\rho_{yx}}{\rho_{xx}^2 + \rho_{yx}^2} \quad (4.8)$$

1.10 Magnetoresistance Measurements

Magnetoresistance is a measure that describes a materials response to changes in electrical resistance in response to an externally applied field H . When the electrical current is along the x -direction I_x with electrical field E_x and the field is along the z -direction H_z , magnetoresistance MR is quantitatively defined as

$$MR(H_z) = \frac{\rho_{xx}(H_z) - \rho_{xx}(0)}{\rho_{xx}(H_z)} \times 100 \%, \quad (4.9)$$

which can be calculated in a material using the experimental setup in left of Fig. 2.6(b) where ρ_{xx} was given by Eq. 2.4.

The H dependence of MR up to 9 T with $H \parallel c$ and $I \perp c$ for YMn_6Sn_6 is shown in Fig. 4.1(a). At 300 K, MR is only negative for the entire field regime. Upon cooling to 250 K, MR starts to become positive at low fields, where at 80 K, it becomes only positive for the entire field regime. At 2 K, the positive MR behavior becomes present only at low H while the negative MR behavior becomes very large H (close to - 12 % at 9 T). The H dependence of MR up to 9 T with $H \parallel c$ and $I \perp c$ for TbMn_6Sn_6 is shown in Fig. 4.1(b). At 100 K, MR is negative at large H , while at lower temperatures, MR becomes both large

and positive with a transition from negative and positive between 70 and 100 K. This large and positive behavior at low temperatures (close to + 70 % at 1.8 K and 9 T) is distinct from the non-magnetic rare-earth YMn_6Sn_6 compound [Fig. 4.1(a)].

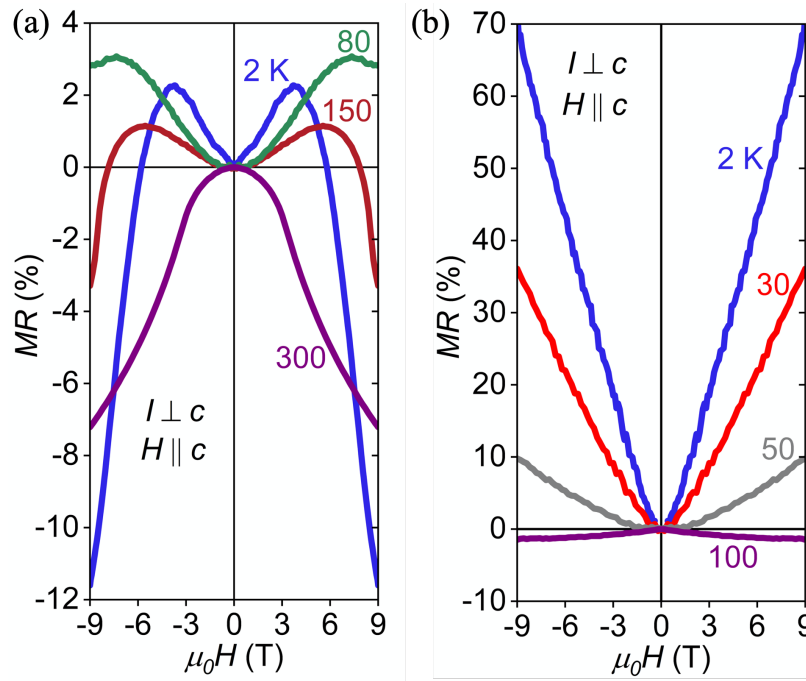


Figure D.1: Magnetoresistance in YMn_6Sn_6 and TbMn_6Sn_6 . External field dependence of magnetoresistance MR for (a) YMn_6Sn_6 and (b) TbMn_6Sn_6 with $H \parallel c$ and $I \perp c$. The inset for (a) shows MR at 100 K displays a “butterfly” effect in TbMn_6Sn_6 up to some field H_b where MR is positive when the field is increasing towards H_b and negative above.

To predict the underlying physics leading to the large and positive behavior in MR in TbMn_6Sn_6 , let’s consider how the magnetic moments on Tb and Mn atoms change with temperature in Fig. 3.8. The magnetic moments on the Tb atoms are greatly enhanced when decreasing temperature while the magnetic moments on the Mn atoms stay relatively constant [Fig. 3.8]. Assuming the itinerant electrons predominantly reside on the Mn-

kagome lattices when the current is perpendicular to the c-axis [Fig. 2.6], the enhanced state on the Tb atoms provides a larger induced magnetic field on the Mn-sublattice. This increased magnetic field likely shrinks the localized wave functions of the itinerant electrons and increases their hopping lengths, thereby increasing electron scattering and generating positive MR at lower temperatures, a characteristic of a strongly metallic system [37]. Since the Y-sublattice in $Y\text{Mn}_6\text{Sn}_6$ does not provide this large induced magnetic field on the Mn-sublattice as the Y atoms are effectively non-magnetic, the distinctly large and positive behavior is nonexistent in $Y\text{Mn}_6\text{Sn}_6$ [Fig. 4.1(a)].

1.11 Hall Measurements

For steady-state flow of electrons (or holes) in the x -direction, the net force on electrons (or holes) in the y -direction is balanced out by an induced electrical field \vec{E}_y , caused by transverse charge accumulation and the Lorentz force from \vec{B}_z [26], given as

$$\vec{F}_y = e\vec{E}_y + e\vec{v}_x \times \mu_0\vec{H}_z = 0, \quad (4.10)$$

where e is the electrical charge and \vec{v}_x is the electron drift velocity in the x -direction. Rearranging Eq. 4.10 gives $E_y = v_x\mu_0H_z$. Let us now consider measuring the Hall voltage V_y [right of Fig. 2.6(b)], across a segment in the y -direction of width w . Since we know E_y , the Hall voltage can be written as

$$V_y = wE_y = wv_x\mu_0H_z. \quad (4.11)$$

Assuming a Fermi gas, the current along the x -direction I_x , can also be written as

$$I_x = nA_xv_x(\pm e) = n(tw)v_x(\pm e), \quad (4.12)$$

where A_x is the cross-sectional area normal to the x -direction, n is the number of charge particles per unit volume (charge carrier density), t is the thickness of the sample along the z -direction, and \pm denotes whether the charge carriers are holes or electrons, respectively. Eq. 4.11 can now be rewritten as

$$V_y = \left(\pm \frac{1}{ne}\right) \frac{\mu_0 H_z I_x}{t} = \frac{I_x}{t} R_H \mu_0 H_z, \quad (4.13)$$

where $R_H = \pm 1/ne$ is known as the Hall coefficient, thereby the sign of R_H , and thus the polarity of V_y , can reveal the sign of the charge carriers.

By virtue of Ohm's law, the Hall resistance can be written as

$$R_{yx} = \frac{V_y}{I_x}, \quad (4.14)$$

which can be calculated for a material using the experimental setup illustrated in Fig. 4.2.

The Hall resistivity ρ_{yx} can therefore be calculated from experiment using

$$\rho_{yx} = t R_{yx} = t \frac{V_y}{I_x}, \quad (4.15)$$

which also can be written as a function of the applied field H by plugging in Eq. 4.13:

$$\rho_{yx} = R_H \mu_0 H_z. \quad (4.16)$$

In FM conductors, an additional contribution to the Hall resistivity ρ_{yx} , termed the anomalous Hall resistivity ρ_{yx}^{AH} , is present as a nonzero Hall voltage V_y is observed in the absence of an applied field H_z . This phenomenon is referred to as the anomalous Hall effect (AHE) [27]. An empirical relation established that ρ_{yx}^{AH} proportional to the sample magnetization along the z -direction M_z [39]:

$$\rho_{yx}^{AH} = R_S \mu_0 M_z, \quad (4.17)$$

where R_S is the anomalous Hall coefficient. Summing Eq. 4.17 to the “normal” Hall effect contribution in Eq. 4.16, the total Hall resistivity can now be rewritten in total as

$$\rho_{yx} = R_H \mu_0 H_z + \rho_{yx}^{AH} = R_H \mu_0 H_z + R_S \mu_0 M_z. \quad (4.18)$$

The two competing theories for the origins of the AHE are the extrinsic and intrinsic mechanisms [27]. The extrinsic mechanisms are termed side jump, where an impurity generates a lateral displacement of the electron perpendicular to its wavevector and spin, and skew-scattering, where an impurity causes SOC to break left-right symmetry. The intrinsic mechanism has been interpreted as electrons acquiring an “anomalous velocity” contribution to their group velocity perpendicular to an electric field [28]. This “anomalous velocity” depends only on the Hamiltonian of the perfect crystal and to non-zero Berry curvature effects [see *Appendix A.5: Intrinsic Anomalous Hall Effects*]. To predict these leading intrinsic and extrinsic contributions to the AHE, ρ_{yx}^{AH} can be approximately separated into the following scaling relations connected to ρ_{xx} [23]:

$$\rho_{yx}^{AH} = \rho_{yx,ext}^{AH} + \rho_{yx,int}^{AH} = (a_{sk} \rho_{xx,0} + b_{sj} \rho_{xx,0}^2) + \sigma_{xy,int}^{AH} \rho_{xx}^2 \quad (4.19)$$

where $\rho_{yx,ext}^{AH}$ and $\rho_{yx,int}^{AH}$ are the extrinsic and intrinsic components of ρ_{yx}^{AH} , respectively. For the extrinsic component in Eq. 4.19, $\rho_{xx,0}$ is the residual component of ρ_{xx} caused by crystal defects and a_{sk} and b_{sj} are the material-dependent scaling constants for the extrinsic skew-scattering and side-jump mechanisms, respectively. The intrinsic component in Eq. 4.19 is scaled with ρ_{xx}^2 by $\sigma_{xy,int}^{AH}$.

The external field H dependence of the Hall resistivity ρ_{yx} for TbMn₆Sn₆ is shown in Fig. 4.4(a) with $H \parallel c$ and $I \perp c$. As temperature is increased, the saturated ρ_{yx} is

exponentially increased. Below around 100 K, ρ_{yx} is nearly linear with H while between 100 and 220 K, ρ_{yx} exhibits a hysteresis curve. ρ_{yx} overlaid with magnetization M with $H \parallel c$ is shown for 2 and 100 K in Fig. 4.4(b). At 100 K, ρ_{yx} closely following the hysteresis in M with $H \parallel c$. However, this is not the case at 2 K, as no hysteresis is present in ρ_{yx} , thereby not following M with $H \parallel c$. Since the anomalous Hall resistivity ρ_{yx}^{AH} is conventionally defined proportional to M_z [Eq. 4.17], some additional mechanism is likely present which cancels out the intrinsic AHE, such as a possible leading negative extrinsic contribution.

To investigate the separate intrinsic and extrinsic contributions in TbMn_6Sn_6 , ρ_{yx}^{AH} is plotted against ρ_{xx}^2 in Fig. 4.3(a) where ρ_{yx}^{AH} is extracted from ρ_{yx} using Eq. 4.18. At temperatures above 100 K [Fig. 4.3(a)], ρ_{yx}^{AH} decreases smoothly with decreasing ρ_{xx}^2 , while at and below 100 K, ρ_{yx}^{AH} deviates from this smooth behavior and remains near a magnitude of $10^{-1} \Omega \text{ cm}$. Since extrinsic effects in materials are generally thermally saturated out at elevated temperatures, the transition at 100 K upon increasing temperature is likely a transition from a leading extrinsic to intrinsic contribution in the AHE. Using Eq. 4.19, $\sigma_{xy,int}^{AH}$ can be approximated within the high temperature regime as $\rho_{xx,0} \rightarrow 0$ [Fig. 4.3(b)], yielding $\sigma_{xy,int}^{AH} \approx 96.6 \Omega^{-1} \text{ cm}^{-1} = 0.06 e^2/h$ per kagome layer, which is $\sim 40\%$ of the value calculated by Yin et al. [1]. However, as can be seen in Fig. 4.3(b), the high temperature regime is not truly linear and thus $\sigma_{xy,int}^{AH}$ is temperature dependent. Since $\sigma_{xy,int}^{AH}$ arising from a field induced topological Chern gap (and hence Δ and E_F) is generally temperature independent in materials [see *Appendix A.4: Topological Chern Gap State*],

the leading intrinsic contribution may arise elsewhere within the electronic structure of TbMn_6Sn_6 and thus requires further investigation.

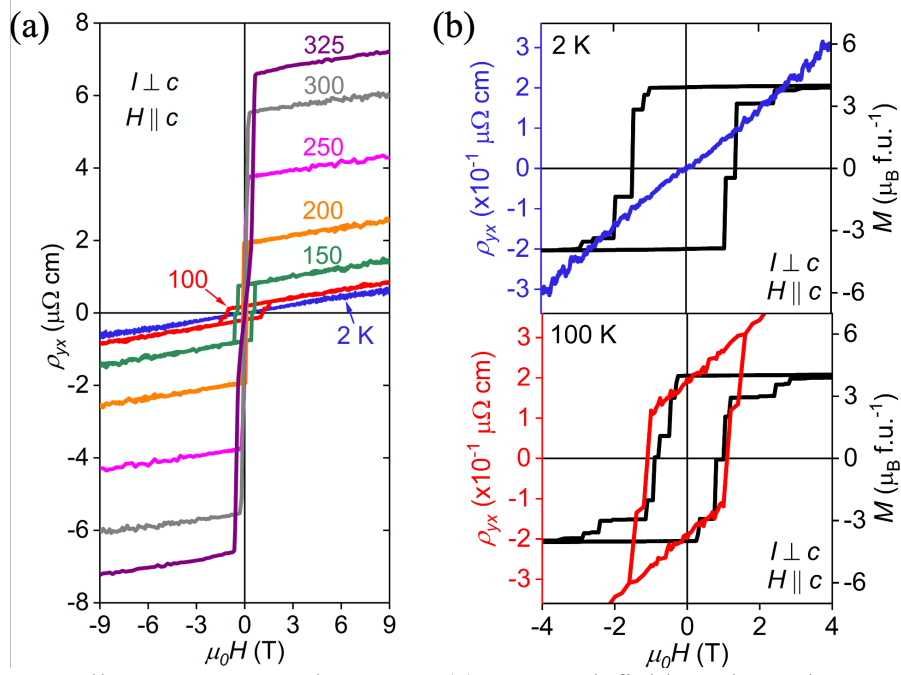


Figure D.2: *Hall resistivity in TbMn_6Sn_6 .* (a) External field H dependence of the Hall resistivity ρ_{yx} with $H \parallel c$ and $I \perp c$. (b) External field dependence of ρ_{yx} overlaid with magnetization M with $H \parallel c$ and $I \perp c$ between for 2 and 100 K.

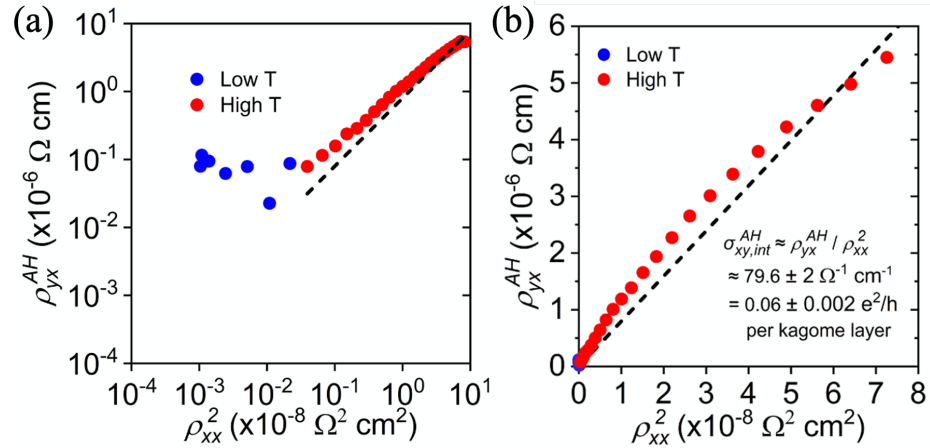


Figure D.3: *Anomalous Hall Analysis in TbMn₆Sn₆*. Square of longitudinal resistivity dependence of the anomalous Hall resistivity with $H \parallel c$ and $I \perp c$ for in (a) logarithm scale and (b) non-logarithm scale for low (< 100 K) and high (≥ 100 K) temperature regimes shown in blue and red, respectively. The dashed line in (b) shows a linear fit through zero intercept for the high temperature regime with a slope of $\approx 96.6 \Omega^{-1} \text{ cm}^{-1} = 0.06 e^2/h$ per kagome layer.

Chapter 5: Summary and Outlook

In this master's thesis project, we have explored the role of the rare-earth elements $R = Y, Tb$ on the magnetic and magnetotransport properties within the RMn_6Sn_6 compounds using magnetometry and magnetotransport combined with first-principles calculations. The framework of this study largely focused on the magnetic rare-earth compound $TbMn_6Sn_6$ and compared the magnetic and electronic properties to the non-magnetic rare-earth parent compound YMn_6Sn_6 . Using Sn-flux growth, single crystals of YMn_6Sn_6 and $TbMn_6Sn_6$ were successfully grown, exhibiting high metallicity and distinct features consistent with transformations to their magnetic structure revealed from electronic transport and magnetic susceptibility measurements. By considering a simplified description of the collinear configuration on magnetic anisotropy energy, by lumping the Heisenberg exchange and single-site anisotropy terms, we demonstrated that how the spin-reorientation magnetic phase diagram for $TbMn_6Sn_6$ is quantitatively described by the temperature dependencies of magnetic moments on the Mn- and Tb-sublattices. An enhanced magnetic state on Tb at low temperatures leads to a strong out-of-plane magnetization which likely enhances the stability of the intrinsic topological Chern gap state previously observed by Yin et. al. [1]. To explore to what extent this above-mentioned magnetic state of Tb affects the electronic properties in $TbMn_6Sn_6$, especially near the Fermi surface, magnetotransport measurements were performed on YMn_6Sn_6 and

TbMn₆Sn₆ with $I \perp c$ and $H \parallel c$. By comparing the measured MR to that of YMn₆Sn₆ the role of the magnetic rare-earth Tb on the electronic properties was clearly significant low temperatures. The negative to large and positive MR in TbMn₆Sn₆ below around 100 K was likely attributed to the enhanced magnetic state on Tb at low temperatures. The field dependence of ρ_{yx} and ρ_{xx}^2 dependence of ρ_{xy}^{AH} for TbMn₆Sn₆ provided evidence of a likely dominating extrinsic contribution below 100 K and intrinsic contribution above 100 K not governed by a field-induced topological Chern gap.

Following these key findings from this experimental study on YMn₆Sn₆ and TbMn₆Sn₆, we now discuss future work to expand this scope to understand role of the rare-earth elements on the magnetic and magnetotransport properties within the RMn₆Sn₆ compounds. Since the RMn₆Sn₆ compounds are naturally predicted to host Dirac cones, a comprehensive ARPES study on YMn₆Sn₆ and TbMn₆Sn₆ to identify the location of these energy-dependent Dirac cones, as previously done for Fe₃Sn₂ [8], may provide further insight into the intrinsic electronic transport properties of these materials. To determine the origin of the leading intrinsic contribution to the AHE in TbMn₆Sn₆, which may reside elsewhere to the K and K' points, density functional theory (DFT) calculations would provide insight into which bands in TbMn₆Sn₆ reside near the Fermi level and thus contribute most to a non-zero Berry curvature. Lastly, in the context of comparing the magnetic rare-earth TbMn₆Sn₆ compound with the non-magnetic rare-earth YMn₆Sn₆ compound, doping YMn₆Sn₆ with Tb at various concentrations would provide further detail into the role of the magnetic state of Tb. A previous neutron study by Bykov et. al. [29] on the temperature dependence of the Bragg peaks in Y_{1-x}Tb_xMn₆Sn₆ ($x = 0, 0.2,$

0.225, 0.25) revealed that the helimagnetic phases in YMn_6Sn_6 naturally mix with the ferrimagnetic (FiM) phases in TbMn_6Sn_6 . Therefore, the scope of this thesis project would be expanded by a similar experimental study on single crystals of $\text{Y}_{1-x}\text{Tb}_x\text{Mn}_6\text{Sn}_6$.

At a high-level scope, the long-term goal following this project would be to construct a comprehensive understanding of the role of the rare-earth elements among the nine available RMn_6Sn_6 compounds. Because of the various magnetic ground states which emerge naturally from the interaction between competing interplanar interactions, the other RMn_6Sn_6 compounds provide a unique opportunity to explore both emergent and topological properties arising from the interactions between complex magnetism and electronic topology. As demand for new frontiers within nanotechnology continues to increase over the next decade, engineering components for spin-based electronic devices with materials containing unique emergent and topological properties, such as in RMn_6Sn_6 compounds, may provide new avenues for innovation.

Appendix: Kagome Lattice Electronic Properties

A.1 Tight-Binding Model

Due to the unique geometry of the kagome lattices, these lattices naturally host interesting electronic states. A common approach to visualize the electronic band structure for a periodic crystal lattice containing atomic orbitals at its lattice sites is to use a tight-binding model, which assumes that tightly bound electrons on the lattice can be modeled by a simplified quantum mechanical model [30]. Let us consider a Fourier series of Bloch functions describing the electronic states for a given periodic lattice with Bravais lattice vector \vec{R}_n :

$$\psi_{\vec{k},m}(\vec{r}) = \sum_n e^{i\vec{k}\cdot\vec{R}_n} \varphi_m(\vec{r} - \vec{R}_n), \quad (\text{A.1})$$

where $\varphi_m^{(a)}(\vec{r} - \vec{R}_n)$ is the real space wavefunction localized at \vec{R}_n with \vec{r} being the electron position and m being the band index, \vec{k} is the wavevector of the Bloch's function, and the summation is over all n atomic sites [31]. By assuming the m th band contributes greatest to the Bloch states closest to Fermi level, the energy dispersion relation can therefore be approximated with Eq. A.1. under the first approximation as

$$E(\vec{k}) = \int \psi_{\vec{k},m}^*(\vec{r}) \mathcal{H}(\vec{r}) \psi_{\vec{k},m}(\vec{r}) d^3r, \quad (\text{A.2})$$

where $\mathcal{H}(\vec{r})$ is some arbitrary Hamiltonian with \vec{r} dependence.

A.2 Monolayer Kagome Lattice

For a single 2D lattice, let us assume that electrons only hop between nearest-neighbor (NN) sites, as governed by the Hamiltonian

$$\mathcal{H}_{hop,1}(\vec{r}) = -t_1 \sum_{\langle ij \rangle, \mu} (c_{i,\mu}^\dagger c_{j,\mu} + c_{j,\mu}^\dagger c_{i,\mu}), \quad (\text{A.3})$$

where t_1 is the NN in-plane orbital hopping strength, $\langle ij \rangle$ indexes NN pairs, μ is the spin polarization, and $c_i^\dagger (c_j)$ is the electron creation (annihilation) operator with $c_i (c_j^\dagger)$ being its Hermitian conjugate. Using $\mathcal{H}_{hop,1}$ [Eq. A.3] as the Hamiltonian in Eq. A.2., the energy dispersion relation for the 2D honeycomb lattice [Fig. A.1] and the 2D kagome lattice [Fig. A.1] is approximated in Fig. A.2(a) and (b), respectively. For both models, two bands emerge (valence on bottom and conduction on top) at the K and K' points in the first Brillouin zone, as shown in Fig. A.2(c), known as Dirac points (DP), forming a Dirac cone in (k_x, k_y, E) . Because we have a two-band model in the vicinity of the K and K' points, the Hamiltonian in momentum-space $\mathcal{H}(\vec{k})$ can be approximately described by a two-by-two Hermitian matrix in terms of the Pauli matrices $\vec{\sigma}_\alpha$ ($\alpha = x, y, z$), akin to spin- $1/2$ particles in a magnetic field, with z perpendicular to lattice plane:

$$\mathcal{H}(\vec{k}) = \vec{d}(\vec{k}) \cdot \sigma_\alpha = \vec{d}_x(\vec{k})\sigma_x + \vec{d}_y(\vec{k})\sigma_y + \vec{d}_z(\vec{k})\sigma_z, \quad (\text{A.4})$$

where $\vec{d}(\vec{k})$ defines a mapping of the k_x - k_y plane to a Bloch unit sphere with unit vector $\hat{d}(\vec{k}) = \vec{d}(\vec{k})/|\vec{d}(\vec{k})|$. By expanding around the K and K' points, $\mathcal{H}(\vec{k})$ for Dirac fermions has been shown to be described by the following Hamiltonian [32]:

$$\mathcal{H}(\vec{k}) = v_F(k_x \tau^z \sigma^x + k_y \sigma^y), \quad (\text{A.5})$$

where $v_F = \sqrt{3}a_0t_1/2$ is the Fermi velocity with a_0 being the distance between NN sites and $\tau^z = \pm$ is a pseudo spin-variable denoting whether described Hamiltonian is centered at the K or K' points defined at $(k_x, k_y) = (\pm 4\pi/3a_0, 0)$ [Fig. A.2(c)]. The eigenvalues for this expression [Eq. A.5] yield a linear approximation for the dispersion relation close to the DP:

$$E(k') \approx E_D \pm \hbar v_F k' = \pm \hbar v_F k', \quad (\text{A.6})$$

where the energy at the DP is given by $E_D = E = 0$ with $k' = K(K') + k$ being the wavevector approximated near the DP. The significance of the DP is that it denotes the point where the energy of the valence and conduction bands equal, causing electrical conduction at this point to be described by the movement of massless Dirac fermions [33]. Similarly, for the kagome lattice model [Fig. A.2(b)], the same two bands as in the honeycomb lattice with this DP also appear, due to the same point symmetry of the hexagons, but because of the additional equilateral triangles, a flat band (FB) also appears. The first Brillouin zone for the kagome lattice model is shown in Fig. A.2(c), illustrating the DPs at the hexagon corners. The mechanism behind the FB within the context of the NN tight-binding model is attributed to destructive quantum interference of the superimposed wavefunctions at the M-points in the hexagonal Brillouin zone ensuing from the unique geometry of the kagome lattice [34]. Consequently, electrons become localized within the hexagon of the kagome lattice with an infinite effective mass, leading to increased electronically correlated phenomenon. For example, when the FB is partially filled, fractional quantum Hall states can emerge as these localized electrons can mimic Landau levels, as in the case of twisted bilayer graphene [35].

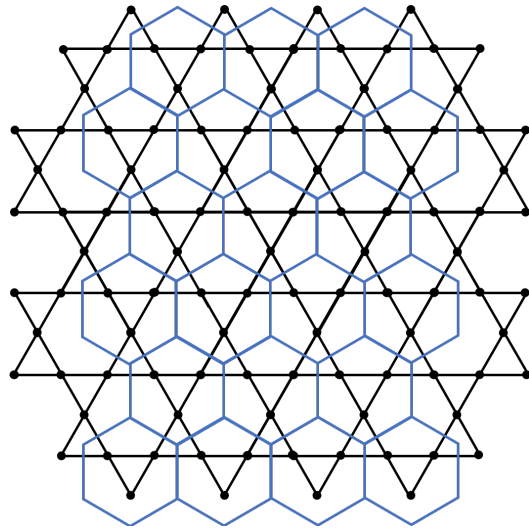


Figure A.1: Two-dimensional (2D) kagome lattice in black overlaid with the 2D honeycomb lattice in blue. The black dots denote the atomic sites of the kagome lattices.

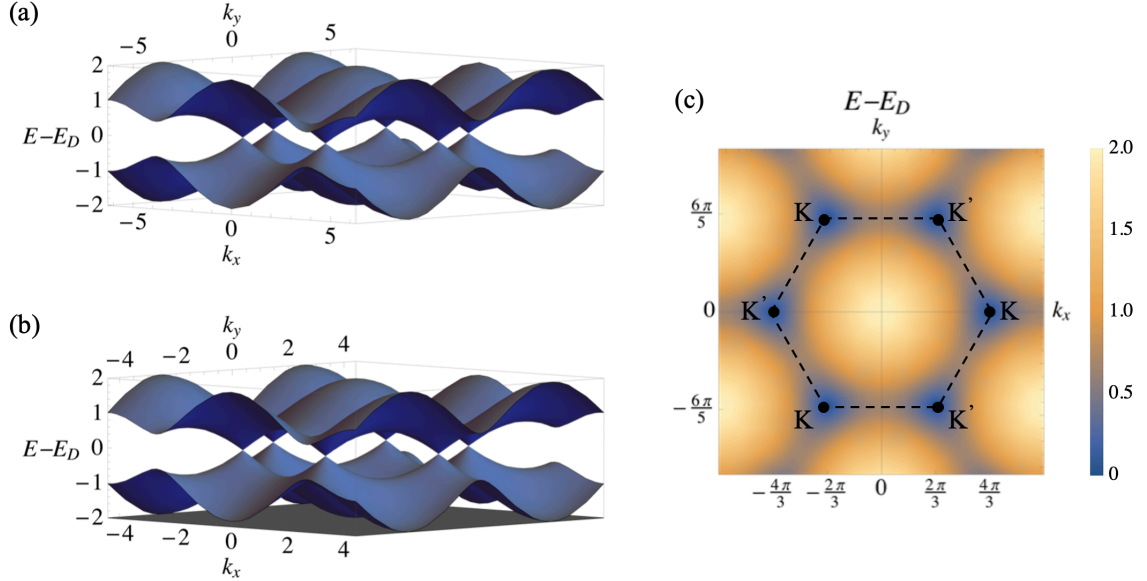


Figure A.2: *Simple tight-binding model with nearest-neighbor hopping for a single layer of the honeycomb and kagome lattices with $t_1 = 1$ (arbitrary units). (a) Honeycomb lattice calculated band structure. The points at which the top and bottom bands touch at $E_D = 0$ are the Dirac points (DP). (b) Kagome lattice calculated band structure (shifted to $E_D = 0$). The additional band at the bottom is the Flat band (FB). (c) Energy density plot for the top band in (b). The dashed line illustrates the hexagon shape of the first Brillouin zone, and the black dots denote the DPs which exist at the K and K' points.*

A.3 Bilayer Kagome Lattice

For the bilayer kagome lattice, illustrated by overlaying two cryptographically equivalent 2D kagome lattices along the c-axis in Fig. A.3, let us assume that electrons can hop between NN sites within the lattices as well as between vertically displaced sites as governed by the Hamiltonian

$$\mathcal{H}_{hop,2}(\vec{r}) = -t_1 \sum_{m,\langle ij \rangle, \mu} (c_{m,i,\mu}^\dagger c_{m,j,\mu} + c_{m,j,\mu}^\dagger c_{m,i,\mu}) - t_2 \sum_{m,i,\mu} (c_{1,i,\mu}^\dagger c_{2,i,\mu} + c_{2,i,\mu}^\dagger c_{1,i,\mu}), \quad (\text{A.7})$$

where t_1 and $\langle ij \rangle$ are the NN orbital hopping strength and index pairs within the planes of the layers, respectively, t_2 is the orbital hopping strength between vertically displaced sites

of the layers, and $m = 1, 2$ is the layer index. Using $\mathcal{H}_{hop,2}$ [Eq. A.5] as the Hamiltonian in Eq. A.2., the energy dispersion relation can be approximated for the bilayer kagome lattice in Fig. A.4(a). Compared to the single layer kagome lattice model [Fig. A.2(b)], the band structure is now doubled and split by $\pm t_2$ [Fig. A.4(a)] due to bonding-antibonding splitting of order t_2 between NN orbitals on the vertically displaced sites, similar to the case of AA-stacked bilayer graphene [36]. The Dirac cones of each band structure overlap into a Dirac circle (DC) separated by $\Delta E_D = E_{D,2} - E_{D,1} = 2t_2$ with its midpoint at E_{DC} [Fig. A.4(c)]. The lower band structure is the bonding structure centered at $E - E_{DC} = E_{D,1}$ [Fig. A.4(b)] and the upper band structure is the antibonding structure centered at $E - E_{DC} = E_{D,2}$ [Fig. A.4(d)]. The energy dispersions near $E_{D,1}$ and $E_{D,2}$ for each Dirac cone can be individually approximated using Eq. A.4 with $E_D = E_{D,1} = -t_2$ or $E_D = E_{D,2} = +t_2$.

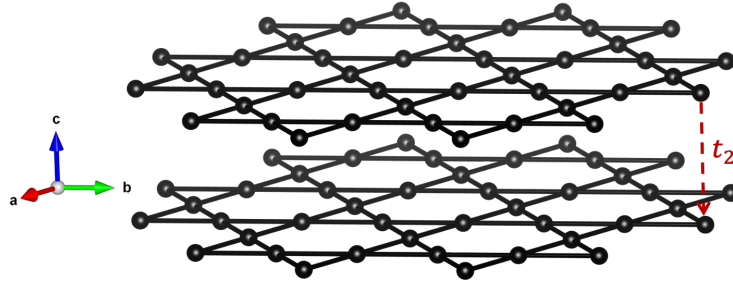


Figure A.3: 3D illustration of the bilayer kagome lattice where two 2D kagome lattices are stacked along the c -axis. The vertical dashed arrow shows hopping path between a vertically displaced site with orbital hopping strength t_2 .

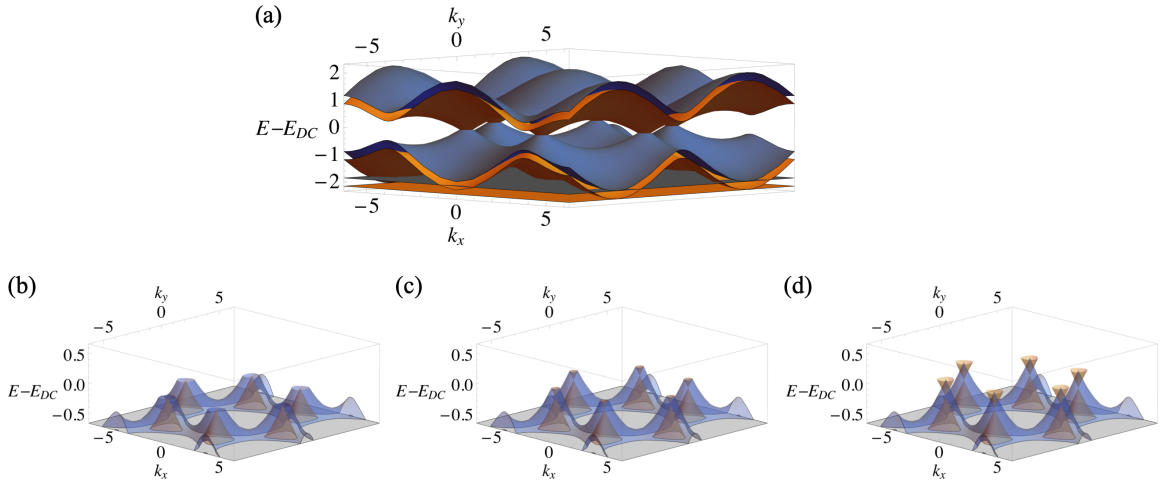


Figure A.4: *Simple tight-binding model with nearest-neighbor hopping (arbitrary units) for a bilayer kagome lattice with $t_1 = 1$ and $t_2 = 0.15$.* (a) Calculated band structure where orange and blue represent the lower and upper bands, respectively. (b) Energy filled up to the lower Dirac point at $E - E_{DC} = E_{D,1} = -t_2$. (c) Energy filled up to the midpoint between the lower and upper Dirac points at $E - E_{DC} = 0$ within the Dirac circle. (d) Energy filled up to the upper Dirac point at $E - E_{DC} = E_{D,1} = +t_2$.

A.4 Topological Chern Gap State

When spin-orbit interactions within a kagome lattice system become significant, a magnetized Dirac fermion with an out-of-plane component can induce a topological Chern gap at the K(K')-points [37]. To understand this effect, we revise our simple NN tight-binding Hamiltonian $\mathcal{H}_{hop,1}$ [Eq. A.3] [38] for the case of ferromagnetism along the z -direction, thereby breaking time-reversal symmetry:

$$\mathcal{H}_{hop,\uparrow}(\vec{r}) = -t_1 \sum_{\langle ij \rangle} c_{i,\uparrow}^\dagger c_{j,\uparrow}, \quad (\text{A.8})$$

where \uparrow denotes the spin polarization along z . We next introduce the effect of SOC by considering the Kane-Mele model with SOC-induced hopping between the next-nearest-

neighbors (NNN) [39], which effectively breaks SU(2) symmetry for the spin-polarized case. The Hamiltonian for the Kane-Mele SOC is given by

$$\mathcal{H}_{SOC}(\vec{r}) = i \sum_{\langle ij \rangle} \lambda v_{ij} (c_{i\uparrow}^\dagger c_{j\uparrow} - c_{i\downarrow}^\dagger c_{j\downarrow}), \quad (\text{A.9})$$

where λ is the Kane-Mele SOC strength and $\lambda v_{ij} = (\vec{E}_{ij} \times \vec{v}_{ij}) \cdot \vec{S}_z = \frac{2\lambda}{\sqrt{3}} (\hat{d}_i \times \hat{d}_j) \cdot \vec{S}_z$ with \vec{E}_{ij} being the electric field of the NNN hopping path, \vec{v}_{ij} being the NNN hopping path velocity vector, \vec{S}_z being the spin vector of the electron with z polarization, and $\hat{d}_i(\hat{d}_j)$ being the unit vector at site $i(j)$. For an electron with its spin perpendicular to the kagome plane ($\vec{S}_z \neq 0$), \mathcal{H}_{SOC} therefore generates a perturbation to the original electronic band structure [Fig. A.2(b)]. Conversely, when the lattice magnetic moment \vec{m} lies within the plane ($\vec{m} \cdot \hat{z} = 0$), $\mathcal{H}_{SOC} = 0$ (since $\vec{S}_z = 0$). A conceptual illustration on the Kane-Mele SOC model is shown in Fig A.5.

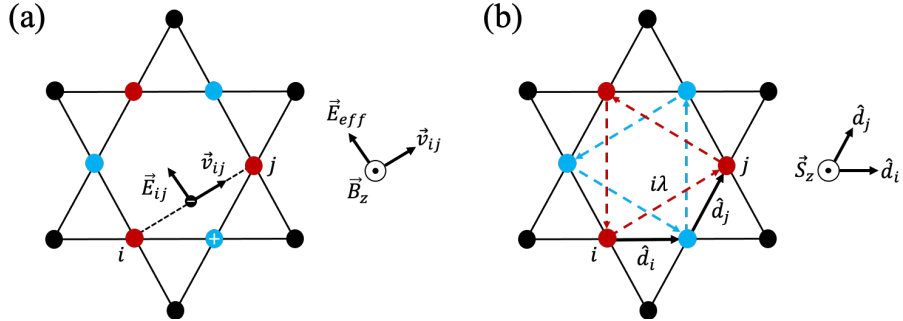


Figure A.5: *Conceptualization of the Kane-Mele spin-orbit coupling (SOC) model.* (a) In a classical picture, as an electron hops from site i to a next-nearest-neighbor (NNN) site j , it feels an effective electric field E_{ij} induced by the positive charge via coulombic potential on the nearest-neighbor (NN) site. This produces an effective magnetic field B_z in the rest frame of the electron which couples with the spin vector of the electron S_z via SOC. (b) The SOC interaction can also be written in terms of the hopping unit vectors d_i and d_j .

By using $\mathcal{H}_{hop,\uparrow} + \mathcal{H}_{SOC}$ [Eq. A.8 and A.9] as the Hamiltonian in Eq. A2., the energy dispersion relations for the monolayer and bilayer kagome lattices now effectibely opens energy gaps at the Dirac points as shown in Fig. A.6. Because of the spin-polarized Kane-Mele SOC effect [Eq. A.9], this pertubation is equivalent to the relativistic Dirac fermions aquiring a mass term. Eq. A.5 can now be rewritten [40]:

$$\mathcal{H}(\vec{k}) = v_F(k_x\tau^z\sigma^x + k_y\sigma^x) + m\sigma^z, \quad (\text{A.10})$$

The eigenvalues for this expression [Eq. A.10] yield a non-linear approximation for the dispersion relation close to the DP which has the form of a relativistic particle:

$$E(k') \approx E_D \pm \sqrt{(\hbar k' v_F)^2 + (m^* v_F^2)^2}, \quad (\text{A.11})$$

where $m^* = 2\lambda \cos \theta / \sqrt{3} a_0^2 t_1^2$ is the effective mass of the Dirac fermion with θ being the angle \vec{m} make with the z-axis. Let $\Delta = 2m^* v_F^2 = 4\sqrt{3}\lambda \cos \theta$ be the energy band gap associated with the aquired mass m^* from the Kane-Mele SOC effect approximated to behave like a classical particle. Hence, only when \vec{m} is out-of-plane ($\theta \neq \pi/2$) can the band gap be opened by the spin-polarized Kane Mele SOC effect. Eq. A.10 can alternatively be written:

$$\mathcal{H}(\vec{k}) = v_F(k_x\tau^z\sigma^x + k_y\sigma^x) + \Delta\sigma^z\tau^z, \quad (\text{A.12})$$

which yields eigenvalues of similar for to Eq. A.11:

$$E(k') \approx E_D \pm \sqrt{(\hbar k' v_F)^2 + (\Delta/2)^2}, \quad (\text{A.13})$$

For the case of the bilayer kagome lattice, Eq. A.11 and A.13 can be used to approximate near $E_D = E_{D,1} = -t_2$ or $E_D = E_{D,2} = +t'$ as shown in Fig. A.6(c) and (d).

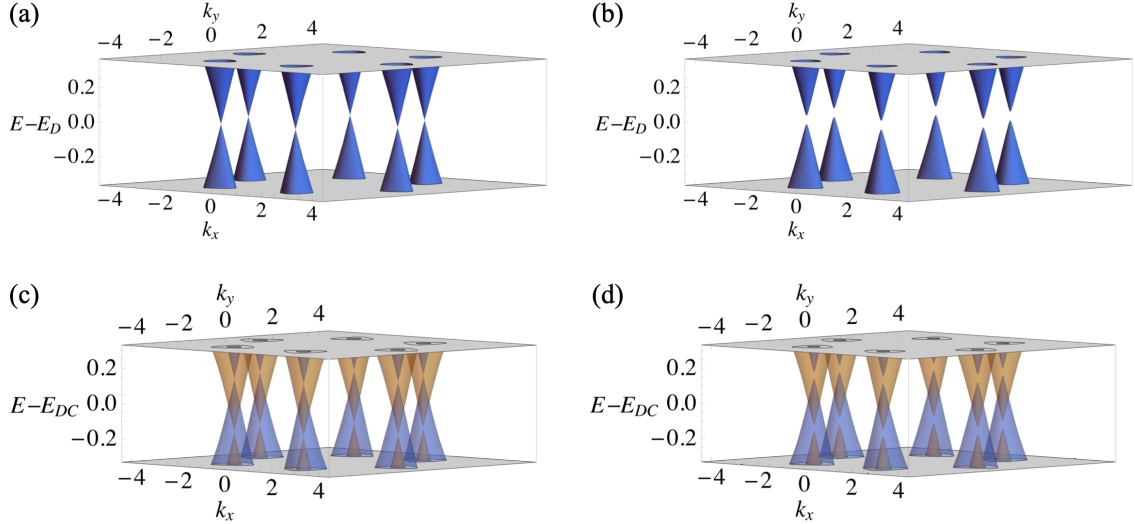


Figure A.6: *Band structure for a Dirac fermion acquiring mass for monolayer and bilayer kagome lattices with $t_1 = 1$ (arbitrary units). (a) Calculated band structure near the Dirac point energy $E_D = 0$ for a massless Dirac fermion ($m^* = 0$) in a single layer kagome lattice. (b) Calculated band structure near $E_D = 0$ for a Dirac fermion with an acquired mass ($m^* \neq 0$) in a single layer kagome lattice. (c) Calculated band structure near the Dirac point energies $E_{D,1} = -t_2$ and $E_{D,2} = +t_2$ for a massless Dirac fermion ($m^* = 0$) in a bilayer kagome lattice where $t_2 = 0.15$ and orange and blue represent the lower and upper bands, respectively. (d) Calculated band structure near $E_{D,1} = -t_2$ and $E_{D,2} = +t_2$ for a Dirac fermion with an acquired mass ($m^* \neq 0$) in a bilayer kagome lattice.*

The spin-polarized SOC-induced bandgap is also considered a Chern gap because it generates a topologically invariant when time-reversal symmetry is broken called the Chern number $C \in \mathbb{Z}$, which characterizes a distinctive state robust against small perturbations [41]. Recall that we defined a vector $\vec{d}(\vec{k})$ which maps the k_x - k_y momentum plane to a Bloch unit sphere with unit vector $\hat{d}(\vec{k}) = \vec{d}(\vec{k})/|\vec{d}(\vec{k})|$. Since we now consider a mass perturbation [Eq. A.10], we can use the following expression to describe the mapping [42]:

$$\vec{d}(\vec{k}) = (t_1 \sum_{\beta} \cos(\vec{k} \cdot \vec{a}_{\beta}) \hat{d}_x, t_1 \sum_{\beta} \sin(\vec{k} \cdot \vec{a}_{\beta}) \hat{d}_y, -2\lambda \cos\theta \sum_{\beta} \sin(\vec{k} \cdot \vec{b}_{\beta}) \hat{d}_z). \quad (\text{A.14})$$

where \vec{a}_β and \vec{b}_β are the NN and NNN hopping vectors on the kagome lattice ($\beta = 1, 2, 3$), respectively. The topological index for this representation via Chern number is calculated by the number of times $\hat{d}(\vec{k})$ wraps around the mapped Bloch unit sphere over the entire first Brillouin zone (BZ):

$$C = \frac{1}{4\pi} \int_{\text{BZ}} d\hat{k} \left(\frac{\partial \hat{d}}{\partial k_x} \times \frac{\partial \hat{d}}{\partial k_y} \right) \cdot \hat{d}. \quad (\text{A.15})$$

In the absence of the Chern gap ($\lambda = 0$ or $\theta = \pi/2$), the Chern number is calculated to be $C = 0$ for both the lower ($+\hat{d}$) and upper ($-\hat{d}$) Dirac bands. When the Chern gap is present ($\lambda \neq 0$ and $\theta \neq \pi/2$), however, the lower ($+\hat{d}$) and upper ($-\hat{d}$) Dirac bands yield $C = +1$ and -1 , which therefore describes topologically invariant phase.

A.5 Intrinsic Anomalous Hall Effects

Let us consider an electron wave packet centered at \vec{r}_c at a given time t . The ‘‘anomalous velocity’’ contribution to the Bloch electron group velocity \vec{v}_g can be expressed as [47]

$$\vec{v}_g = \frac{1}{\hbar} \frac{\partial E_n}{\partial \vec{k}} - \frac{d\vec{k}_c}{dt} \times \vec{\Omega}_{k_z}, \quad (\text{A.16})$$

where E_n is energy of the n th band of the unperturbed crystal, $\frac{d\vec{k}_c}{dt} = -e\vec{E}_y - e \frac{d\vec{r}_c}{dt} \times \mu_0 \vec{H}_z$ with \vec{k}_c being the wavevector of the wave packet at \vec{r}_c , and $\vec{\Omega}_{k_z}$ is momentum-space Berry curvature generated which is proportional to the area in the k_x - k_y momentum plane enclosed by the generated Berry phase, as conceptualized in Fig. A.7. The first term on the right in Eq. A.16 is the standard Bloch band group velocity calculated for the electronic

band structure. The second term on the right in Eq. A.16 is the “anomalous velocity”, given by $-\frac{d\vec{k}_{c,y}}{dt} \times \vec{\Omega}_{k_z}$, predicted to generate a non-zero anomalous Hall conductivity $\sigma_{xy,int}^{AH}$ in FM conductors [28]. In the context of the quantum Hall effect for a 2D electron gas, the integral of $\vec{\Omega}_{k_z}$ over the first Brilluion zone has been shown to be proportional to $\sigma_{xy,int}^{AH}$ and to be quantized based on the total magnetic-flux quanta per unit cell of the cyclotron orbits near a given Landau level [41]. This result was shown semi-classically [44] and can be generalized to other systems:

$$\sigma_{xy,int}^{AH} = -\frac{e^2}{h} \sum_n \int_{Filled} d\vec{k} \vec{\Omega}_{k_z}(n, \vec{k}). \quad (\text{A.17})$$

Since the behavior of a material is governed by the collective ensemble of electrons, the summation of the Berry curvature over all filled energy bands within the first Brilluion zone is only non-zero (and hence $\sigma_{xy,int}^{AH}$ is non-zero [Eq. A.17]) if certain symmetries of are broken. Fig. A.8, for example, illustrates how breaking both time-reversal and inversion symmetry can generate a non-zero total Berry curvature.

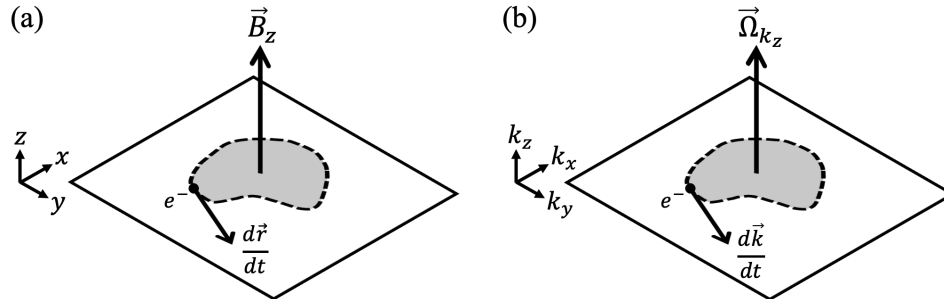


Figure A.7: *Berry curvature conceptualization.* (a) A magnetic field in the z -direction B_z is generated within the loop enclosed by the charge of the electron traveling in the x - y plane. (b) A Berry curvature in the k_z -direction Ω_{k_z} is generated within the loop enclosed by the electron traveling in the k_x - k_y plane with a non-zero Berry phase (adiabatic phase).

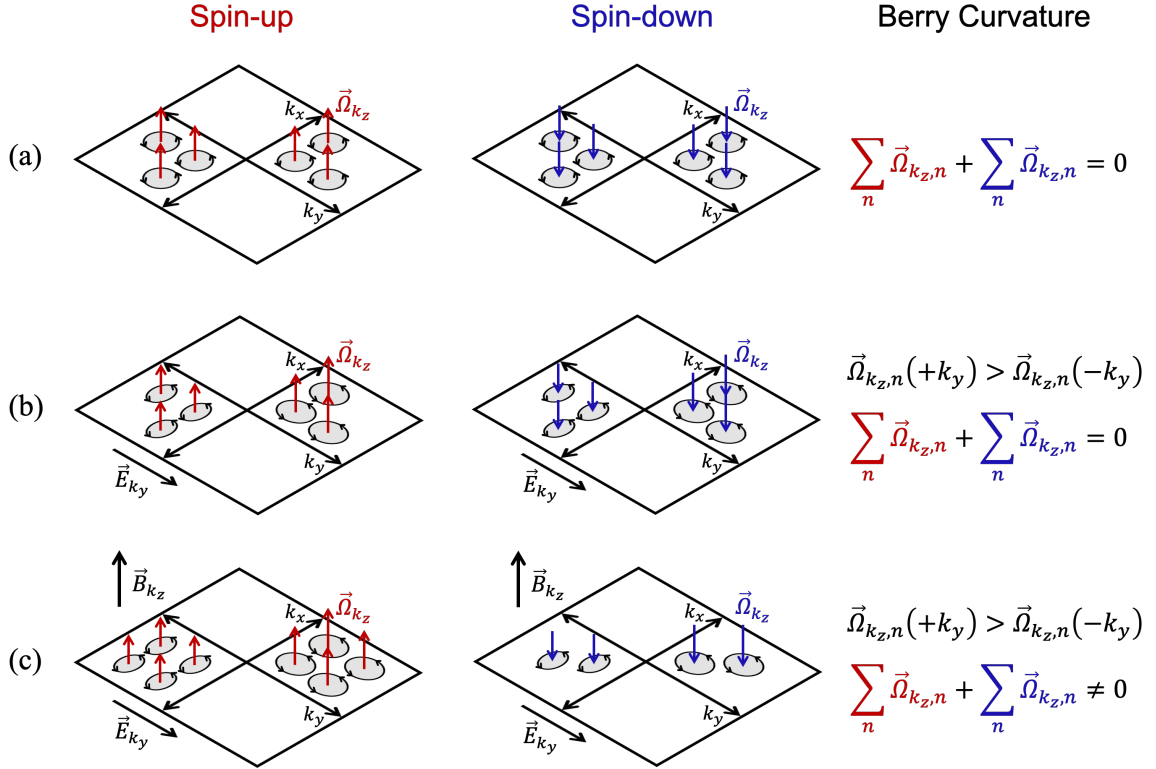


Figure A.8: *Non-zero Berry curvature conceptualization example.* (a) Because of the preserved inversion and time-reversal symmetries within the k_x - k_y plane for the spin-up (red) and spin-down (blue) electrons bands, the total summation of the Berry curvature Ω_{k_z} from each band n is zero. (b) When an applied electric field is induced in the k_y -direction E_{k_y} , inversion symmetry is broken within the k_x - k_y plane, generating greater values for $\Omega_{k_z}(+k_y)$ than for $\Omega_{k_z}(-k_y)$. The total summation of Ω_{k_z} is still however zero as time-reversal symmetry is still preserved. (c) When both E_{k_y} and a magnetic field in the k_z -direction B_{k_z} are applied, the inversion and time-reversal symmetries within the k_x - k_y plane for the spin-up and spin-down electrons bands are broken. The total summation of Ω_{k_z} is now non-zero, effectively yielding a non-zero intrinsic anomalous Hall conductivity.

For a system containing Dirac bands, such in a monolayer kagome lattice [Fig. A6(a)], breaking time-reversal symmetry with the inclusion of spin-orbit effects generates non-zero Berry curvature when the energy bands are only partially filled up within both massive Dirac bands [Fig. A.6(b)]. $\sigma_{xy, int}^{AH}$ for such a system can be regarded as a geometric

property connected to the filled energy states in a material connected to $\hat{d}(\vec{k})$ [Eq. A.14] [41]:

$$\sigma_{xy,int}^{AH} = \frac{e^2}{h} \int_{Filled} d\hat{k} \left(\frac{\partial \hat{d}}{\partial k_x} \times \frac{\partial \hat{d}}{\partial k_y} \right) \cdot \hat{d}, \quad (\text{A.18})$$

where $\vec{\Omega}_{k_z} = \left(\frac{\partial \hat{d}}{\partial k_x} \times \frac{\partial \hat{d}}{\partial k_y} \right) \cdot \hat{d}$. In simple terms, $\sigma_{xy,int}^{AH}$ for a single Dirac fermion can be conceptualized as proportional to the area enclosed by the filled states on the surface of the Bloch sphere of \hat{d} . The anomalous intrinsic anomalous Hall conductivity for a monolayer kagome lattice $\sigma_{xy,int,1}^{AH}$ can be therefore described, as illustrated in Fig. A.9, as

$$\sigma_{xy,int,1}^{AH} = \frac{|A_2 - A_1|}{2\pi} \frac{e^2}{h}, \quad (\text{A.19})$$

where A_1 and A_2 are the areas enclosed by the lower and upper hemispheres of the Bloch unit sphere, which states $\sigma_{xy,int,1}^{AH} \neq 0$ ($A_2 - A_1 \neq 0$) when in the presence of the Chern gap. When only the lower hemisphere of the Bloch sphere is completely filled ($A_1 = 2\pi$ and $A_2 = 0$), $\sigma_{xy,int,1}^{AH}$ takes on the integer $e^2/h = |0 - 2\pi|/2\pi \cdot e^2/h$. The level of the filled states of the unit Bloch sphere can also be conceptually regarded as the Fermi energy E_F or the energy level of the highest occupied state within a material at zero temperature. Alternatively, $\sigma_{xy,int,1}^{AH}$ can be connected to Δ and E_F [Fig. A.9(c)] by

$$\sigma_{xy,int,1}^{AH}(\Delta, E_F) = \frac{\Delta/2}{|E_F - E_D|} \frac{e^2}{h}, \quad (\text{A.20})$$

for $|E_F - E_D| \geq \Delta/2$. Similar, $\sigma_{xy,int,1}^{AH}$ thus takes on the integer e^2/h when $E_F - E_D$ is filled to the Chern gap ($|E_F - E_D| = \Delta/2$), i.e., only the lower Dirac band is filled ($C = +1$), also known as the integer quantum Hall state [45, 40]. By calculating the total

anomalous Hall conductivity σ_{xy}^{AH} by magnetotransport, one can therefore theoretically probe the intrinsic topological properties within a kagome quantum magnet.

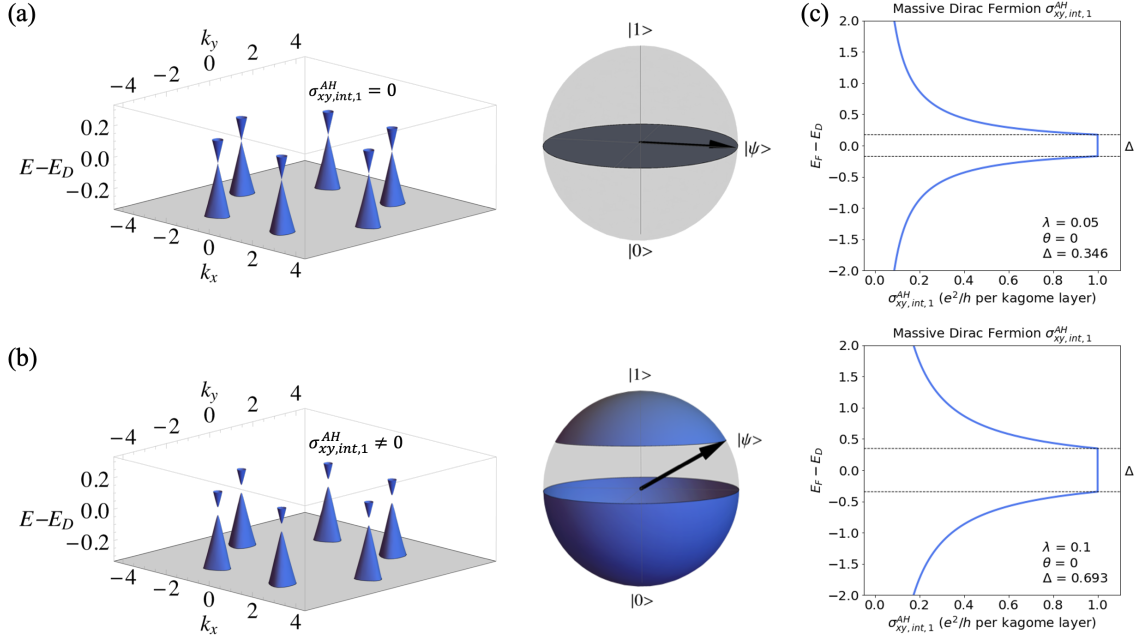


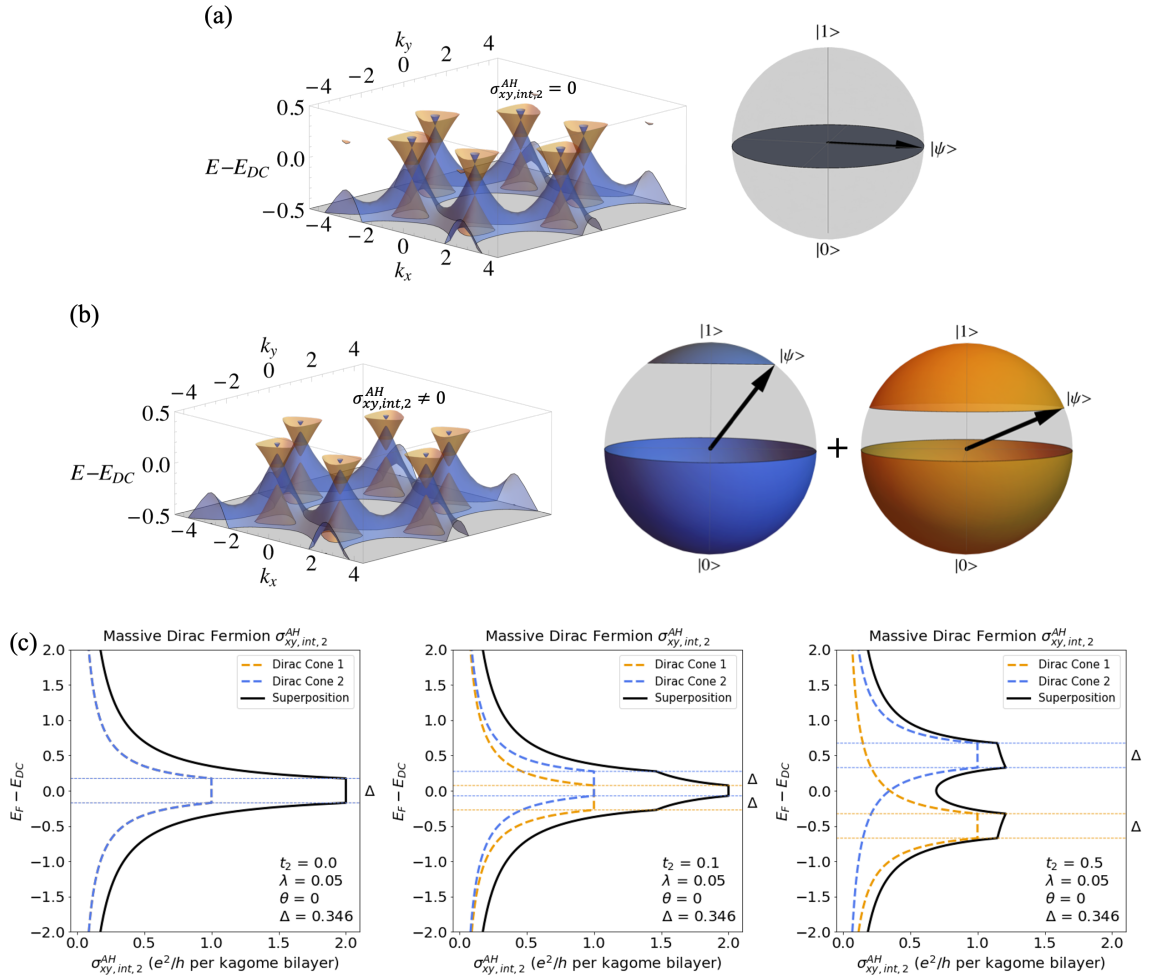
Figure A.9: *Conceptual formulation of the intrinsic anomalous Hall conductivity for a single Dirac fermion in a single layer kagome lattice using a Bloch sphere representation with $t_1 = 1$ (arbitrary units).* (a) Left: Filled states up to the Fermi energy $E_F = 0.15$ for a massless Dirac fermion. Right: Corresponding Bloch-sphere representation illustrating that the wavefunction of the massless Dirac fermion is confined to the Bloch sphere's equator, yielding a zero Berry phase. (b) Left: Filled states up to E_F for a massive Dirac fermion. Right: Corresponding Bloch-sphere representation illustrating that the wavefunction of the massive Dirac fermion is confined to the Bloch sphere's topologically distinctive lower and upper hemispheres, yielding a non-zero Berry phase. (c) Intrinsic anomalous Hall conductivity dependence on E_F for a massive Dirac fermion with Kane-Mele SOC strength $\lambda = 0.05$ and 0.10 with out-of-plane magnetization ($\theta = 0$), using Eq. A.20.

For a bilayer kagome lattice, the anomalous intrinsic anomalous Hall conductivity $\sigma_{xy, int, 2}^{AH}$ is conceptually more non-trivial. Because the massive Dirac fermions near the K

and K' points on the two layers within the bilayer lattice are related through inversion symmetry, both of the split Dirac cones [Fig. A.6(d)] contribute similarly to the Berry curvature $\vec{\mathcal{D}}$ [8], as shown in Fig. A.1(a) and (b). Therefore, $\sigma_{xy,int,2}^{AH}$ can be connected to Δ and E_F [Fig. A8(c)], assuming Δ is equal for both of the Dirac cones, by superimposing Eq. A.20 for both Dirac cones:

$$\sigma_{xy,int,2}^{AH}(\Delta, E_F) = \left(\frac{\Delta/2}{|E_F - E_{D,1}|} + \frac{\Delta/2}{|E_F - E_{D,2}|} \right) \frac{e^2}{h}, \quad (\text{A.21})$$

where E_F is referenced at the midpoint of the Dirac circle at E_{DC} .



Bibliography

- [1] J. X. Yin, W. Ma, T. A. Cochran, X. Xu, S. S. Zhang, H. J. Tien, N. Shumiya, G. Cheng, K. Jiang, B. Lian, Z. Song, G. Chang, I. Belopolski, D. Multer, M. Litskevich and Cheng, *Nature* **583**: 533-536 (2020).
- [2] I. Syozi, *Prog. Theor. Phys.* **6**, no. 3: 306-308 (1951).
- [3] V. Elser, *Phys. Rev. Lett.* **62**: 2405 (1989).
- [4] P. Anderson, *Mat. Res. Bull.* **8**: 153 (1973).
- [5] G. Overton, "Kagome - more than a woven basket," *LaserFocusWorld* (2015).
- [6] Z. Barkan, "Muslim Star of David at the Dome of the Rock," *Wikimedia Commons* (2013).
- [7] Z. Barkan, "Star of David," *Blogspot* (2009).
- [8] M. B. Hastings, *Phys. Rev. B* **63**, no. 1 (2001).
- [9] B. A. Volkov and O. A. Pankratov, *JETP Letters* **42**: 178 (1985).
- [10] I. I. Mazin, H. O. Jeschke, F. Lechermann, H. Lee, M. Fink, R. Thomale and R. Valenti, *Nat. Commun.* **5**: 4261 (2014).
- [11] Y. Cao, V. Fatemi, S. Fang, K. Watanabe, T. Taniguchi, E. Kaxiras and P. Jarillo-Herrero, *Nature* **556**: 43-50 (2018).
- [12] A. Grüneis, C. Attaccalite, A. Rubio, D. V. Vyalikh, S. L. Molodtsov, J. Fink, R. Follath, W. Eberhardt, B. Büchner and T. Pichler, *Phys. Rev. B* **80**: 075431 (2009).

- [13] D. Hsieh, D. Qian, L. Wray, Y. Xia, Y. S. Hor, R. J. Cava and M. Z. Hasan, *Nature* **452**: 970-974 (2008).
- [14] L. Ye, M. Kang, J. Liu, F. von cube, C. R. Wicker, T. Suzuki, C. Jozwiak, A. Bostwick, E. Rotenberg, D. C. Bell, L. Fu, R. Comi and G. J. Checkelsky, *Nature* **555**: 638-642 (2018).
- [15] M. Kang, L. Ye, S. Fang, J. S. You, A. Levitan, M. Han, J. I. Facio, C. Jozwiak, A. Bostwick, E. Rotenberg, M. K. Chan, R. D. McDonald, D. Graf, K. Kaznatcheev, E. Vescovo and Bell, *Nat. Mater.* **19**, no. 2: 163-169 (2020).
- [16] S. K. N. H. T. Nakatsuji, *Nature*, **534**: S5–S6 2016.
- [17] Q. Wang, Y. Xu, R. Lou, Z. Liu, M. Li, Y. Huang, D. Shen, H. Weng, S. Wang and H. Lei, *Nat. Commun.* **9**: 3681 (2018).
- [18] V. Hemmati, M. L. Plumer and J. P. Whitehead, *Phys. Rev. B* **86**: 104419 (2012).
- [19] N. J. Ghimire, R. L. Dally, L. Poudel, D. C. Jones, D. Michel, N. T. Magar, M. Bleuel, M. A. McGuire, J. S. Jiang, J. F. Mitchell, J. W. Lynn and I. I. Mazin, *Sci. Adv.* **6**, no. 51: eabe2680 (2020).
- [20] G. Venturini, D. Fruchart and B. Malaman, *J. Alloys Compd.* **236**: 102-110 (1996).
- [21] B. Malaman, G. Venturini, R. Welter, J. P. Sanchez, P. Vulliet and E. Ressouche, *J. Magn. Magn. Mater.* **202**, no. 2: 519-534 (1999).
- [22] D. M. Clatterbuck and K. A. Gschneidner, *J. Magn. Magn. Mater.* **207**: 78-94 (1999).
- [23] Y. Tian, L. Ye and X. Jin, *Phys. Rev. Lett.* **103**: 087206 (2009).
- [24] P. Villars, *Pearson's Handbook: Crystallographic Data for Intermetallic Phases.*, Materials Park (1997).
- [25] L. Zhang, *Unusual Magnetic Behavior of Some Rare-Earth and Manganese Compounds*, Van der Waals-Zeeman Institute (2005).
- [26] B. E. Douglas, *J. Chem. Educ.* **31**, no. 11: 598 (1954).
- [27] N. D. Mermin and H. Wagner, *Phys. Rev. Lett.* **17**: 1307 (1966).

- [28] N. J. Ghimire and I. I. Mazin, *Nat. Mater.* **19**: 137-138 (2020).
- [29] B. C. El Idrissi, G. Venturini, B. Malaman and D. Fruchart, *J. Less. Common Met.* **175**, no. 1: 143-154 (1991).
- [30] P. Terentev and N. Mushnikov, *Phys. Met. Metallogr.* **100**: no. 6: 50-56 (2005).
- [31] M. G. Kanatzidis, R. Pöttgen and W. Jeitschko, *Angew. Chem.* **44**: 6996-7023 (2005).
- [32] L. B. McCusker, R. B. V. Dreele, D. E. Cox, D. Louër and P. Scardi, *J. Appl. Cryst.*, **32**: 36–50 (1999).
- [33] J. Rodriguez-Carvajal, *Physica B*, **192**: 55–69 (1993).
- [34] Z. Guguchia, C. Mielke, W. Ma, V. Pomjakushin, O. Zaharko, X. Liu, J. X. Yin, S. S. Tsirkin, T. A. Cochran, M. Medarde, V. Poree, D. Das, C. N. Wang, J. Chang, T. Neupert, A. Amato, S. Jia, M. Z. Hasan and H. Luetkens, *arXiv: 2101.05763* (2021).
- [35] R. L. Dally, J. W. Lynn, N. J. Ghimire, D. Michel, P. Siegfried and I. I. Mazin, *Phys. Rev. B*, **103**: 094413 (2021).
- [36] N. A. Spaldin, *Magnetic Materials 2nd Edition*, Cambridge University Press (2011).
- [37] A. B. Pippard, *Magnetoresistance in Metals*, Cambridge University Press (1989).
- [38] E. H. Hall, *Am. J. Math.*, **2**: 287-292 (1881).
- [39] N. Nagaosa, J. Sinova, S. Onoda, A. H. MacDonald and N. P. Ong, *Rev. Mod. Phys.* **82**, no. 2: 1539-1592 (2010).
- [40] E. M. Pugh and T. W. Lippert, *Phys. Rev.* **42**: 709 (1932).
- [41] R. Karplus and J. M. Luttinger, *Phys Rev.* **95**, no. 5: 1154-1160 (1954).
- [42] A. Bykov, Y. Chetverikov, E. Moskvin, A. Pirogov and S. Grigoriev, *J. Magn. Magn. Mater.* **424**, no. 15: 47-351 (2017).
- [43] W. A. Harrison, *Electronic Structure and the Properties of Solids*, Dover Publications (1989).

- [44] C. Kittel, *Introduction to Solid State Physics 8th Edition*, Wiley (2004).
- [45] D. S. L. Abergel, V. Apalkov, J. Berashevich, K. Ziegler and T. Chakraborty, *Adv. Phys.* **59**, no. 4: 261-482 (2010).
- [46] K. S. Novoselov, A. K. Geim, S. V. Morozov, D. Jiang, M. I. Katsnelson, I. V. Grigorieva, S. V. Dubonos and A. A. Firsov, *Nature* **438**: 197–200 (2005).
- [47] Z. Li, J. Zhuang, W. Li, H. Feng, Q. Gao, X. Xu, W. Hao, X. Wang, C. Zhang, K. Wu, S. X. Dou, C. Lan, Z. Hu and Y. Du, *Sci. Adv.* **4**, no. 11: eaau4511 (2018).
- [48] K. S. Kim, A. L. Walter, L. Moreschini, T. Seyller, K. Horn, E. Rotenberg and A. Bostwick, *Nat. Mater.* **12**: 887-892 (2013).
- [49] H. M. Guo and M. Franz, *Phys. Rev B* **80**, no. 11: 3102 (2009).
- [50] Z.-Z. Lin and X. Chen, *Phys. Status Solidi RRL* **14**, no. 5: 1900705 (2020).
- [51] C. L. Kane and E. J. Mele, *Phys. Rev. Lett.* **95**: 226801 (2005).
- [52] F. D. Haldane, *Phys. Rev. Lett* **61**, no. 18 (1988).
- [53] D. J. Thouless, M. Kohmoto, M. P. Nightingale and M. d. Nijs, *Phys. Rev. Lett.* **49**, no. 6: 405-408 (1982).
- [54] T. Thonhauser and D. Vanderbilt, *Phys. Rev. B* **74**: 235111 (2006).
- [55] G. Sundaram and Q. Niu, *Phys. Rev. B* **59**, no. 23: 915-925 (1998).
- [56] M.-C. Chang and Q. Niu, *Phys. Rev. B*, **53**, no. 11: 7010 (1995).
- [57] G. Xu, B. Lian and S. C. Zhang, *Phys. Rev. Lett.* **115**, no. 18, 2015.
- [58] D. Betts, *Proc. N.S. Inst. Sci.* **40**, no. 2: 95-100 (1995).
- [59] S. Sachdev *ArXiv*: 1203.4565v4 (2012).
- [60] M. P. Shores, E. A. Nytko, B. M. Bartlett and D. G. Nocera, *J. Am. Chem. Soc.* **127**, no. 39: 13462-13463 (2005).

- [61] M. R. Norman, *arXiv*: 604.03048v4 (2016).
- [62] P. Mendels, F. Bert, M. A. de Vries, A. Olariu, A. Harrison, F. Duc, J. C. Trombe, J. S. Lord, A. Amato and C. Baines, *Phys. Rev. Letts.* **98**: 077204 (2007).
- [63] I. I. Mazin and N. J. Ghimire, *Nat. Mater.* **19**: 137-138 (2020).
- [64] J.-X. Yin, S. S. Zhang, H. Li, K. Jiang, G. Chang, B. Zhang, B. Lian, C. Xiang, I. Belopolski, H. Zheng, T. A. Cochran, S.-Y. Xu, G. Bian, K. Liu, T.-R. Chang, H. Lin, Z.-Y. Lu and Z. Wang, *Nature* **562**: 91-95 (2018).
- [65] Q. Wang, S. Shanshan, X. Zhang, F. Peng and H. Lei, *Phys. Rev. B* **94**: 075135 (2016).
- [66] I. I. Rabi, *Z. Phys.* **49**: 507–511 (1928).
- [67] L.-J. Yin, K.-K. Bai, W.-X. Wang, S.-Y. Li, Y. Zhang and L. He, *Front. Phys.* **12**: 127208 (2017).
- [68] L. L. Hinchey and D. L. Mills, *Phys. Rev. B* **33**, no. 5: 3329-3343 (1986)
- [69] A. H. C. Neto, F. G. N. M. R. Peres, K. S. Novoselov and A. K. Geim, *Rev. Mod. Phys.* **81**: 109-162 (2009).

Biography

David Connor Jones graduated from Potomac Falls High School, Loudoun, Virginia, in 2013. He received his Bachelor of Science in Chemical Engineering from Virginia Tech in 2018 and was employed as an associate at Technomics until 2019. Currently, he is working on completing his Master of Science in Applied and Engineering Physics at George Mason University.

List of Publications:

N. J. Ghimire, R. L. Dally, L. Poudel, D. C. Jones, D. Michel, N. T. Magar, M. Bleuel, M. A. McGuire, J. S. Jiang, J. F. Mitchell, J. W. Lynn and I. I. Mazin, *Sci. Adv.* **6**, no. 51: eabe2680 (2020).